

UNI  
BASEL

---

**Computational exploration of water structure and  
dynamics at heterogeneous interfaces**

---

INAUGRALDISSERTATION

zur

Erlangung der Würde eines Doktors Philosophie

vorgelegt der

Philosophisch-Naturwissenschaftlichen Fakultät

der Universität Basel

von

**Prashant Kumar Gupta**

aus Indien

Basel, 2014

Genehmigt von der  
Philosophisch-Naturwissenschaftlichen Fakultät auf  
Antrag von:

**Prof. Dr. Markus Meuwly**

**Prof. Dr. Gerhard Hummer**

Basel, 20 May 2014

Prof. Dr. Jörg Schibler  
Dekan

*To my parents*

विद्या ददाति विनयं विनयाद्याति पात्रताम् ।  
पात्रत्वाद्धनमाप्नोति धनाद्धर्मं ततः सुखम् ॥



# ACKNOWLEDGMENTS

---

I am deeply indebted to everyone in my life who has helped me to shape me as a person and researcher what I am today. It is my immense pleasure to be able to thank all of them here.

First and foremost, I would like to thank my family for their love and support in every aspect of my life. Starting from my early days in Gorakhpur, Uttar Pradesh (India), they inculcate me in a deep love for reading, a passion for learning and a skeptic attitude towards science. I am truly grateful to them for being patient with me and their unconditional love. I am thankful to my younger brother Amar for showing faith in me, when I make decisions on behalf of him. Finally, the person who is my role model in my life and who taught me many important things in life, my grandfather Gaya Prasad Gupta. I wish he could still be here with me.

In pursuing my scientific career, I am deeply indebted to my thesis advisor Markus Meuwly. He has been a continuous support for my research all these years, as well as his patience, motivation, enthusiasm, and immense knowledge, are essential for the completion of this work. Over the past four years I have learned a great deal from him about how to do science and communicate effectively, and how to become an independently good researcher. His motivation towards science was always a constant inspiration for me. Apart from professional relations, Markus has always been a generous source for advice and friendship and it has been a great pleasure to know him during these four years.

I would not have made it this far without the help and guidance of many other people throughout my education. I would like to thank K. Srihari (IITK) for being an excellent teacher and introducing me to the concept of chemical binding and statistical mechanics, and S. Manogaran (IITK) for Molecular spectroscopy. My first encounter with simulations was done with Markus Meuwly by his classes on theory of molecular simulations for liquids and

condense phase, basic electronic structure theory by Stephan Goedecker and reaction dynamics by Stephan Willstich at the University of Basel.

During my doctoral research, I had the pleasure of collaborating with emeritus Prof. Martin Karplus working on the problem related to quaternary structural transition in human hemoglobin.

My sincere thanks also go to all the group members here in the Meuwly group (Dr. Ana Patricia Gamiz-Hernandez, Dr. Christian Kramer, Dr. Lixian Zhang, Dr. Franziska Hofmann, Florent Hedin, Dr. Ganna Berezovska, Dr. Juvenal Yosa Reyes, Dr. Juan Carlos Castro Palacio, Dr. Jing Huang, Dr. Maurus Schmid, Dr. Myung Won Lee, Dr. Stephan Lutz, Dr. Pierre-Andre Cazade, Dr. Tibor Nagy, Maksym Soloviov, Akshaya Kumar Das, and Zhen-Hao Xu) during my stay in Basel over the past four years. I would like to give special thanks to Dr. Stephan Lutz and Dr. Myung Won Lee for their patience and support during the initial days of my doctoral studies, Dr. Tristan Bereau for helping and collaborating in one of my project and having wonderful discussions. It was always a different and wonderful experience with the group excursions we made in switzerland and the summer grill party on the terrace of our office. At last, I would like to thanks official memeber in the department, Maya Greuter and Danni Tischhauser for all their help and support.

Many thanks to Amit Sundriyal, Chanchal S. Chowdhary, Swarna Machineni, Mitasha Bharadwaj, Devender and Reena Negi, and Harish Phuleria, for being such a wonderful friends, and without them I couldn't imagine my four years in Basel. A very special thanks to Navratna Vajpai for being my very close friend and mentor in my scientific life.

Finally, my heartiest thanks to my wife Sarahna Mishra. All this would not have been possible without her constant encouragement and unconditional love. Sarahna has been my closest friend, advisor and support for me in every aspect of my life. Her excitement for life keeps me active and engaged. The past four years are one of the best moment of my life, because of her and my research work.

Funding from the Swiss National Science Foundation (SNSF), University of Basel, is gratefully acknowledged.

# Abstract

---

The goal of this thesis is to completely understand the dynamical behavior of water at different heterogeneous interfaces through statistical mechanics and computational methods. The molecular processes described here has been focused for past few decades, since the advent of experimental techniques to probe interfacial water molecules. A central theme throughout the thesis is to have quantitative understanding of water dynamics and structural interactions at the microscopic level. This work has immense importance in the field of analytical chemistry, surface science and biophysics.

We first describe the model for the intercalation process of a probe molecule in the chromatographic system. This study is relevant for industrial HPLC techniques, however complete microscopic level understanding of this process is still not completely understood. The effect of various solvent concentrations and phase thickness on the process of intercalation of acridine orange (probe) has been studied. An extension to this work is the thermodynamic model for intercalation of organic compounds based on experimentally known partition coefficient data.

Another interesting process is related with the vibrational spectroscopic feature of water at hydroxylated silica surface. A lot of experimental studies has been done to probe vibrational feature of water at solid interface and relate it to H-bonding structure at these interfaces. Most of these results focused on the vibrational feature in the stretching frequency regime of water but we focused on the vibrational bending mode of water close to the bare hydroxylated silica surface. This study demonstrate the importance of higher order multipoles to capture the precise spectroscopic description. Both the above studies are discuss in great detail in chapter IV.

Other interesting system we studied is the allosteric proteins, which mainly includes “*Dimeric Scapharca Hemoglobin*” and “*Tetrameric human hemoglobin*”. This study mainly focus on the role of water molecules close to protein surface and disentangle the coupled dynamics of ligand and water molecules at the interface. Finally, we will describe the quaternary structural transition (T→R) in “*tetrameric human hemoglobin*”. This work is described in chapter V of this thesis.

---





# CONTENTS

---

<b>1</b>	<b>Introduction</b>	<b>1</b>
1.1	The water molecule . . . . .	2
<b>2</b>	<b>Historical note on the role of water at different interfaces</b>	<b>7</b>
2.1	Water at different interfaces . . . . .	10
2.1.1	Water at solid silica interfaces . . . . .	11
2.1.2	Water at different biological interfaces . . . . .	12
<b>3</b>	<b>Theoretical and computational methods</b>	<b>17</b>
3.1	Molecular dynamics simulation . . . . .	19
3.1.1	Historical note . . . . .	19
3.1.2	Basic Theory . . . . .	19
3.2	Force Field . . . . .	22
3.2.1	Point charge force field . . . . .	22
3.2.2	Multipolar force field (MTP) . . . . .	24
3.3	Analysis Methods . . . . .	26
3.3.1	Umbrella Sampling . . . . .	27
3.3.2	Thermodynamic Integration . . . . .	30
<b>4</b>	<b>Water at hydroxylated silica interface</b>	<b>33</b>
4.1	Water at chromatographic interfaces . . . . .	35
4.1.1	Theoretical and computational methods . . . . .	36
4.1.2	Molecular Dynamics simulations . . . . .	39
4.1.3	Analysis of the Trajectories . . . . .	40
4.2	Results . . . . .	40
4.2.1	Solvent mixture without alkyl chains . . . . .	40
4.2.2	Characterization of the Solvent Mixtures . . . . .	41
4.2.3	Exchange Dynamics . . . . .	47
4.2.4	Dynamics of Acridine orange . . . . .	49
4.3	Thermodynamics of retention process in RPLC . . . . .	51
4.3.1	Computational methods . . . . .	52
4.3.2	Results . . . . .	52
4.4	Water at bare hydroxylated silica surface . . . . .	57
4.5	Computational part . . . . .	59
4.5.1	Description of the system . . . . .	59
4.5.2	Molecular dynamics simulations . . . . .	61
4.5.3	Exchange dynamics . . . . .	62

---

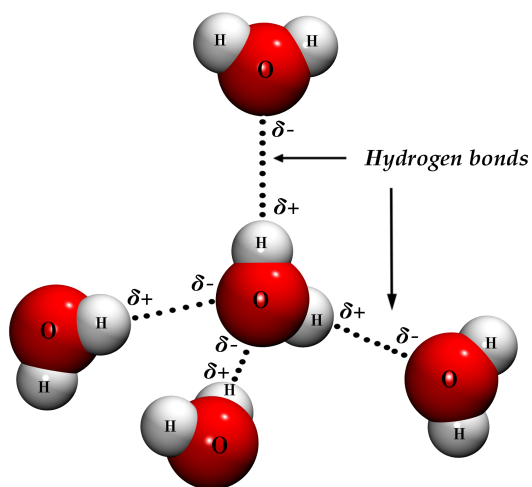
4.5.4	Infrared Spectra . . . . .	62
4.6	Results and discussion . . . . .	63
4.6.1	Static properties . . . . .	63
4.6.2	Orientational behavior of water . . . . .	64
4.6.3	Planar density distribution . . . . .	66
4.6.4	Dynamical properties . . . . .	66
4.6.5	Vibrational spectroscopy . . . . .	71
<b>5</b>	<b>Water dynamics at protein interface</b>	<b>77</b>
5.1	Introduction . . . . .	79
5.1.1	Differences in the structures of oxy and deoxy state . . . . .	80
5.2	Theoretical methods . . . . .	82
5.3	Results . . . . .	85
5.3.1	Role of Leu36 and Trp135 residue in CO migration . . . . .	85
5.3.2	Presence of water in distal pocket . . . . .	93
5.3.3	Structural changes at the dimeric interface . . . . .	93
5.3.4	Free energy simulations . . . . .	103
5.4	Conclusion . . . . .	104
5.5	Quaternary structural transition in HbA . . . . .	107
5.6	Computational methods . . . . .	107
5.7	Results . . . . .	108
5.8	Addition of chloride ions at $\beta_1\beta_2$ interface . . . . .	121
5.8.1	Reducing the force constant (k) between Fe and N . . . . .	125
5.9	2DN2 state in the presence of 2,3-DPG . . . . .	127
5.10	Outlook . . . . .	129
	<b>Bibliography</b>	<b>131</b>

# 1

## INTRODUCTION

---

*The first chapter briefly introduce the properties of water molecules*



Water is the chemical substance with chemical formula  $\text{H}_2\text{O}$ . Single oxygen atom reduces two hydrogen atoms to form covalently bonded water molecule. Water appears in nature in all three different states of matter namely solid (ice), liquid and gas (vapor). On Earth, 96.5 % of the planet's water is found in seas and oceans, 1.7% in groundwater, 1.7% in glaciers and the ice caps of Antarctica and Greenland, a small fraction in other large water bodies, and 0.001% in the air as vapor, clouds (formed of solid and liquid water particles suspended in air), and precipitation.

## 1.1 The water molecule

---

Water is one of the simplest and most studied compound either experimentally or theoretically. A water molecule is formed by making covalent bonds between two hydrogen atoms and a single oxygen atom. The structure of water is precisely determined from spectroscopic measurement.<sup>1,2</sup> Water molecules ( $\text{H}_2\text{O}$ ) are symmetric (point group  $C_{2v}$ ) with two mirror planes of symmetry and a 2-fold rotation axis. Figure 1.1 shows the results of these studies. Water adopts a bent structure with an HOH angle,  $\theta_{\text{HOH}} = 104.5^\circ$  and OH bond lengths,  $r_{\text{OH}} = 1\text{\AA}$ , on average. This geometry can be rationalized from molecular orbital theory which predicts that molecule is  $\text{sp}^3$  hybridized, with the two hydrogens and the four paired electrons pointing at the opposite edges of a tetrahedron resulting in  $C_{2v}$  point group symmetry. The large disparity in electronegativities between oxygen and hydrogen results in the majority of the electron density for this closed-shell, neutral molecule to be localized on the oxygen atom. This localization leads to the molecule being roughly spherical, as shown in Fig 1.1 b, with a van der Waals radius<sup>3</sup> determined from the crystal structure of ice of  $2.8\text{\AA}$ , which is identical to isoelectronic particles, methane and neon. The different electronegativities of oxygen and hydrogen coupled with the molecular symmetry, endows water with a large dipole moment. In a dilute vapor the molecular dipole can be measured with microwave spectroscopy and for water this yields a value of 1.85 D. In liquid and in ice Ih, water is further polarized by its surroundings leading to static dipole moments of 2.95 D and 3.0 D.

Apart from mostly studied compound, water is also known for its range of anomalous property. Some of these anomalous properties can be understood in the microscopic description of water termed as *hydrogen bonding*. Formation of

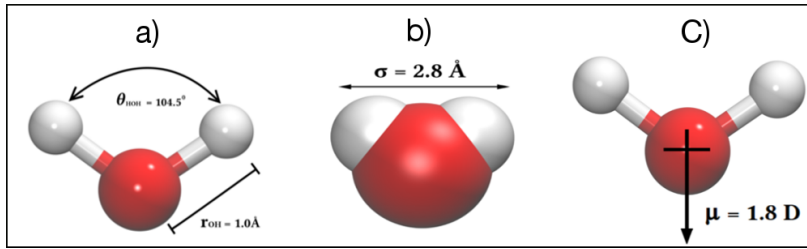


Figure 1.1

hydrogen-bonds introduces orientational dependence into molecular interactions. So water has some of the properties of normal liquid and some of the properties of fluctuating tetrahedral network of water. Hydrogen bonds are formed when a hydrogen *donor* atom is near a oxygen *acceptor* atom in the appropriate orientation. Increasing the temperature of water causes the solid phase (ice) to melt to a liquid phase and then causes a liquid phase to become a gas. Water is unusual in many more subtle ways. A statistical mechanical description of water by Dahl and Anderson<sup>4</sup> shows that water is able to store energy in hydrogen bonds and that can be weakened or broken. Water has a high dielectric constant, in part because of hydrogen bonds which are polarizable. So water is a better solvent compared to many other liquids. Water molecules in liquid water are attracted to each other by electrostatic forces, and these forces have been described as van der Waals forces or van der Waals bonds. Even though the water molecule as a whole is electrically neutral, the distribution of charge in the molecule is not symmetrical and leads to a dipole moment - a microscopic separation of the positive and negative charge centers. This leads to a net attraction between such polar molecules which finds expression in the cohesion of water molecules and contributes to viscosity, surface tension and in its high melting and boiling temperature. The high enthalpy of vaporization ( $40.5 \text{ kJ mol}^{-1}$ ) and a high surface tension of water ( $72 \text{ dyn cm}^{-1}$ ) are due to its property of forming hydrogen bonds. Liquid water has a relatively large heat capacity ( $75.2 \text{ J mol}^{-1} \text{ K}^{-1}$ ) which describes the storage of energy (enthalpy) in bonds that break or weaken on increasing temperature.

The properties of water appear as a hierarchy of effects playing a role at different temperatures and pressures. These facts are mostly derived from molecular modeling, not from experimental data. Figure 1.2 shows these effects, where “Structural” bounds indicate where water is more disordered when compressed, the “Dynamic” bounds indicate where diffusion increases with density, and the “Thermodynamic” bounds show where there is a temperature of maximum den-

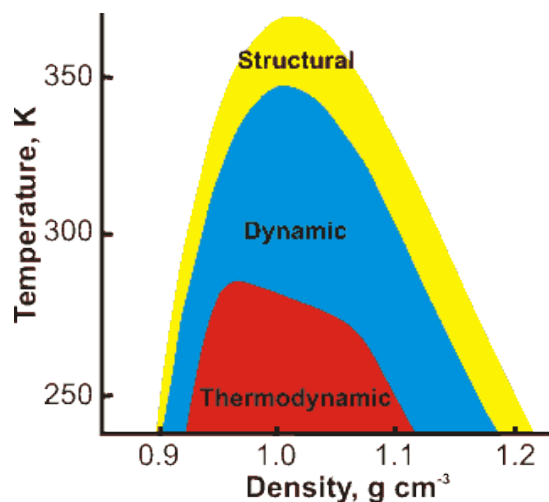


Figure 1.2

sity. As density always increases with increasing pressure, a similar relationship holds with pressure along the horizontal axis.

The rest of the dissertation is organized as follows. First in Chapter 2, some facts about the role of water at chemical and biological interfaces are reviewed. These facts serve to motivate, build an effective microscopic description at interfaces that is latter studied and used throughout the text. Next in chapter 3, numerical techniques for simulating the chemical and biological interfacial systems as well as multipolar water models used to study the vibrational spectroscopic of water is described. This chapter mainly includes methodology used throughout the work. Chapter 4 examines the dynamics and role of water at heterogeneous interfaces. It also includes the dynamics of chromophore (analyte), role of methanol as a co-solvent and thermodynamic study of intercalation process for some compounds of industrial relevance. Second part of this chapter discuss the dynamics and vibrational spectrum of water molecules on the hydroxylated silica surface. It also discuss the importance of higher order multipoles for water models to correctly account for electrostatic interactions. Chapter 5 take divergence and put emphasis on the role of water molecules for cooperative protein such as Scapharca dimeric hemoglobin and human hemoglobin. In these proteins water dynamics plays an important role for interfacial structural transition, witnessing cooperative behavior of protein. This chapter also discuss ligand dynamics inside the protein, reminiscent of the photolysis experiment. It clearly demonstrate the coupled dynamics between interfacial water molecules and ligand migration as well as migration pathway of ligand to the solvent.

In particular many questions have been addressed for experimental findings which were not explicitly discussed before. Second part of this chapter discuss the quaternary structural transition in human hemoglobin (HbA). This section mainly discuss the factor which mostly triggers the structural transitions.





# 2

## HISTORICAL NOTE ON THE ROLE OF WATER AT DIFFERENT INTERFACES

---

*This chapter briefly describes the previous work done for water at solid and biological interfaces*

*Thus one is led still more nearly inevitably to conclude that water is not a simple substance at all*

**Lavoisier**

## Contents

---

<b>2.1</b>	<b>Water at different interfaces . . . . .</b>	<b>10</b>
2.1.1	Water at solid silica interfaces . . . . .	11
2.1.2	Water at different biological interfaces . . . . .	12

---

---

This chapter begins by addressing some preliminaries about the water molecule and its implications for the condensed phases of water are shown. These facts are used to motivate and perform molecular simulations of water molecules in different environment. Interfacial properties of water molecules are briefly described in connection with heterogeneous environment of both chemical and biological importance.

Water at interfaces is also a field of great interest, in its theoretical aspects as well as due to development of diverse experimental techniques. Important new developments in the field involve the properties of water (and ice) next to various types of solid interfaces relevant to broad range of physicochemical phenomena and technological processes such as corrosion, lubrication, heterogeneous catalysis and electrochemistry. With the advent of scanning electron microscopy (STM) it became possible to simply “see” at an atomistic local level what structures water forms when it sticks to metal surfaces. Vibrational sum frequency generation spectroscopic techniques helps to look deeper into the microscopic structuring at water/air interface. Depending on the nature of an interface (which may include charges, hydrogen-bonding sites, dipoles or hydrophobicity/hydrophilicity), structure and dynamics of the water surface should differ from that in the bulk.

Two of the most natural questions to ask regarding water near an interface are: (1) How is the water structure near a solid interface different (if it is different at all) from bulk water? (2) If the structure of vicinal water is, indeed, different, how far from the interface does the altered structure penetrate into the bulk region? The properties of water in the vicinity of an interface are different than the properties of bulk water, giving rise to many surprising and intriguing effects.<sup>5</sup> Depending upon the nature of the interface, water shows totally distinct behavior. One of the key factor is the hydrophobicity or hydrophilicity of the interface. Hydrophobic interfaces break the hydrogen bond structure of water, and the interfacial water molecules reorient to achieve their minimum energy.<sup>6</sup> One of the method to determine the nature of solid interface is to exactly calculate the contact angle between water and the surface. This contact angle ranges from  $180^\circ$  at air to  $0^\circ$  for very hydrophilic interfaces, where droplet of water spread on the surface and contact angle can't be determined anymore. Hydrophilic surfaces are much more abundant in nature. There is a much larger variety of chemical motifs and just to name a few, polar surfaces such as biological membranes, surfaces of ionic crystals, charged surfaces, or metallic surfaces, which attract polar water molecules through the strong electrostatic force, all posses hydrophilic surface character, i.e., a contact angle of less

than  $90^\circ$ . Contrary to hydrophobic interfaces existence of ordered water is evident near certain water/solid interfaces. In the past few years there has been enormous amount of research being focused on the waters interaction with different surfaces through experiments and computer simulations. These study mainly includes water on different metal surfaces, hydroxylated and oxide surfaces.

Water molecules have also proved to be an integral part of most protein-protein,<sup>7,8</sup> protein-DNA<sup>9</sup> and protein-ligand<sup>10</sup> interactions. The driving force for binding depends not only on the interaction of the biological molecules with each other but the energetic cost for the necessary removal of hydration water and the energetic gain for the subsequent molecular rearrangement of the hydration water molecules. The hydration of biological macromolecules is very important for their three dimensional structure and activity.<sup>11–14</sup> Indeed protein lacks activity in the absence of hydrating water. The aqueous structuring around proteins is affected out to at least a nanometer from its surface or 2 nm between neighboring proteins, as shown by terahertz spectroscopy.<sup>15</sup> Some water molecules interact with the surface, reorienting both themselves and the surface groups whereas other water molecules link these to the bulk in an ordered manner whilst remaining in dynamically active.<sup>16</sup> In solution proteins possess a conformational flexibility, which encompasses a wide range of hydration states, not seen in the crystal or in non-aqueous environments. One of the good examples for protein allostery where water plays an essential role is *Scapharca dimeric hemoglobin* from Mollusc.<sup>17</sup>

## **2.1** Water at different interfaces

---

The properties of water have been systematically studied for more than 80 years. Unfortunately, these studies have resulted in only a modest increase in our understanding of water structure. The structural and dynamical behavior of water around an interface is highly dependent upon the chemical or biological morphology as well as the thermodynamic nature of the interface (solid, liquid or gas). These interfaces include solid mineral surface, water-air interface, water biological interfaces. The presence of solid interface provides an environment for studying diverse processes, such as sorption/desorption, precipitation/dissolution, as well as surface mediated chemistry of electron transfer,<sup>18–20</sup> hydrolysis<sup>21</sup> and various photochemical transformations. Water-air

interface is of fundamental importance for aqueous chemistry, where reactivity is governed by the hydrogen bond (H-bond) structure of water at the interface.<sup>22–26</sup> Water dynamics around biological interfaces have significant impact on stability, function and structure of proteins. Another important aspect of this is related to the packing of water around protein interface, because of its implications the way protein interacts with other molecules<sup>27</sup> and which was a matter of discussion in early 1970s.<sup>28–30</sup> Rest of the chapter discuss about water behavior around silica and protein interface.

### 2.1.1 Water at solid silica interfaces

Silica and silica based materials are widely used in chemistry and materials science due to their importance in many diverse fields such as chromatography,<sup>31–35</sup> microelectronics, metal-supported catalysis<sup>36,37</sup> and medicine.<sup>38</sup> Indeed, silica as stationary phase for liquid chromatography system is used in the pharmaceutical industry, in the analysis of contaminants, pesticides, bioanalytes, and drug residues in drinks and foodsamples, and in medical or environmental tests. The topology of these materials are key towards understanding their applications. Molecular level understanding of water behavior at these interfaces are still quite limited. There are different studies done on silica water interface, always from different perspective. The spectroscopic studies mainly involve IR,<sup>39–41</sup> Raman and Solid-state NMR.<sup>42,43</sup> The IR study mainly include vibrational frequencies for dangling “-OH group” and “H-bonded” silanol groups. Solid-state NMR has been a choice for studying structure of silicates and silica polymorph and their local structuring<sup>44</sup> as well as bulk structure.<sup>45</sup>

Apart from the experimental techniques mentioned above there are many groups who work on modeling the silica force field, however these force fields doesn't involve water reaction with terminal SiOH. To specify the H-bonded properties at the surface FFSiOH has been proposed.<sup>46</sup> For the silica/water system Garofalini et al.,<sup>47,48</sup> Singer et al.,<sup>49,50</sup> and Du et al.<sup>51</sup> have extended the silica force field to include the interaction with water. Force field studies have focused on mainly on quartz,<sup>52–55</sup> and cristobalite (high-temperature polymorph of silica) surface. De Leeuw et al. studied the  $\alpha$ -(0001) hydroxylated quartz-water interface.<sup>56</sup> The important findings from these studies conclude liquid like behavior of water above the SiOH

surface, together with preferred orientation of water,  $H_{\text{up}}$  above the dangling -OH group and  $H_{\text{down}}$  configuration between the SiOH groups concluded by Wander and Clark.<sup>57</sup> Argyris et al.<sup>58,59</sup> studied C(111) water interface using the SPC model for water and a 12-6 Lennard- Jones potential for Si-water interaction. In all cases, the perturbation of the water structure due to the surface interaction decreases as the distance from the solid substrate increases, bulk water properties being recovered for distances greater than  $\approx 14$  Å. The (001) quartz-water interface has also been recently investigated by Sulpizi et al.<sup>60</sup> using BLYP, who confirm that the H-bond network on this surface is partially maintained: two types of silanols, “in plane” and “out of plane” are present on the surface. The “in plane” silanols are H-bond donor to a silanol (strong H-bond), and the “out of plane” ones are H-bond donor to water.

All the above studied has used different ways to characterize the dynamics and structure of water near the solid interfaces<sup>61-63</sup> which includes density of water perpendicular to the surface,<sup>64</sup> water -OH bond angular distribution<sup>65</sup> close to the surface, mean square displacement, hydrogen bond network<sup>65-67</sup> and vibrational spectroscopic features of water close to the wall.

### **2.1.2** Water at different biological interfaces

---

Water at biological interfaces plays a crucial role in cell<sup>13,68</sup> and molecular biology.<sup>69,70</sup> Water is essential for the stability and function of biological macromolecules, proteins and DNA. It is physiologically harmless and is the main component of living beings: approximately 60 % by weight of an adult human body is due to its water content. Most of this water (60 %) are confined in cells, while the remaining water flows through tissues and in narrow blood vessels. Hydration plays an important role in the assembly of a protein’s structure and dynamics.<sup>11</sup> For example, enzymes and proteins need to be suspended in solution to change their conformation and to adopt their active structures, and water governs the rate of recognition that proteins, nucleic acids and membranes have of ligands and drugs.<sup>71</sup> Our failure in fully understanding the behavior of water is one of the main limitation we have in predicting protein structures and in designing drugs. For example, recent data shows how water plays a fundamental role in determining the proteins folding rate<sup>72</sup> and the hydrophobic collapse of proteins<sup>73</sup> mediated by the water molecules. Other

examples include protein-protein interactions that are affected by the dynamics of the hydration-water layer.<sup>74</sup> Water molecules in protein chemistry can be classified into three categories, namely strongly bound waters;<sup>75,76</sup> water molecules that occupy the internal cavities;<sup>77</sup> and water molecules that are attached to the surface of protein.<sup>78,79</sup> The water molecules that make up the hydration shell in the immediate vicinity of the surface are particularly relevant to the function and, are termed as ‘*biological water*’ or ‘*bound water*’, this distinction has been discussed clearly by Nandi and Bagchi<sup>80,81</sup> in relation to their dielectric relaxation time scales. These water molecules have been found to have properties that are detectably different from those of the bulk, e.g. they exhibit lower vapor pressure, lower mobility, lower freezing point, etc.<sup>82</sup> Such definition have certain limitations. Different experimental techniques measure different properties, and some water molecules may be considered “bound” by one method but not by others. The nature of this shell “layer” has been the focus of numerous studies both theoretically<sup>83-86</sup> and experimentally,<sup>87,88</sup> yet there is no generalized picture of the dynamics at the local molecular level. Experimental techniques like X-ray crystallography,<sup>89</sup> neutron diffraction<sup>90</sup> and molecular dynamics<sup>11,86,91,92</sup> simulations have shown that at protein surfaces, water molecules are site selective and highly restrictive in their dynamical motion. One of the examples is the neutron diffraction study of carboxymyoglobin<sup>93</sup> which was followed by molecular dynamics simulations<sup>85</sup> which clearly demonstrate that out of 89 crystal water molecules, 4 remain with the protein for the entire simulations and rest of the water molecules were continuously exchanging with the solvent. Water dynamics at the surface of proteins happens at different time scales, which gives us an idea of strong and weak bound water molecules around the biomolecule. These time scales can be measured by dielectric measurement<sup>94,95</sup> and NMR experiments.<sup>96</sup> Ordered water molecules are observed by crystallography and nuclear magnetic resonance to mediate protein-ligand interactions.<sup>97</sup>

From these experiments it is found that time scales for water dynamics vary from few picoseconds to nanoseconds time regime. Recently biological water dynamics at the femtosecond resolution was studied for protein surface and using a single native Trp residue by A. H. Zewial et. al.<sup>79</sup> Extended depolarized light scattering (EDLS) measurements<sup>98</sup> have been recently employed to investigate the dynamics of water solvating biological molecules, giving evidence of the presence of two different dynamical regimes among water molecules. However molecular dynamics simulations<sup>84</sup> were performed to completely understand the results obtained from EDLS experiments. These

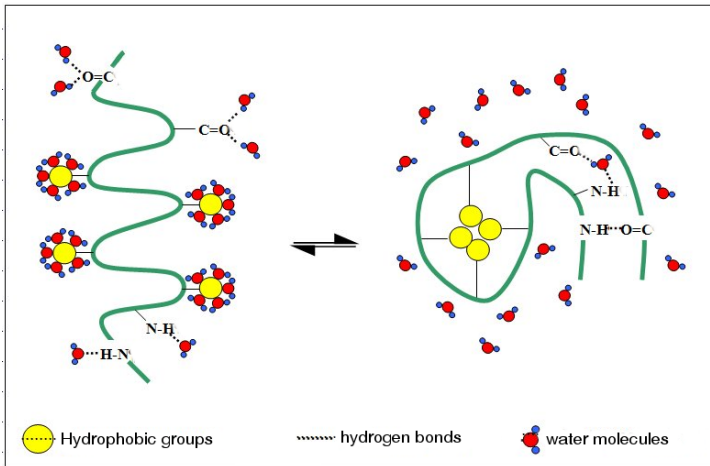


**Figure 2.1:** Schematic representation of the various ways that water molecules are implicated in protein structure and stability. The hydrophobic interaction, water clustering and hydrogen bonds are shown for different functional groups of a protein

studies also concluded two time scales for solvated water dynamics around the protein.

There are different types of interactions present in biomolecules. These interactions could be intermolecular or intramolecular. Electrostatic interactions, known as “salt bridges” (coulomb interaction between charge sites), van der Waals interactions plays an important role in the stability of the proteins. van der Waals interactions are very weak interactions and non-directional as well but they are present everywhere in biomolecules. The “hydrophobic effect” and “hydrogen bonding” are the two major factors for the protein structure, stability and function.<sup>99</sup> The hydrophobic effect is considered to be one of the major driving force for globular protein folding. It effects by moving the non-polar side chains of the protein towards the core of protein. This conformational change leads the water to form small clusters around the hydrophobic groups which decrease the entropy of the system. On the other hand water gains a lot of entropy by forming these clusters. These phenomenon decrease the overall free energy of the protein and make it more stable. These hydrophobic interactions are clearly demonstrated in the work done by Frank and Evans<sup>100</sup> and also by Kauzmann.<sup>101</sup> These hydrophobic collapse are favored by other polar functional groups which are exposed towards the solvent and forms hydrogen bonds. These hydrogen bonds plays an important role for



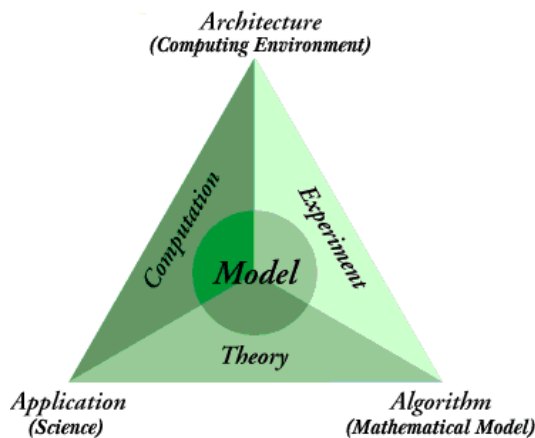
enthalpy contribution. The water molecules shows details balance between entropy and enthalpy of the protein system. The contribution of the H-bond is quite small from energy point of view, however these hydrogen bonds provide intramolecular stability to the protein. The hydrophobic collapse is shown as a cartoon in Figure 2.1



# 3

## THEORETICAL AND COMPUTATIONAL METHODS

---



*The sciences do not try to explain, they hardly even try to interpret, they mainly make models. By a model is meant a mathematical construct which, with the addition of certain verbal interpretations, describes observed phenomena. The justification of such a mathematical construct is solely and precisely that it is expected to work—that is, correctly to describe phenomena from a reasonably wide area.*

**John von Neumann**

## Contents

---

<b>3.1</b>	<b>Molecular dynamics simulation</b>	<b>19</b>
3.1.1	Historical note	19
3.1.2	Basic Theory	19
<b>3.2</b>	<b>Force Field</b>	<b>22</b>
3.2.1	Point charge force field	22
3.2.2	Multipolar force field (MTP)	24
<b>3.3</b>	<b>Analysis Methods</b>	<b>26</b>
3.3.1	Umbrella Sampling	27
3.3.2	Thermodynamic Integration	30

---

The structural and energetic information about any living system can be projected into the motion of their respective building blocks which indeed are quantum particles; atom and molecules. However, in order to study a system like protein it is unlikely to apply the theory of quantum mechanics, but as a crude approximation we can consider those atoms as classical particles (charged/uncharged), connected by springs to each other to form a larger molecular systems. The whole idea of classical molecular dynamics simulation is based on these approximations, where atoms are treated as classical particle. In the following we will discuss about the basics of molecular dynamics simulations, force field and about the method used to estimate free energy from simulations.

## 3.1 Molecular dynamics simulation

---

### 3.1.1 Historical note

---

It is now over 50 years since the first computer simulation of an assembly of hard spheres was carried out by MD, in conjugation with same system studied by Monte Carlo method by Alder and Wainwright<sup>102</sup> and Jacobson et. al.<sup>103</sup> After that Rahman did the simulations for liquid Argon (Ar) and later in the year 1971 Rahman and Stillinger performed liquid simulation of water. The method of molecular simulations get wider applicability after world war II, to study the problem of particle systems. In the year 1977, the first molecular dynamics simulation for a protein was done by Martin Karplus, J. A. Mccammon and B. R. Gelin.<sup>104</sup> In the 80's there was much improvement in the method to perform free energy calculations, protein-ligand docking calculations and since then, a continuous development of potentials and sampling techniques has been carried out.

### 3.1.2 Basic Theory

---

The molecular dynamics simulation method is based on numerically solving Newton's equation of motion,  $\mathbf{F} = m\mathbf{a}$ , where  $\mathbf{F}$  is force exerted on the

particle and  $m$  is its mass and  $\mathbf{a}$  is its acceleration. Knowing the force on each atom, it is possible to determine the acceleration of each atom in the system. Integration of the equations of motion then yields a trajectory that describes the positions, velocities and accelerations of the particles as they vary with time. From this trajectory, the average values of properties can be determined. The method is deterministic; once the positions and velocities of each atom are known, the state of the system can be predicted at any time in the future or the past.

For any given system of  $N$  classical interacting particles, the total energy of the system is represented by the Hamiltonian  $\mathcal{H}$  which is the sum of the kinetic and potential energy of the system, denoted by  $T$  and  $V$ . This is represented mathematically in the following equation

$$\mathcal{H}(\mathbf{p}, \mathbf{r}) = \mathcal{H}(\mathbf{p}_1, \mathbf{p}_2, \dots, \mathbf{p}_N, \mathbf{r}_1, \mathbf{r}_2, \dots, \mathbf{r}_N) = \sum \mathbf{p}_i^2 / 2m + \mathcal{U}(\mathbf{r}_1, \mathbf{r}_2, \dots, \mathbf{r}_N) \quad (3.1)$$

The equation of motion is derived from Hamilton's equation and is written as follows

$$\dot{\mathbf{r}}_i = \frac{\partial \mathcal{H}}{\partial \mathbf{p}_i} = \frac{\mathbf{p}_i}{m_i} \quad (3.2)$$

$$\dot{\mathbf{p}}_i = -\frac{\partial \mathcal{H}}{\partial \mathbf{r}_i} = -\frac{\partial \mathcal{U}}{\partial \mathbf{r}_i} = \mathbf{F}_i \quad (3.3)$$

The classical state of a system at any instant in time can be determined by specifying the complete set of particle positions and corresponding momenta.

To make the connection to statistical mechanics a phase space vector is defined:

$$\mathbf{x} = (\mathbf{p}_1, \mathbf{p}_2, \dots, \mathbf{p}_N, \mathbf{r}_1, \mathbf{r}_2, \dots, \mathbf{r}_N) \quad (3.4)$$

The classical state of a system correspond to a single point in the  $6N$  dimensional phase space. This space is thus the union of all possible classical states of the system. Properties of the equation of motion are described as follows:

**Time reversal symmetry** The equations of motion take the same form when the transformation  $t \rightarrow -t$  is made. It means that the physics is independent of the flow of time.

**Hamiltonian is conserved**

$$\frac{d\mathcal{H}}{dt} = \sum_{i=1}^N \left[ \frac{\partial \mathcal{H}}{\partial t} \mathbf{r}_i + \frac{\partial \mathcal{H}}{\partial t} \dot{\mathbf{p}}_i \right] = \sum_{i=1}^N \left[ \frac{\partial \mathcal{H}}{\partial t} \frac{\partial \mathcal{H}}{\partial \mathbf{r}_i} - \frac{\partial \mathcal{H}}{\partial t} \frac{\partial \mathcal{H}}{\partial \mathbf{p}_i} \right] \quad (3.5)$$

The conservation of the Hamiltonian is equivalent to the conservation of the total energy of the system and provides important link between molecular dynamics and statistical mechanics. Statistical mechanics is based on Gibbs *ensemble* concept and connects the microscopic details of a system to physical observables such as equilibrium thermodynamics properties, transport coefficients and spectra.

**Integrator** A Molecular Dynamics program requires a good algorithm to integrate Newton's equation of motion. However algorithm to numerically solve the equation of motion must follow certain criterion, mainly conservation of energy, time-reversibility, computationally efficient, enables long integration time step and evaluates force at every time step. There are different integration schemes known like Verlet,<sup>105</sup> Velocity-Verlet, Leap-frog,<sup>106</sup> Predictor-Corrector and Gear Predictor-Corrector.<sup>107</sup> Among all these integrator the most important, efficient and widely used is the Velocity-Verlet integrator. The Velocity-verlet algorithm is modification of Verlet algorithm which is described as follows. To derive it, we start with a Taylor expansion of the particle's coordinate around the time  $t$ , once in the forward direction and once in the backward direction.

$$\mathbf{r}(t + \Delta t) = \mathbf{r}(t) + \mathbf{v}(t)\Delta t + \frac{\mathbf{f}(t)\Delta t^2}{2m} + \frac{\Delta t^3}{3!} \ddot{\mathbf{r}} + O(\Delta t^4) \quad (3.6)$$

$$\mathbf{r}(t - \Delta t) = \mathbf{r}(t) - \mathbf{v}(t)\Delta t + \frac{\mathbf{f}(t)\Delta t^2}{2m} - \frac{\Delta t^3}{3!} \ddot{\mathbf{r}} + O(\Delta t^4) \quad (3.7)$$

Adding the above eq 4.7 and 3.7, and rearranging we obtain:

$$\mathbf{r}(t + \Delta t) \approx 2\mathbf{r}(t) - \mathbf{r}(t - \Delta t) + \frac{\mathbf{f}(t)\Delta t^2}{2m} + O(\Delta t^4) \quad (3.8)$$

This is the basic form of the Verlet algorithm. Since we know from Newton's equations,  $\mathbf{a}(t)$  is just the force divided by the mass, and the force is in turn a function of the positions  $\mathbf{r}(t)$  given by  $\mathbf{a}(t) = -\frac{1}{m}\nabla V(\mathbf{r}(t))$ . This algorithm is simple to implement, but the truncation error of the algorithm is of the order of  $\Delta t^4$ . A problem with this version of the Verlet algorithm is that velocities are not directly generated. One can compute the velocities from the positions by using

$$\mathbf{v}(t) = \frac{\mathbf{r}(t + \Delta t) - \mathbf{r}(t - \Delta t)}{2\Delta t} + O(\Delta t^2) \quad (3.9)$$

but the error associated with the estimation of velocity is of the order of  $\Delta t^2$ . To overcome this problem, a different variant of the Verlet algorithm is shown below, known as Velocity-Verlet method. In this scheme, the positions and velocities are computed at equal times.

$$\mathbf{r}(t + \Delta t) = \mathbf{r}(t) + \mathbf{v}(t)\Delta t + \frac{\mathbf{f}(t)\Delta t^2}{2m} \quad (3.10)$$

$$\mathbf{v}(t + \Delta t) = \mathbf{v}(t) + \frac{\mathbf{f}(t + \Delta t) + \mathbf{f}(t)}{2m}\Delta t \quad (3.11)$$

However the new velocities are computed only after the new positions have been computed, and from these the new forces. In practice, almost every classical MD programs uses Verlet or Leap-frog algorithm to integrate Newton's equation of motion.

## 3.2 Force Field

In molecular dynamics a molecule is described as a series of charged points (atoms) linked by springs (bonds). To describe the time evolution of bond lengths, bond angles and torsions, also the non-bonding van der Waals and electrostatic interactions between atoms, one uses a *force field*. The force field is a collection of equations and associated constants designed to reproduce molecular geometry and selected properties of tested structures. There are many commercially available force field namely CHARMM,<sup>108</sup> AMBER,<sup>109</sup> GROMOS,<sup>110</sup> OPLS<sup>111</sup> etc. All these force field are known as classical force field. There are another class of force field known as Polarizable force field such as AMOEBA,<sup>112</sup> SIBFA.<sup>113</sup> There are few reactive force field namely ReaxFF,<sup>114</sup> RWFF.<sup>115</sup> Following is the description for the force field.

### 3.2.1 Point charge force field

The basic functional form of a force field encapsulates both bonded terms relating to atoms that are linked by covalent bonds, and nonbonded (also



called "noncovalent") terms describing the long-range electrostatic and van der Waals forces. The specific decomposition of the terms depends on the force field, but a general form for the total energy in an additive force field can be written as  $E_{total} = E_{bonded} + E_{nonbonded}$ , where the components of the covalent and noncovalent contributions are given by the following summations:

$$\begin{aligned} E_{bonded} &= E_{bond} + E_{angle} + E_{dihedral} \\ E_{non-bonded} &= E_{electrostatic} + E_{vanderwaals} \end{aligned} \quad (3.12)$$

The general form of the potential energy function is as follows:

$$\begin{aligned} \mathcal{U}(\vec{R}) &= \underbrace{U_{bond} + U_{angle} + U_{dihedral}}_{bonded} \\ &\quad + \underbrace{U_{electrostatic} + U_{vanderwaals}}_{nonbonded} \end{aligned} \quad (3.13)$$

The functional form of the  $U_{bond}$ ,  $U_{angle}$  and  $U_{dihedral}$  is written in the following equations

$$\sum_{i=bonds} K_i^{bonds} (\mathbf{r}_i - \mathbf{r}_0)^2 \quad (3.14)$$

$$\sum_{i=angle} K_i^{angles} (\theta_i - \theta_0)^2 \quad (3.15)$$

$$\sum_{i=dihedrals} K_i^{dihedrals} [1 + (\cos n_i \phi_i + \delta)] \quad (3.16)$$

and the functional form for  $U_{electrostatic}$  and  $U_{vanderwaals}$  are described as follows

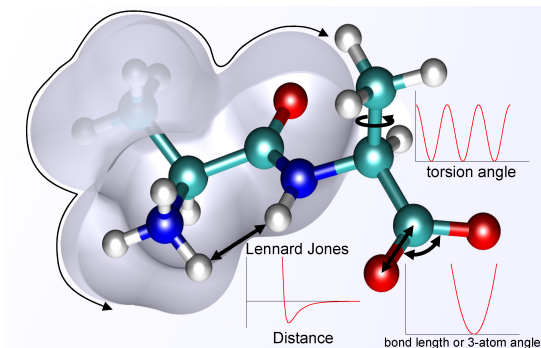
$$\sum_i \sum_{j \neq i} \frac{q_i q_j}{\mathbf{r}_{ij}} \quad (3.17)$$

$$\sum_i \sum_{j \neq i} 4\epsilon_{ij} \left[ \left( \frac{\sigma_{ij}}{\mathbf{r}_{ij}} \right)^{12} - \left( \frac{\sigma_{ij}}{\mathbf{r}_{ij}} \right)^6 \right] \quad (3.18)$$

All the  $K$ 's appearing in the above equation corresponds to the value of force constant derived experimentally or from high level of ab initio calculations.  $r_0$ ,  $\theta_0$  and  $\phi$  correspond to the equilibrium bond length, bond angle and dihedral angle. In the above equation the  $\varepsilon$  denotes the well depth of the Lennard Jones potential and  $\sigma$  represent the LJ radius.

The bond and angle terms are usually modeled as harmonic oscillators that do not allow bond breaking. A more realistic description of a covalent bond at higher stretching is provided by the more expensive Morse potential. The functional form for the rest of the bonded terms is highly variable. Proper dihedral potentials are usually included. Additionally, *improper torsional* terms may be added to enforce the planarity of aromatic rings and other conjugated systems, and *cross-terms* that describe coupling of different internal variables, such as angles and bond lengths. Some force fields also include explicit terms for hydrogen bonds. The non-bonded terms are most computationally intensive because they include many more interactions per atom. A popular choice is to limit interactions to pairwise energies. The van der Waals term is usually computed with a Lennard-Jones potential and the electrostatic term with Coulomb's law, although both can be buffered or scaled by a constant factor to account for electronic polarizability and produce better agreement with experimental observations.

**Figure 3.1:** A schematic representation of different contributions to force field



### 3.2.2

### Multipolar force field (MTP)

Atomic interactions in classical force fields are roughly divided into short-ranged, bonded interactions and long-ranged, nonbonded interactions. Nonbonded inter-

action potentials include terms modeling the electrostatic, exchange-repulsion and dispersion interactions, and are largely responsible for the inaccuracies in classical force fields.<sup>116</sup> Electrostatic interactions have been modeled using an atom-centered point charge (“partial charge”) representation of the molecular charge density.<sup>117</sup> The most popular methods for extracting charges from molecular wavefunctions are based on fitting atomic charges to the molecular electrostatic potential (MEP), computed with *ab initio*, density functional theory (DFT) or semiempirical wave functions. The charge fitting procedure consists of minimizing the squared deviation between the Coulombic potential produced by the atomic charges and the MEP. Such representations are believed to be an important source of error in current force fields.<sup>116</sup> The idea behind the multipolar force field is to accurately describe the electrostatic potential of the molecule. The fit to the MEP can be improved either by adding more charge sites (3) or by including higher order multipoles at the atomic sites. A realistic physical molecular representation requires dipole moments (e.g., for the lone pairs), quadrupole moments (e.g., for the  $\pi$  bonds), etc. There are two ways to perform a multipole expansion: the one-center multipole expansion which is taken with respect to a center in a molecule (i.e., the center of mass), or the distributed multipole analysis (DMA) first introduced by Stone,<sup>116</sup> where distributed multipole moments are assigned to several sites in the molecule (i.e., atoms and bond mid-points).

In a multipole expansion, the electrostatic potential or energy of a charge distribution is expanded in powers of the Coulomb potential (or Green’s function)  $1/R = 1/|\mathbf{x} - \mathbf{x}'|$  where  $\mathbf{x}'$  is the position of a charge element and  $\mathbf{x}$  is the point in space where the electrostatic potential is evaluated. Point-charge descriptions corresponding to the first term in a multipole expansion or the Coulomb term in standard classical force fields.<sup>118,119</sup> For MTP the molecular multipole moments are determined using DMA. It includes a partitioning of the electron density in molecular orbital space and an integration of  $\rho(r)$  over an appropriately defined space for all desired multipole ranks. The Coulomb interaction of a standard force field as described by the first term in Equation 3.17 is replaced in MTP by a description of multipole expansion for a selected number of molecules in the system. Consider a localized charge density  $\rho(\mathbf{x}')$  generating an electrostatic potential (ESP)  $\Phi(\mathbf{x})$  at position  $\mathbf{x}$ .

$$4\pi\epsilon_0\Phi(\mathbf{x}) = \int d\mathbf{x}' \frac{\rho(\mathbf{x}')}{|\mathbf{x} - \mathbf{x}'|} \quad (3.19)$$

A Taylor series expansion of  $1/R = 1/|\mathbf{x} - \mathbf{x}'|$  provides the following multipole

expansion for  $\Phi$  in Cartesian coordinates.

$$4\pi\epsilon_0\Phi(\mathbf{x}) = q\frac{1}{R} + \frac{\mu_a R_a}{R^3} + \frac{1}{3}\Theta_{\alpha\beta}\frac{3R_\alpha R_\beta - R^2\delta_{\alpha\beta}}{R^5} + \dots \quad (3.20)$$

where  $\mu_\alpha$  is the component  $\alpha$  of the dipole moment  $\mu$ ,  $\Theta_{\alpha\beta}$  is the component  $\alpha\beta$  of the second-rank quadrupole moment tensor  $\Theta$ , and the Einstein summation convention is applied. The parametrization protocol<sup>120</sup> for multipole moments on each atomic site for a given molecule, is an extension of the work done by Kramer et. al.<sup>121</sup> All multipole moments will be expressed in spherical coordinates  $Q_{lk}$ , where  $l$  denotes the order of the expansion and  $k$  is used to iterate over the  $2l + 1$  coefficients.

$l = 0$ : The charge  $q$  is invariant under coordinate transformation:  $Q_{00} = q$

$l = 1$ : The dipole moment  $\mu$  becomes  $Q_{10} = \mu_z$ ;  $Q_{11c} = \mu_x$ ; and  $Q_{11s} = \mu_y$

$l = 2$ : The symmetry and traceless property of  $\Theta$  imply that only five coefficients characterize the quadrupole moment:  $Q_{20} = \Theta_{zz}$ ;  $Q_{21c} = 2\Theta_{xz}/\sqrt{3}$ ;  $Q_{21s} = 2\Theta_{yz}/\sqrt{3}$ ;  $Q_{22c} = (\Theta_{xx} - \Theta_{yy})/\sqrt{3}$ ; and  $Q_{22s} = 2\Theta_{xy}/\sqrt{3}$  As a means to validate the MTP force field, we calculated density of the compounds in the pure liquid state, enthalpy of vaporization and absolute hydration free energies  $\Delta G_{hyd}$  of the fragments used in the parametrization and compared them with experimental values (if available).

The versatility and robustness of MTP has already been demonstrated for different molecular systems.<sup>122–126</sup> In these studies MTP successfully unravelled the conformational dependence of vibrational shifts and frequency splittings of CO, water sensed in the electrostatic field and water bending vibrational frequency shifts in condensed-phase environments.

### 3.3 Analysis Methods

The free energy is the most important thermodynamic quantity to calculate in any physical, chemical or biological systems and are usually known as Helmholtz free energy or Gibbs free energy. The free energy (or relative free energy) of a system are very useful parameters to follow chemical reactions, phase transitions, critical phenomena or any other transformations. We can never calculate absolute free energies (since we do not have an appropriate reference state), however relative free energies can be found using several different computational techniques. The calculation of free-energy differences

is one of the main challenges in computational biology and chemistry. The MD methods are not efficient in estimating certain statistical averages and one of those quantity is “free energy”. These quantities are hard to estimate because using the approach of MD direct calculation of free energy requires more sampling over high-energy configurations. To drive a system over an energy barrier, one can either (1) modify the energy expression in order to reduce the barrier, or (2) restrict the sampling space to all degrees of freedom, but the reaction coordinate describing the transition over the barrier. However, there are different methods to overcome this problem which includes umbrella sampling,<sup>127,128</sup> Thermodynamic integration,<sup>129–132</sup> Free energy perturbation method,<sup>133</sup> adaptive methods,<sup>134</sup> non-equilibrium work,<sup>135</sup> metadynamics.<sup>136</sup> Out of these methods I will describe two of them used in different projects, which are *Umbrella sampling* and *Thermodynamic integration* method.

### 3.3.1 Umbrella Sampling

Umbrella sampling, biased molecular dynamics (MD), is one of the methods that provide free energy along a reaction coordinate. It was developed by Torrie and Valleau<sup>127,128</sup> based on previous work.<sup>137–139</sup> The canonical partition function  $Q$  of a system can be calculated via an integral over the whole phase space, i.e., configuration space and momentum space. If the potential energy  $E$  is independent of the momentum, the integral over the latter is a multiplicative constant to  $Q$ , which can be ignored. Then  $Q$  is obtained as:

$$Q = \int \exp[-\beta E(r)] d^N \mathbf{r} \quad (3.21)$$

with  $\beta=1/k_B T$ ,  $k_B$  being the Boltzmann’s constant,  $T$  being the absolute temperature. The free (Helmholtz) energy is related to  $Q$  via  $A = -1/\beta \ln Q$ . The canonical partition function involves a constant number of particles, constant volume, and a constant temperature. If the pressure, rather than the volume, is kept constant, the Gibbs free energy (usually denoted as  $G$ ) is obtained.

In chemical reactions, one is generally interested in free-energy differences between two states. If the two states differ by geometry (like a reactant and product of a reaction) then the integration in eq. 3.21 is done over a part of the coordinate space for each state. Two different thermodynamic states can be connected through a reaction coordinate ( $\xi$ ), which is a continuous parameter and can have different form. The reaction coordinate can be one-

or multi-dimensional. Often,  $\xi$  is defined as distance, angle, torsion or root mean square deviation from reference states. With  $\xi$  known, the probability distribution of the system along  $\xi$  can be evaluated by integrating out all degrees of freedom except  $\xi$ :

$$Q = \frac{\int \delta[\xi(r) - \xi] \exp[(-\beta E(r)) d^N \mathbf{r}]}{\int \exp[(-\beta E(r)) d^N \mathbf{r}]} \quad (3.22)$$

$Q(\xi) d\xi$  is interpreted as the probability of finding the system in a small interval  $d\xi$  around  $\xi$ . In computer simulations, the direct phase-space integrals used in Eqs. 3.21 and 3.22 are impossible to calculate. However, if the system is ergodic, i.e., if every point in phase space is visited during the simulation,  $Q(\xi)$  is equal to

$$P(\xi) = \lim_{t \rightarrow \infty} \frac{1}{t} \int_0^t \rho[\xi(t')] dt' \quad (3.23)$$

that is, the ensemble average  $Q(\xi)$  becomes equal to the time average  $P(\xi)$  for infinite sampling in an ergodic system. In Eq. 3.23,  $t$  denotes the time and  $\rho$  simply counts the occurrence of  $\xi$  in a given interval (of infinitesimal width in the exact equation and of finite width when calculating a histogram).

In umbrella sampling technique, an additional bias potential energy term is added to the system to ensure efficient sampling along the given reaction coordinate. This procedure can be applied to either one simulation or in different simulations (windows) of overlapping distributions. The idea of this method is to connect together different energy regions in the phase space. The bias potential  $w_i$  of window  $i$  is an additional term which depends upon the reaction coordinate, defined as  $E^b(r) = E^u(r) + w_i(\xi)$ , where ‘b’ and ‘u’ corresponds to bias and unbiased quantities. The biased distribution along the reaction coordinate ( $\xi$ ), obtained from the MD simulations can be written as

$$P_i^b(\xi) = \frac{\int \exp\{-\beta[E(r) + w_i(\xi'(r))]\} \delta[\xi'(r) - \xi] d^N \mathbf{r}}{\int \exp\{-\beta[E(r) + w_i(\xi'(r))]\} d^N \mathbf{r}} \quad (3.24)$$

In order to calculate unbiased free energy  $A_i(\xi)$ , one need to evaluate the unbiased distribution, which from eq. 3.22 can be written as:

$$P_i^u(\xi) = \frac{\int \delta[\xi'(r) - \xi] \exp[(-\beta E(r))] d^N \mathbf{r}}{\int \exp[(-\beta E(r))] d^N \mathbf{r}} \quad (3.25)$$

Because the bias depends only on  $\xi$  and the integration in the numerator is

performed over all degrees of freedom but  $\xi$ ,

$$P_i^b(\xi) = \exp[-\beta\omega_i(\xi'(r))] \times \frac{\int \exp\{-\beta[E(r)]\} \delta[\xi'(r) - \xi] d^N \mathbf{r}}{\int \exp\{-\beta[E(r) + \omega_i(\xi'(r))]\} d^N \mathbf{r}} \quad (3.26)$$

Using eq. 3.25 one can write

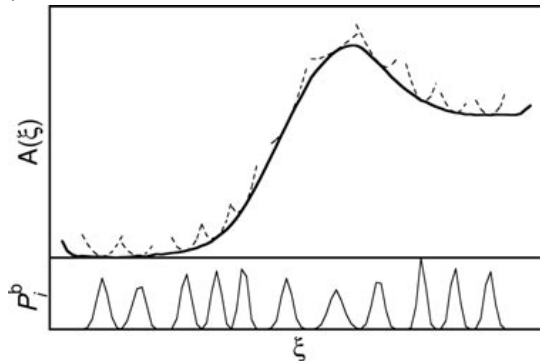
$$\begin{aligned} P_i^u(\xi) &= P_i^b(\xi) \exp[\beta\omega_i(\xi(r))] \times \frac{\int \exp\{-\beta[E(r) + \omega_i(\xi(r))]\} d^N \mathbf{r}}{\int \exp\{-\beta E(r)\} d^N \mathbf{r}} \\ &= P_i^b(\xi) \exp[\beta\omega_i(\xi(r))] \times \frac{\int \exp\{-\beta[E(r)] \exp\{-\beta\omega_i(\xi(r))\}\} d^N \mathbf{r}}{\int \exp\{-\beta E(r)\} d^N \mathbf{r}} \\ &= P_i^b(\xi) \exp[\beta\omega_i(\xi)] \langle \exp[-\beta\omega_i(\xi)] \rangle \end{aligned} \quad (3.27)$$

From eq. 3.27,  $A_i(\xi)$  can be readily evaluated.  $P_i^b(\xi)$  is obtained from an MD simulation of the biased system,  $\omega_i(\xi)$  is given analytically, and  $F_i = -(1/\beta) \ln \langle \exp[-\beta\omega_i(\xi)] \rangle$  is independent of  $\xi$ :

$$A_i(\xi) = -(1/\beta) \ln P_i^b(\xi) - \omega_i(\xi) + F_i \quad (3.28)$$

As long as each window spans the given range of  $\xi$  to be studied, Eq. 3.28 is sufficient to unbiased the simulation.  $A(\xi)$  is in any case only defined up to an additive constant; so in this case,  $F_i$  can be chosen arbitrarily. If the free-energy curves  $A_i(\xi)$  of more windows are to be combined to one global  $A(\xi)$ , see Figure 2, the  $F_i$  have to be calculated.

**Figure 3.2:** Global free energy (thick solid curve) and the contributions  $A_i$  of some of the windows (thin dashed curves). For clarity, only every third window is shown. At the bottom, the biased distributions  $P_i^b$  as obtained from the simulation are shown (thin solid curves).



### 3.3.2 Thermodynamic Integration

Thermodynamic Integration (TI) is another most common method for calculating free energy differences between two systems whose potential energies are given by  $\mathcal{U}_I$  and  $\mathcal{U}_{II}$ . The formalism to calculate the free energy difference is via Kirkwood's coupling parameter method.<sup>129</sup> We assume that potential energy  $\mathcal{U}$  depends linearly on a coupling parameter  $\lambda$  such that, for  $\lambda = 0$ ,  $\mathcal{U}$  corresponds to the potential energy of our reference system  $\mathcal{U}_I$  and for  $\lambda = 1$ , we recover the potential energy of the system of interest denoted by  $\mathcal{U}_{II}$ :

$$\begin{aligned}\mathcal{U}(\lambda) &= (1 - \lambda)\mathcal{U}_I + \lambda\mathcal{U}_{II} \\ &= \mathcal{U}_I + \lambda(\mathcal{U}_{II} - \mathcal{U}_I)\end{aligned}\quad (3.29)$$

We assume that the free energy of system I is known (either analytically or numerically). The partition function for a system with a potential energy function that corresponds to a value of  $\lambda$  between 0 and 1 is

$$Q(N, V, T, \lambda) = \frac{1}{\Lambda^{3N} N!} \int d\mathbf{r}^N \exp[-\beta\mathcal{U}(\lambda)] \quad (3.30)$$

The derivative of the Helmholtz free energy  $F(\lambda)$  with respect to  $\lambda$  can be written as an ensemble average:

$$\begin{aligned}\left(\frac{\partial F}{\partial \lambda}\right) &= -\frac{1}{\beta} \frac{\partial}{\partial \lambda} \ln Q(N, V, T, \lambda) \\ &= -\frac{1}{\beta Q(N, V, T, \lambda)} \frac{\partial Q(N, V, T, \lambda)}{\partial \lambda} \\ &= \frac{\int d\mathbf{r}^N (\partial\mathcal{U}(\lambda)/\partial\lambda) \exp[-\beta\mathcal{U}(\lambda)]}{\int d\mathbf{r}^N \exp[-\beta\mathcal{U}(\lambda)]} \\ &= \left\langle \frac{\partial\mathcal{U}(\lambda)}{\partial\lambda} \right\rangle_\lambda\end{aligned}\quad (3.31)$$

where  $\langle \dots \rangle_\lambda$  denotes an ensemble average for a system with a potential energy function  $\mathcal{U}(\lambda)$ . The free energy difference between systems II and I can be obtained by integrating Eq. 3.31:

$$F(\lambda = 1) - F(\lambda = 0) = \int_{\lambda=0}^{\lambda=1} d(\lambda) \left\langle \frac{\partial\mathcal{U}(\lambda)}{\partial\lambda} \right\rangle_\lambda \quad (3.32)$$



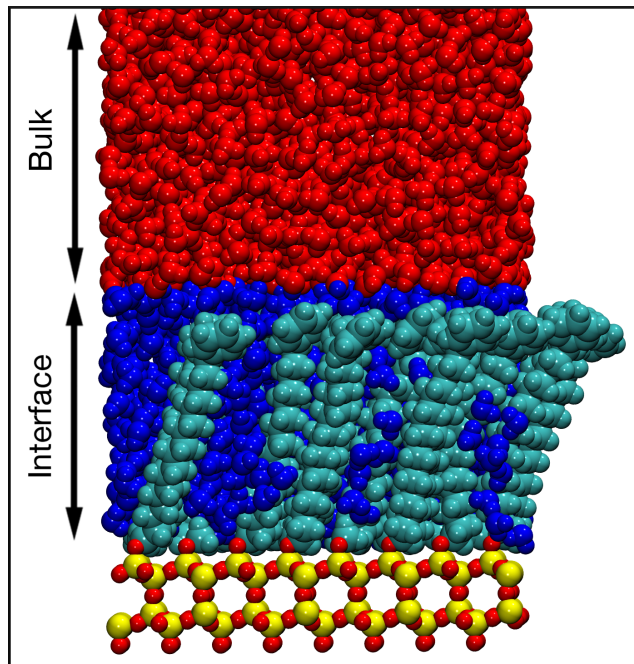
This expression evaluate free energy differences in terms of an ensemble average which can be calculated directly in a simulation. Artificial thermodynamic integration is often used to compute the difference in excess free energy, having importance in biomolecular modeling.<sup>140</sup>



# 4

## WATER AT HYDROXYLATED SILICA INTERFACE

---



## Contents

---

<b>4.1</b>	<b>Water at chromatographic interfaces . . . . .</b>	<b>35</b>
4.1.1	Theoretical and computational methods . . . . .	36
4.1.2	Molecular Dynamics simulations . . . . .	39
4.1.3	Analysis of the Trajectories . . . . .	40
<b>4.2</b>	<b>Results . . . . .</b>	<b>40</b>
4.2.1	Solvent mixture without alkyl chains . . . . .	40
4.2.2	Characterization of the Solvent Mixtures . . . . .	41
4.2.3	Exchange Dynamics . . . . .	47
4.2.4	Dynamics of Acridine orange . . . . .	49
<b>4.3</b>	<b>Thermodynamics of retention process in RPLC . . .</b>	<b>51</b>
4.3.1	Computational methods . . . . .	52
4.3.2	Results . . . . .	52
<b>4.4</b>	<b>Water at bare hydroxylated silica surface . . . . .</b>	<b>57</b>
<b>4.5</b>	<b>Computational part . . . . .</b>	<b>59</b>
4.5.1	Description of the system . . . . .	59
4.5.2	Molecular dynamics simulations . . . . .	61
4.5.3	Exchange dynamics . . . . .	62
4.5.4	Infrared Spectra . . . . .	62
<b>4.6</b>	<b>Results and discussion . . . . .</b>	<b>63</b>
4.6.1	Static properties . . . . .	63
4.6.2	Orientational behavior of water . . . . .	64
4.6.3	Planar density distribution . . . . .	66
4.6.4	Dynamical properties . . . . .	66
4.6.5	Vibrational spectroscopy . . . . .	71

---

This chapter starts with brief introduction about experimental background and practical relevance of solid silica interface. The importance of silica lies in its versatility to be used in many industrial, environmental and biological processes, such as waste water filtration,<sup>141</sup> antireflection coatings,<sup>142</sup> antibacterial coatings,<sup>143</sup> catalytic materials,<sup>144</sup> drug delivery<sup>145</sup> and chromatography.<sup>146–148</sup> Many studies on the adsorption of nanoparticles could be controlled by manipulating the particle and the silica surface properties.<sup>149–151</sup> The process of adsorption is one of the key feature of liquid chromatography.

Part I of this chapter deals with water dynamics and its importance as a co-solvent at C<sub>17</sub>-phenyl grafted silica surface together with the process of intercalation of a probe molecule. Later on, intercalation of other organic compounds will be addressed quantitatively from thermodynamic perspective for which the experimental data are known. Part II of this chapter describes the interfacial behavior of water at the hydroxylated silica surface, which includes structure, dynamics and vibrational spectroscopic data compared to bulk water behavior. The behavior of water molecules at the solid-liquid interface which plays an important role in surface science (adsorption/desorption), geology, material science, diffusion of ions in nano-pores, biological membranes and in interfacial chemistry.<sup>6,152–155</sup> Part I and Part II of this chapter borrows largely from previously published work, *J. Phys. Chem. B*, 2012, 116, 10951 and *Faraday Discuss.*, 2013, 167, 329.

## 4.1

## Water at chromatographic interfaces

---

Chromatography (RPLC) is one of the major analytical techniques used for the separation of chemical compounds. On the other hand, there are many factors that can go wrong with the separation; this control is probably trickier in HPLC than in any other chromatography. In the past two decades, great theoretical understanding has been developed for liquid chromatography. However predicting the retention time and elution order for a given mixture is still a tricky task. Recent work done by Pizzi and De Sousa,<sup>156</sup> Noinville et. al.,<sup>157</sup> Siepmann and Schure<sup>35,158–161</sup> and Meuwly et. al.<sup>32–34,162</sup> has provided firm understanding for the behavior of stationary phase, role of solvent (water/methanol/acetonitrile) and the intercalation mechanism. Despite the seemingly “simple” chemical composition of such systems (functionalized silica surface, solvent mixture, and analyte molecules), the atomistic understanding

underlying the separation process remains elusive. One of the reasons for this is that the systems of interest are intrinsically disordered which makes controlled and atomistically resolved experiments difficult. Under such circumstances, computational methods are an ideal means to obtain additional insights and have considerably contributed to better characterize such systems.<sup>31,34,163,164</sup> Typically, a chromatographic system contains an alkyl-chain derivatized stationary phase, a solvent mixture, and analyte molecules. The nature and composition of the mobile phase, together with the functionalization of the stationary phase, play a decisive role in the separation process. Commonly used solvent mixtures include water (H<sub>2</sub>O) and an organic cosolvent such as acetonitrile (ACN) or methanol (MeOH). The composition of the solvent is adjusted to change the hydrophobic nature of the solution mixture and affects the elution time for the analyte. Experimentally, spectroscopic methods including IR,<sup>165–167</sup> Raman, and NMR<sup>168</sup> investigations have provided detailed information about water/methanol mixtures. The general consensus is that such solutions separate into MeOH-rich regions and water-rich regions and lead to microheterogeneous or microimmiscible<sup>169–171</sup> solutions at microscopic levels which was also observed experimentally by Raman spectroscopy for water/acetonitrile mixtures.<sup>172</sup> In chromatographic systems the derivatization of the stationary phase is another important determinant.<sup>173</sup> The alkyl chains are nonpolar whereas the surface to which they are attached is polar. Most recently, the solvent distributed C<sub>18</sub> stationary phases was characterized for different ACN/water and MeOH/water mixtures from configurational-bias Monte Carlo simulations.<sup>174</sup> However these simulations are good to obtain thermodynamic properties but to follow the intermolecular dynamics, molecular dynamics are preferred scheme.<sup>34,162</sup>

---

**4.1.1**Theoretical and computational methods

---

A model silica support was constructed by slicing two 8.75 Å thick segments of the (101) face of quartz crystalline lattice with dimensions of 36 x 41 Å. This resulted in two -OH terminated surfaces with a vicinal silanol density of 3.1 μmol/m<sup>2</sup>. A chromatography column was then created by covalently tethering alkylsilane ligands (with alkyl chains in an all trans conformation) to the silanol oxygen atoms of the quartz surface and orthogonal to the bulk quartz. Alkyl chains were evenly distributed over the surface silanols in a

randomized fashion to result in a specific surface coverage of 0.88 and 2.65  $\mu\text{mol}/\text{m}^2$ . A 80 Å thick solvent box (water/methanol) was added between the two silica surfaces, resulting in a unit cell with dimensions of 36 x 41 x 97 Å. The simulation system is shown in Figure 4.1.

In the present work, the transferable intermolecular potential three-point (TIP3P)<sup>175</sup> water model was used. For the methanol (MeOH) molecule, methyl hydrogen atoms were assigned to aliphatic hydrogen (atom type HA), the methyl-C atom is an aliphatic  $\text{sp}^3$  carbon (CT3), the hydroxyl oxygen is a polar oxygen (OH1), and the hydroxy hydrogen atom was assigned to a polar hydrogen (H). The OH equilibrium bond length is 0.96 Å. The MeOH is flexible with standard CHARMM parameters used for the CT3-OH1 bond, the HA-CT3-OH1 and HA-OH1-CT3 angles, and the dihedrals. As for water, SHAKE<sup>176</sup> was used to constrain all hydrogen atoms. Five different functionalizations of the chromatographic column are considered and studied here with two different solvent compositions. The functionalizations include  $-\text{CH}_3$ ,  $-\text{CN}$ ,  $-\text{NH}_2$ ,  $-\text{NO}_2$  and  $-\text{C}_6\text{H}_5$ , and their parametrization has been reported in earlier work.<sup>162</sup> Briefly, for  $-\text{CN}$ ,  $-\text{NH}_2$ , and  $-\text{C}_6\text{H}_5$  existing CHARMM parameters were employed in analogy to lysine and phenylalanine. For  $-\text{NO}_2$  literature values were used.<sup>177</sup> Details concerning the number of molecules (water and methanol) and the solvent composition are reported in Table 4.1.

**Table 4.1:** Number of water/methanol molecules for different simulations and solvent mixtures, 80/20 and 50/50 volume fraction, respectively. Low and High correspond to the surface coverage 0.88 and 2.65  $\mu\text{mol}/\text{m}^2$

Systems	Surface coverage	
	Low	High
C18.20.80	2985/343	2518/280
C18.50.50	1710/640	1456/524
C17cn.20.80	3072/336	2466/292
C17cn.50.50	1731/632	1609/576
C18nh2.20.80	3042/271	2804/244
C18nh2.50.50	1814/692	1609/571
C18no2.20.80	2891/272	2777/255
C18no2.50.50	1783/625	1642/598
C17phenyl.20.80	2975/275	2273/220
C17phenyl.50.50	1783/690	1572/544

The force field parameters for the Si-O and O-C bonds ( $V = \frac{1}{2}k(r-r_e)^2$ ) were ( $k = 525.0$  kcal/mol,  $r_e = 1.62$  Å) and ( $k = 428.0$  kcal/mol,  $r_e = 1.42$  Å),

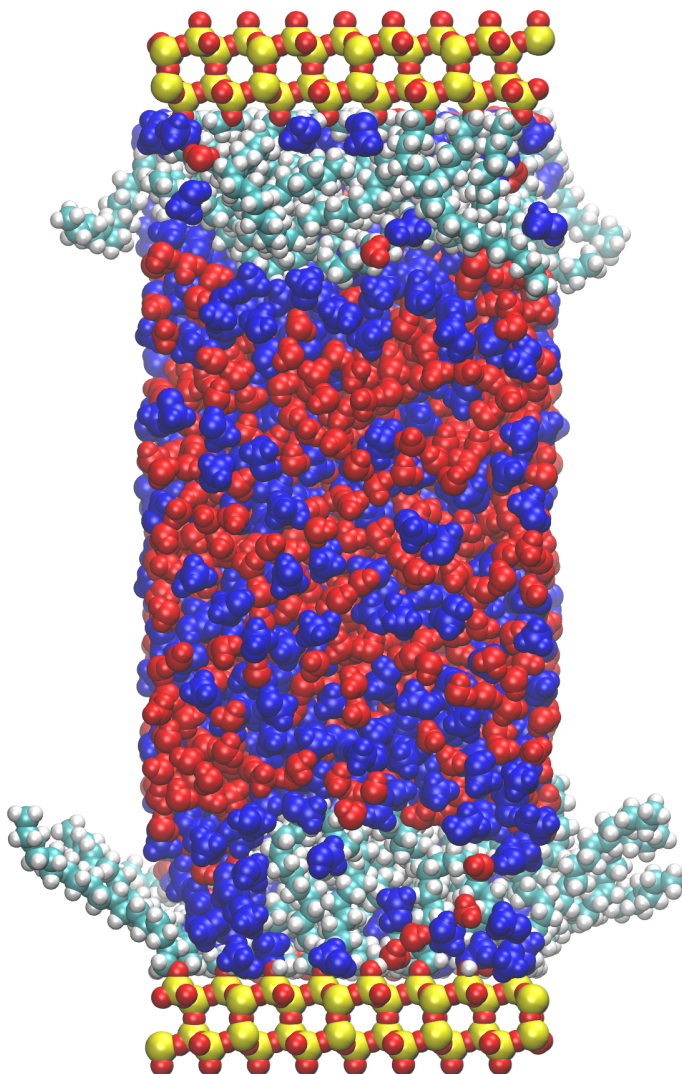


**Figure 4.1:** Schematic representation of the chromatographic system along with the molecule. The figure shows the silica layer (silica in yellow, oxygen in red),  $C_{18}$  - chains (green) grafted onto it, water (red), methanol (blue). The snapshot is taken during the simulation of acridine orange in  $C_{18}$  - functionalized system with 50/50 W/MeOH solvent concentration. All atoms are shown in vdW representation.



respectively; for the Si-O-C, O-Si-O, and O-C-C angles ( $V = \frac{1}{2}k(\theta - \theta_e)^2$ ) were ( $k = 40.0$  kcal/mol,  $\theta_e = 120.0^\circ$ ), ( $k = 40.0$  kcal/mol,  $\theta_e = 90.0^\circ$ ), ( $k = 40.0$  kcal/mol,  $\theta_e = 110.0^\circ$ ), respectively; and for the Si-O-C-C and O-C-C-C dihedral angles ( $V = k(1 + \cos[n\chi - \eta])$ ) they were ( $k = 0.15$  kcal/mol,  $n = 1$ ,  $\eta = 0.0^\circ$ ). The -OH groups bonded to the Si layer had point charges of +0.66e and -0.66e for hydrogen and oxygen atoms, respectively. For acridine orange, the force field parameters are taken from our previous work.<sup>162</sup>

#### 4.1.2 Molecular Dynamics simulations

For all molecular dynamics (MD) simulations the same protocol was used. After solvation, the systems were subjected to 500 steps of steepest descent minimization followed by 200 steps with the Adopted Basis Newton-Raphson algorithm to relieve strain. Next, MD simulations were carried out at constant volume and constant temperature (NVT) using the CHARMM<sup>178</sup> program. The time step in all simulations was 1 fs, and SHAKE<sup>176</sup> was used to constrain the bonds to hydrogen atoms. All simulations were carried out with periodic boundary conditions. Nonbonded interactions were truncated at a distance of 10 Å on an atom-by-atom basis, using a shift function for the electrostatic interactions and a switch algorithm for the van der Waals interactions. The atomic positions of the bulk quartz surface with the exception of the exposed hydrogen atoms of the silanol groups were held fixed during the simulation (1664 atoms). Initially, the systems were heated and equilibrated for 50 ps, followed by 2 ns of production simulations. Atomic coordinates from the MD simulations were recorded at 50 fs intervals for analysis. For every system with different functionalizations one simulation was carried out, except for C<sub>18</sub> alkyl chains, for which five independent simulations were run.

Apart from the above setup, the dynamics of acridine orange in a (-C<sub>6</sub>H<sub>5</sub>) derivatized alkyl column was investigated. An analyte molecule (acridine orange) was introduced into an equilibrated C<sub>17</sub>-phenyl column. Water molecules overlapping with the analyte molecule were removed, and then production simulations were continued for 5 ns to study the dynamics of the analyte. These simulations were run in the C<sub>17</sub>-phenyl system with high surface coverage (2.65 μ/m<sup>2</sup>) in solvent mixtures W/MeOH (100/0, 80/20 and 50/50) for both protonated (NH<sup>+</sup>) and unprotonated (N) acridine.

### 4.1.3 Analysis of the Trajectories

---

Observables to characterize the chromatographic systems were determined from ensemble averages. They include the alkylsilane chain length, solvent density, acridine position with respect to the silica surface, and the diffusion coefficient of the analyte (acridine orange), which is calculated from the Einstein relation.

$$D = \frac{\langle |\vec{\mathbf{r}}_i(t) - \vec{\mathbf{r}}_i(0)|^2 \rangle}{6t} \quad (4.1)$$

where  $\vec{\mathbf{r}}_i(t)$  is the position of the center of mass of a single molecule. Previous experimental<sup>179</sup> and simulation studies<sup>33</sup> suggested that a typical chromatographic system with a C<sub>18</sub> stationary phase can be largely partitioned into three different types of water molecules. In order to analyze the water dynamics, the system is partitioned into three regions: Region I, defined as water molecules within 2.8 Å of Si-bonded oxygen atoms, referred to as “bonded water molecules”; region II, defined as water molecules within 18 Å of the silica layer, called “stationary” and region III, defined as water molecules between 20 to 60 Å away from the surface are called “bulk” water. Depending upon the initial position, water molecules are either in regions I, II or III. The number of water molecules that left a specific region during the production phase and entered a neighboring region is used to follow equilibration of the systems.

Another useful observable is the width of the stationary phase  $\langle z \rangle$ , which is referred to as the “phase thickness”. It is defined as the average vertical distance of the terminal carbon atom of the alkyl chains farthest away from the silica support.

## 4.2 Results

---

### 4.2.1 Solvent mixture without alkyl chains

---

First, the behavior of the solvent mixture is studied for the unfunctionalized systems but with the silica support which defines  $z = 0$  and  $z = 80$  Å. The density of the solvent along the  $z$ -axis (along the height of the column)

is shown in Figure 4.2 for W/MeOH mixtures of 80/20 and 50/50 volume fraction, respectively. The density  $\rho$  of the solvent,

$$\rho = \frac{n_s}{n_s^{id}} \quad (4.2)$$

is calculated from the number of solvent molecules, (water or MeOH) in a slab of  $1\text{\AA}$  width relative to the number of solvent molecules in the same slab for an ideal, homogeneous mixture. The density of the solvent molecules in Figure 4.2 is averaged over the last 100 ps from 1900 to 2000 ps. For both mixtures away from the surface a local high density of one component is balanced by a low density of the other component. This is typical of microheterogeneity at a microscopic level in which self-association of the same type of molecule is found<sup>162,174</sup> with continuous microheterogeneity proposed by Reimers and Hall.<sup>172</sup>

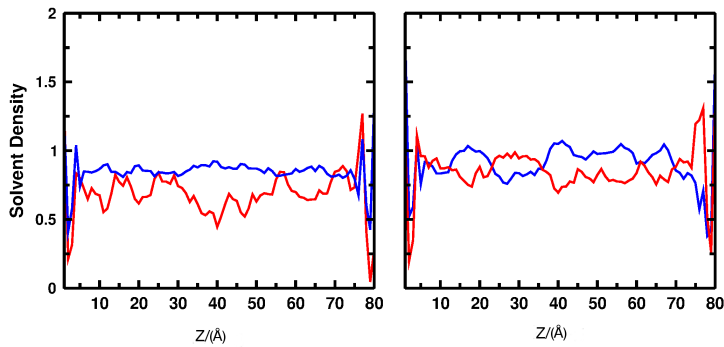


**Figure 4.2:** Solvent density profile for 80/20 (left) and 50/50 (right) volume fraction of solvent mixture without the presence of any functionalized chain on the silica layer.

The variation of the density profiles across the column depends on the relative concentrations of the solvent mixture. This agrees qualitatively with neutron diffraction experiments which found that methanol and water form percolating networks in which water molecule form clusters of typical sizes ranging from 2 to 20 (see also Figure 1).<sup>180,181</sup> Similar effects were recently observed in wide- and small-angle neutron scattering experiments on sorbitol-water mixtures.<sup>182</sup>

### 4.2.2 Characterization of the Solvent Mixtures

Depending on solvent composition, surface density and functionalization of the alkyl chains different organization of the solvent in and close to the surface

of the stationary phase can be expected. With both solvent compositions (80/20 and 50/50), both surface coverages (2.65 and 0.88  $\mu\text{mol}/\text{m}^2$ ) and all functionalizations the solvent density deviates from a uniform distribution  $\rho = 1$ . Rather, both water and MeOH densities decrease when approaching the stationary phase from the middle of the column ( $z = 40 \text{ \AA}$ ). This is shown in Figure 4.3 and 4.4. Between the stationary phases, which differ in their width depending on the system (see Table 4.2) microheterogeneity is still observed. Furthermore, common to all preparations of the systems is a more or less pronounced MeOH density about 5  $\text{\AA}$  away from the surface and a preserved water density at the surface. In other words, the silica (Si-OH) surface is “wet” and hydrated. This agrees with previous work for acetonitrile/water and pure water solvent.<sup>33,162,174</sup>

Comparing high- and low-coverage surfaces Figure 4.3 and it is observed that the width over which the water distributes is approximately 5  $\text{\AA}$  wider for low alkyl chain coverage. This, together with the analysis in Table 4.2, suggests that the alkyl chains are in a more collapsed state for low surface coverage. With high surface coverage, the alkyl chains are forced into a more parallel conformation which leads to increased conformational stability and a more upright and brush-like arrangement.

**Table 4.2:** Functionalized alkyl chain phase thickness  $\langle z \rangle$  measured in  $\text{\AA}$ , defined as the average height of the functionalized alkyl chains with respect to the silica layer. Data is compared with previous work done with acetonitrile as a co-solvent. These data are calculated from 2ns of MD simulation. Low and high refer to the surface coverage.

$\langle z \rangle$	Methanol		Acetonitrile		$N_{\text{water}}$
System	Low	High	Low	High	High
C18.20.80	8.9	13.1	8.0	13.2	35(1)
C18.50.50	10.7	14.8	12.1	15.2	30(1)
C17cn.20.80	10.2	15.3	9.2	13.5	36(1)
C17cn.50.50	11.1	16.8	11.6	16.5	32(1)
C18nh2.20.80	8.2	16.6	9.8	11.8	30(1)
C18nh2.50.50	12.7	13.5	12.8	15.2	25(1)
C18no2.20.80	8.6	14.5	10.0	14.1	37(1)
C18no2.50.50	10.6	15.9	11.1	16.1	33(1)
C17phenyl.20.80	9.2	15.3	9.3	15.4	34(1)
C17phenyl.50.50	10.6	16.6	16.7	14.3	32(1)

Increased MeOH concentrations (50/50 compared to 80/20) change  $\rho_{\text{MeOH}}$  in the middle of the column. In general, fluctuations in  $\rho_{\text{MeOH}}$  are more pronounced for 80/20 compared to 50/50 solvent composition. This is due to

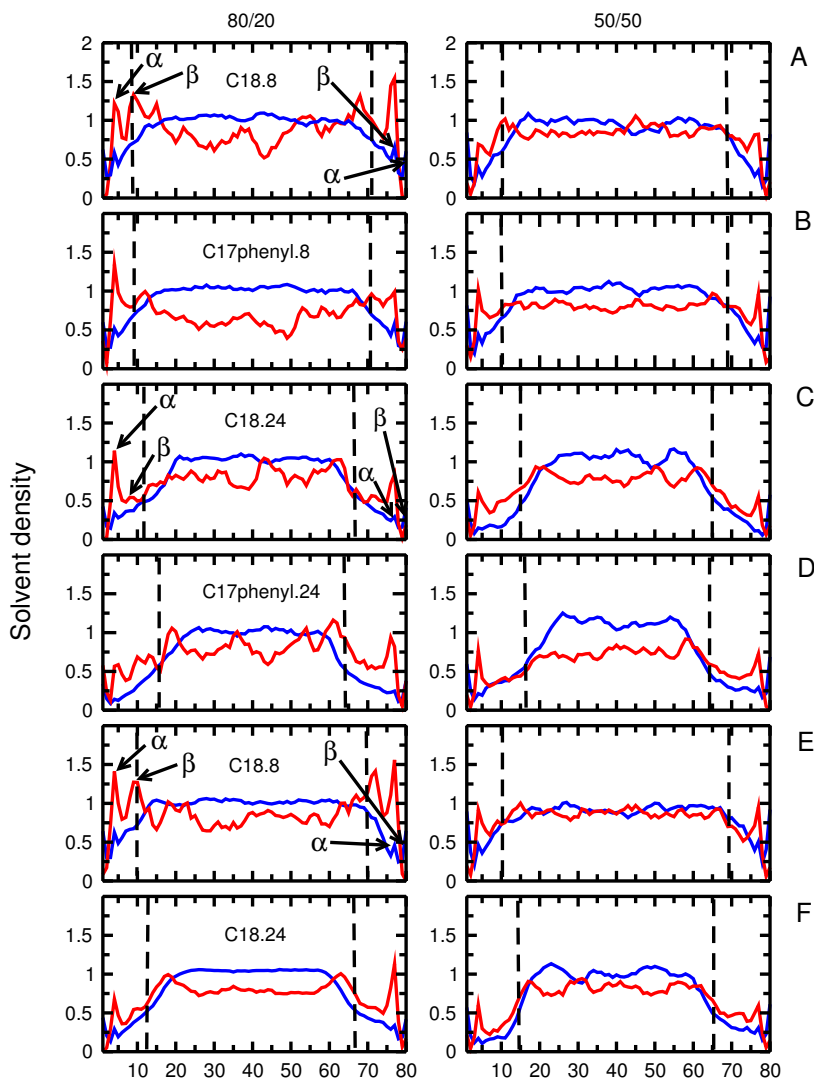


**Figure 4.3:** Average solvent density profile (over 100 ps from 1900 to 2000 ps of simulation time) with C<sub>18</sub> and C<sub>17</sub>-phenyl chains and 80/20 W/MeOH solvent composition (left) and 50/50 W/MeOH composition (right). (A: unfunctionalized C<sub>18</sub> low coverage; B: C<sub>17</sub>-phenyl low coverage; C: C<sub>18</sub> high coverage; D: C<sub>17</sub>-phenyl high coverage; E: C<sub>18</sub> low coverage average over 4 independent simulations; F: C<sub>18</sub> high coverage average over 4 independent simulations. Blue traces correspond to water density, and red traces correspond to MeOH density. The y-axis gives the density of the solvent as defined in eq 2.

increased MeOH concentration in the solvent (Figure 4.3 A, B and 4.3 C, D). The density maxima in  $\rho_{\text{MeOH}}$  within  $\approx 5 \text{ \AA}$  of the surface are more pronounced for low methanol concentration and for both low and high surface coverage and are indicated by  $\alpha$  and  $\beta$  labels in Figure 4.3. These peaks are due to MeOH close to the surface forming a transient layered structure. For a 50/50 solvent composition these peaks are not sharp because as the MeOH concentration increases, it is more homogeneously distributed in the solvent mixture which leads to a decrease in the microheterogeneous structure compared to 80/20 solvent composition. This also shows that microheterogeneity is concentration-dependent and continuous. Comparison of the different functionalization shows that the widths of the stationary phases can vary by 10-25% (see Table 2), depending on the terminal group attached to the chain and the solvent composition.

In order to determine how representative individual trajectories are to characterize the different systems, four independent simulations were run for high- and low-surface coverage  $\text{C}_{18}$  with W/MeOH mixtures of 80/20 and 50/50, respectively. Figures 4.3 E, F report average density distributions from four independent simulations. The density distribution is similar to what is found from individual trajectories (see Figures 4.3A, C), which suggests that the current simulations cover most of the important parts of phase space.

In all systems studied, an appreciable amount of water is found at the surface which corresponds to H-bonded water molecules (Figures 4.3). However, the precise amount also depends on solvent concentration and surface coverage (see Table 2). As the MeOH volume fraction in the mixture increases, the number of water molecules close to the surface reduces. With increasing surface coverage of the stationary phase the hydrophobic interaction increases. This is another reason for the decrease in the water density at the surface. Table 4.2 shows that for given surface coverage the number of water molecules for most functionalizations increases by  $\approx 15\%$ , whereas it is only 6% for  $\text{C}_{17}$ -phenyl chains.

In order to better understand the double  $\rho_{\text{MeOH}}$  peak  $\alpha$  and  $\beta$  within  $10 \text{ \AA}$  of the silica surface, as observed for most systems studied (Figure 4.3), the orientation of the methanol-OH bond vector relative to the z-axis was considered depending on the distance from the silica layer. Here, the OH bond vector points from the hydrogen atoms toward the oxygen of MeOH. The probability distribution  $P(\cos\theta)$ , where  $\theta$  is the angle between the OH vector and the space-fixed z-axis, for the orientation of the MeOH molecule is shown in Figure 4.4. This analysis

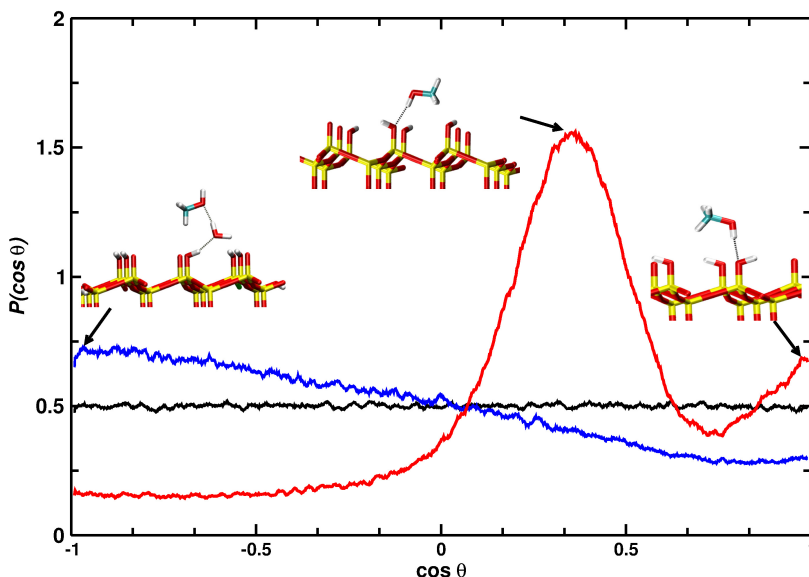


**Figure 4.4:** Average probability distribution for the MeOH -OH bond vector in different layers along the column, averaged over 1 ns. The orientation of the -OH bond vector within 5 Å of silica oxygen in red, in a layer from 5 to 10 Å (blue) and in the middle of the column (black). Structural representations for features in the probability distribution functions are also provided. The color scheme is carbon (blue), oxygen (red), silicon (yellow), and hydrogen (white).

is done for three layers, each 5 Å wide. The first layer includes MeOH molecules within 5 Å of the silica-oxygen atom and the second layer those between 5 and 10 Å. The third layer contains methanol from the middle of the column between 35 and 40 Å. Figure 4.4 demonstrates that the -OH bond vector in the first layer has two preferred orientations (red line), while in the second layer (blue line) the -OH bond vector predominantly orients in an antiparallel fashion relative to the first-layer water molecules. The probability distribution for the -OH bond vector in the middle of the column is uniform as would be expected (black line).

Figures 4.5 A, B show the time evolution of the phase thickness for C<sub>18</sub> and C<sub>17</sub>-phenyl derivatized alkyl chains and suggests that phase thickness depends upon the density of alkyl chains grafted on the silica surface and solvent composition. Table 2 establishes that for low surface coverage all functionalized chains collapse a behavior already observed in previous simulations.<sup>34</sup> At very low grafting density, the chain behaves much like an isolated chain in solution, since they have more spatial freedom; however, at high grafting density the polymer enters the “brush” regime,

a theoretical observation made by Alexander<sup>183</sup> and de Gennes.<sup>184</sup> Because the chains are more densely packed and due to increased hydrophobic interactions among themselves, they have less freedom to move (rotate or bend).

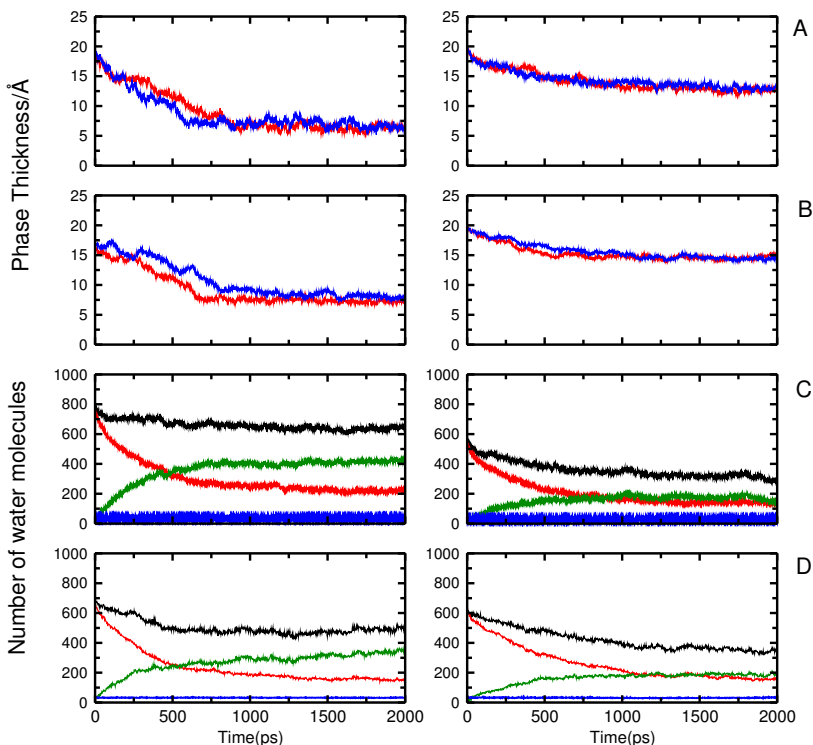


**Figure 4.5:** Temporal development of the phase thickness for unfunctionalized  $C_{18}$  (A) and  $C_{17}$ -phenyl (B) with W/MeOH compositions of 80/20 (red) and 50/50 (blue). Left column is for low surface coverage ( $0.88 \mu\text{mol}/\text{m}^2$ ) and right column for high surface coverage ( $2.65 \mu\text{mol}/\text{m}^2$ ). The solvent exchange dynamics in high surface coverage ( $2.65 \mu\text{mol}/\text{m}^2$ )  $C_{18}$  is reported in panels C and D. The left column is for 80/20 W/MeOH solvent mixture and the right column for 50/50 W/MeOH solvent mixture. Red traces represent outflow of water molecules from the stationary phase to the bulk phase; green, inflow of water molecules from the bulk to the stationary phase; black, total number of water molecules in the stationary phase (sum of red and green traces); blue, the occupation of the hydroxyl groups on the silica layers.

Another factor that influences the spatial extent of the chains is the increased amount of methanol in the mixture which was also observed with acetonitrile as a solvent (see Table 4.2 for comparison). We also observed that chains with polar terminal groups ( $-\text{CN}$ ,  $-\text{NO}_2$ ,  $-\text{NH}_2$ ; Table 4.2) are more extended compare to nonpolar functionalized ( $-C_{18}$ ,  $-C_6H_5$ ) end group. Polar termini provide a favorable environment for water or methanol molecules to interact,



which may contribute to their more extended conformation. In comparing water/ACN and water/MeOH mixtures with the same organic volume fraction, more pronounced solvent penetration for ACN is found compared to MeOH which is consistent with previous work. There is enrichment of the organic cosolvent in the interfacial region, and this effect is more pronounced for 80/20 compared to 50/50 solvent mixture and is more than the bulk density, as found from Monte Carlo simulations. Similar behavior is found for the other derivatized surface C<sub>17</sub>-CN, C<sub>18</sub>-NH<sub>2</sub>, C<sub>18</sub>-NO<sub>2</sub>.

### 4.2.3 Exchange Dynamics

For analyzing the water exchange dynamics between regions II and III, the water flux between these regions was determined. During the MD simulations the number of water molecules exchanged is reported in Figures 4.5 C,D (for C<sub>18</sub> and C<sub>17</sub>-phenyl and high surface coverage). The analysis shows that water molecules initially in region II exchange with region III and vice versa. It is also found that systems with different W/MeOH ratios exhibit significantly different numbers of water in the stationary phase. The numbers of water molecules in region I directly interacting with the silica, i.e., are H-bonded to the Si-OH groups, are summarized in Table 4.2. The number of water molecules in region I found here is similar to what was observed previously for acetonitrile as a solvent 38 and previous work with MeOH as a solvent. The data in Table 4.2 show that as the volume fraction of organic modifier increases, the number of water molecules in H- bonding contact with the silica surface decreases. This is due to the presence of MeOH which competes for H-bonding to the surface -OH group. Depending on the systems, the numbers of water molecules that are exchanged between the regions are different. Figure 4.5C (left) reports results for a C<sub>18</sub> column with a 80/20 solvent mixture. The red trace follows the number of waters exchanged ( $\approx 250$ ) between regions II and III, compared to the initial state at  $t = 0$ . After less than 1 ns a steady state is reached. At the same time, the number of water molecules entering from region III to II is  $\approx 450$  (green), whereas the black trace reports the total number of water molecules always residing in region II, which is  $\approx 700$  during the entire simulation. For C<sub>18</sub> and 50/50 solvent mixtures (Figure 4.5C (right)) the amount of water pumped in and out between regions II and III is  $\approx 200$ , similar to a 80/20 mixture, whereas the number of water molecules that exchange with region III is larger for 80/20 than that for a 50/50 solvent

mixture. A similar behavior is observed for other functionalized chains as well (not shown here). Typically, reaching an equilibrium in the exchange dynamics is slower for 50/50 mixtures compared to 80/20. Quantitatively, all 80/20 systems are equilibrated in less than 1 ns, whereas it can take up to 1.5 ns for 50/50 mixtures. This is probably due to the increased number of water-MeOH hydrogen bonds in 50/50 compared to 80/20 mixtures.

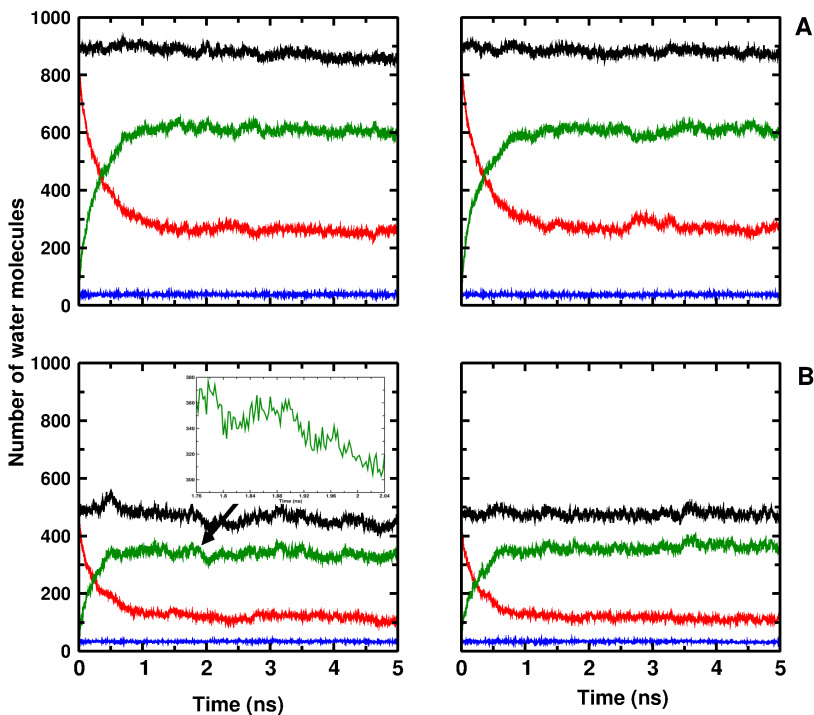


**Figure 4.6:** Inflow and outflow of water molecules from between the alkyl chains measured after introducing acridine orange into  $C_{17}$ -phenyl systems with high surface coverage and W/MeOH compositions of 100/0 (A) and 80/20 (B). Left column for protonated acridine ( $NH^+$ ) and right column for the neutral state (N). The red trace represents outflow of water molecules from the stationary phase to the bulk; green, inflow of water molecules from the bulk to the stationary phase; black, total number of water molecules in the stationary phase (sum of red and green trace); blue, occupation of the hydroxyl groups on the silica layers.

#### 4.2.4 Dynamics of Acridine orange

In order to better characterize the consequences of different solvent composition and surface densities, the dynamics of an analyte molecule was followed. Acridine orange has been previously used to characterize interfacial dynamics at the stationary phase/solvent layer. It was found that it can interact with the surface via chemisorption or intercalation within these functionalized chains. For investigating the dynamics of acridine orange at the C<sub>17</sub>-phenyl/solvent interface, acridine orange was introduced in the system 3 Å above the C<sub>17</sub>-phenyl layer in different W/MeOH compositions (100/0, 80/20, 50/50). The exchange dynamics of water following the perturbation of the system is reported in Figure 4.6. With increasing MeOH concentration the number of exchanged water molecules decreases, and the time for equilibrating water exchange increases from  $\approx 200$  to 500 ps as shown in Figures 4.6A, B. With regards to solvent flow, all systems are well equilibrated on the 5 ns time scale. Occasionally, “avalanches” of solvent can be observed in which there is a sudden change in the number of water molecules; see inset Figure 4.6B, where the number of water molecules changes from 350 to 300 in region II (green line) in less than 1 ns.

To characterize the motion of acridine orange relative to the surface, the  $z$ -coordinate of the acridine orange center-of-mass (COM) is reported as a function of time. Figure 4.7 suggests that the analyte molecule readily adsorbs to the C<sub>17</sub>-phenyl interface, and due to the exchange of solvent and motion of the alkyl chains it moves in and out of the silica surface. Figures 4.7A, B also suggest that there is no appreciable change in the average phase thickness (black curve) of the C<sub>17</sub>-phenyl interface for all solvent compositions during 5 ns of MD simulation. For 100/0 W/MeOH solvent composition the analyte molecule is completely intercalated and remains there for the rest of the simulation. For other solvent mixtures (Figure 4.7B) the analyte molecule moves in and out of the stationary phase. For the simulation in C<sub>17</sub>-phenyl with 100/0 solvent composition, the dynamics of acridine orange (NH<sup>+</sup>) is shown in Figure 4.7C (I-IV). The snapshots are taken at different times along an MD simulation. These snapshots suggest that once the cavity at the surface is formed, the analyte molecule easily moves toward the surface and resides there for the rest of the simulation. The formation of a cavity is not directly observed in our simulations but results from the tendency of the alkyl chains to reduce the surface area by alkyl chain clustering, which in turn is

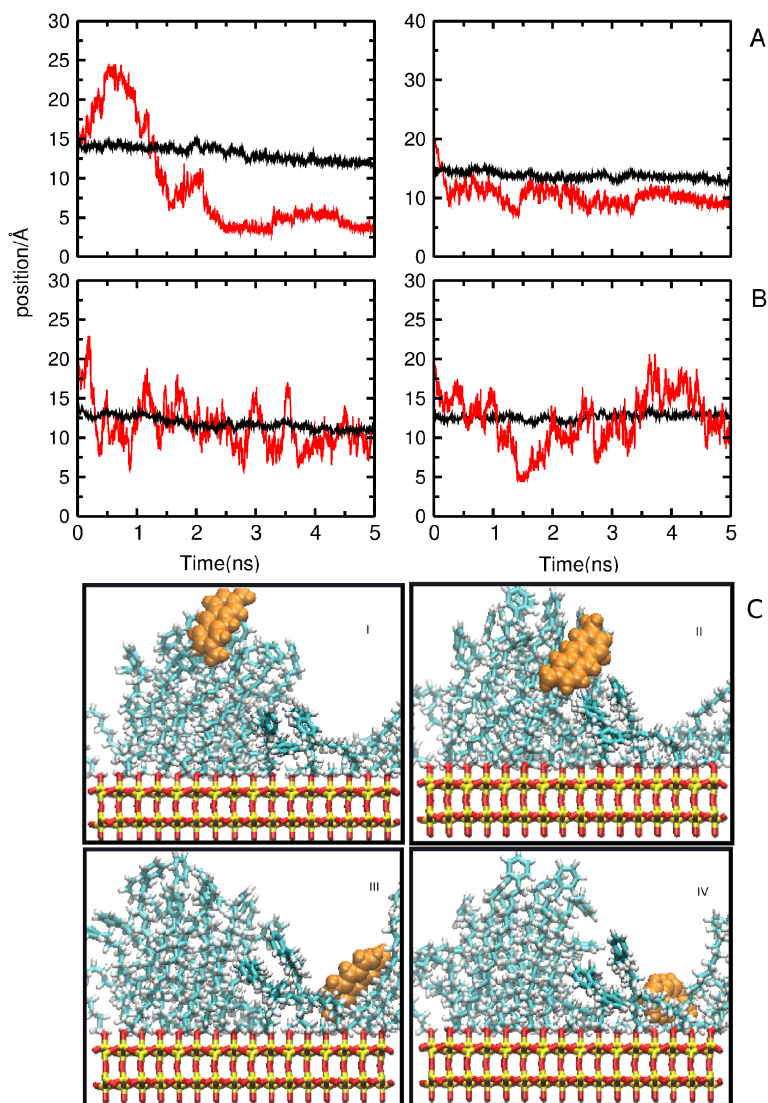


**Figure 4.7:** Inflow and outflow of water molecules from between the alkyl chains measured after introducing acridine orange into  $C_{17}$ -phenyl systems with high surface coverage and W/MeOH compositions of 100/0 (A) and 80/20 (B). Left column for protonated acridine ( $NH^+$ ) and right column for the neutral state (N). The red trace represents outflow of water molecules from the stationary phase to the bulk; green, inflow of water molecules from the bulk to the stationary phase; black, total number of water molecules in the stationary phase (sum of red and green trace); blue, occupation of the hydroxyl groups on the silica layers.

enthalpy-driven as confirmed experimentally. Clustering will lead to space on the silica surface which allows the analyte molecule to approach the surface and to intercalate. Cavity formation and intercalation of analyte molecules is an element of the slot model and has been a matter of debate for the past few years.

The dynamics of acridine orange can also be characterized in terms of a diffusion coefficient  $D$  (see eq 1). For high coverage  $C_{17}$ -phenyl the diffusion coefficient  $D$  of acridine orange increases with increasing MeOH concentration from 0.013 to 0.042 ( $10^{-4}$  cm<sup>2</sup>/s) in going from W/MeOH mixtures of 100/0 to 80/20 and reaches 0.054 ( $10^{-4}$  cm<sup>2</sup>/s) in 50/50 W/MeOH for unprotonated acridine. For protonated acridine the diffusion coefficients depend less strongly on the solvent composition. They range from 0.058 to 0.076 ( $10^{-4}$  cm<sup>2</sup>/s) for solvent compositions of 100/0 to 50/50, respectively. As the analyte molecule moves toward the interface, its diffusion slows down. This can be quantified by considering acridine orange in 100/0 W/MeOH at different  $z$ -positions above the surface. For positions 20, 10, and 2 Å above the surface,  $D = 0.064$ , 0.024, and  $0.014 \times 10^{-4}$  cm<sup>2</sup>/s are found. Experimentally, the lateral diffusion coefficient in pure water was found to be 0.042 ( $10^{-4}$  cm<sup>2</sup>/s) which considerably slows down to 0.0013 ( $10^{-4}$  cm<sup>2</sup>/s) in  $C_{18}$  columns. While the diffusion coefficient in pure water and the slowdown in the presence of a stationary phase are correctly captured, the effect of the interface is only a factor of  $\approx 4$  in the simulations, compared with at least an order of magnitude experimentally.

### 4.3 Thermodynamics of retention process in RPLC

Much of above discussion is mainly based on the structural and dynamical behavior of the solvent and the analyte molecule. The process of intercalation of analyte molecule was based on the diffusion of analyte into the stationary phase. Another route of investigation for the retention process is to understand the thermodynamic of analyte transfer from bulk to the stationary phase. There are experimentally known partition coefficients which can be used to estimate the free energy change for complete retention process. There are only limited theoretical studies,<sup>185–188</sup> which quantify the retention process by calculating the accurate free energy for transferring the molecule from the bulk to the stationary phase. Most of these used Monte-Carlo method for

studying gas-liquid chromatography. Following work will evaluate the free energy differences for two analyte compounds (Chloro benzene and Phenol) for transferring from bulk solvent phase to the stationary phase. The solvent phase is taken as 20.80 and 50.50 MeOH/Water mixture and the C<sub>18</sub> chains acts as the stationary phase. These value matches the known experimental data.

---

### 4.3.1 Computational methods

---

The simulation protocol followed here is exactly same as mentioned above for the other chromatographic systems. This study is mainly done with MeOH/Water solvent mixture having composition of 20.80 and 50.50 by volume, and with C<sub>18</sub> alkyl chain with the grafting density of 2.65  $\mu\text{mol}/\text{m}^2$ . The other difference is that the probe molecule is re-parametrized, which also includes higher order multipoles (quadrupole) description compare to point charges. The parametrization is based on thermodynamic data, such as density  $\rho$  of the pure liquid, heat of vaporization ( $\Delta H_{vap}$ ) and hydration free energy ( $\Delta G_{hyd}$ ) at 298 K. Umbrella sampling was performed to estimate the free energy differences for these compounds. 35 umbrella windows were made, each having the width of 1 Å. In each window the sampling was performed for 2 ns, which make the total sampling time of 70 ns. The reaction coordinate for this sampling process was the  $z$  component of the distance between the center of mass of the compound and the silica surface.

---

### 4.3.2 Results

---

The parametrization procedure is done for the analyte for which there are known experimental data for the retention time, density, heat of vaporization and free energy of hydration. The thermodynamic data evaluated from our simulations are given below in Table 4.3 and compared with the experimental values. For phenol, parametrization is still in progress. The results can be compared in 2 different ways, 1)- by calculating the change in free energy of the same compound in solvent of different composition or 2)- by comparing the difference in free energy of two different compound in same solvent. The

Compounds	density	$\Delta H_{vap}$	$\Delta G_{hyd}$
Benzene	0.89 (0.87)	7.95 (7.95)	-0.76 (-0.86)
Chloro benzene	1.12 (1.11)	9.87 (9.79)	-1.11 (-1.12)

**Table 4.3:** Thermodynamic data calculated from our simulations and compared with the experimental values given in parenthesis. The density is reported in  $\text{g/cm}^3$  and the heat of vaporization and the free energy of hydration is reported in kcal/mol.

result shown below follow both the methods. The free energy estimation was done by the formula

$$\Delta G = -RT \ln K \quad (4.3)$$

Using the above equation above the calculated value of change in free energy is shown below.

For Cl-benzene in two different solvent composition (20.80 and 50.50) the change in free energy is observed and reported below in the units of kcal/mol. This value is based on experimentally observed capacity factor.

$$\Delta G_{cl-benz} = -RT \ln \left( \frac{K_{50.50}}{K_{20.80}} \right) = -1.987 \times 300 \times \ln \left( \frac{55}{14} \right) = -0.815 \quad (4.4)$$

This experimental value can be qualitatively compared with change in free energy data reported in Figure 4.8 (top) for Cl-benzene between the  $z$  range of 5 and 15 Å.

Similar calculation for phenol is reported below.

$$\Delta G_{phenol} = -RT \ln \left( \frac{K_{50.50}}{K_{20.80}} \right) = -1.987 \times 300 \times \ln \left( \frac{5}{2} \right) = -0.546 \quad (4.5)$$

This experimental value can be qualitatively compared with change in free energy data reported in Figure 4.8 (bottom) for phenol between the  $z$  range of 5 and 15 Å. The two observed data shows that these two compounds are more stable in 20.80 solvent composition compared to 50.50 solvent composition, which agrees with our calculated value (Figure 4.8). One can compare value of two different compound for same solvent composition, which is reported below.

(1) - For 20.80 solvent composition

$$\Delta G = -RT \ln \left( \frac{K_{cl-benz}}{K_{phenol}} \right) = -1.987 \times 300 \times \ln \left( \frac{55}{4} \right) = -1.429 \quad (4.6)$$

(2) - For 50.50 solvent composition

$$\Delta G = -RT \ln \left( \frac{K_{cl-benz}}{K_{phenol}} \right) = -1.987 \times 300 \times \ln \left( \frac{14}{2} \right) = -1.159 \quad (4.7)$$

From these two values reported in equation 4.6 and 4.7 shows that Cl-benzene is more stable in stationary phase compare to phenol in both 20.80 and 50.50 solvent composition, which qualitatively agrees with our calculation from simulations (Figure 4.9). All the numbers reported above are in kcal/mol. These reported free energy profile conclude two important results, Cl-benzene is more stable in the stationary phase compare to phenol and this stability is independent of solvent composition which agrees qualitatively with experimental findings.



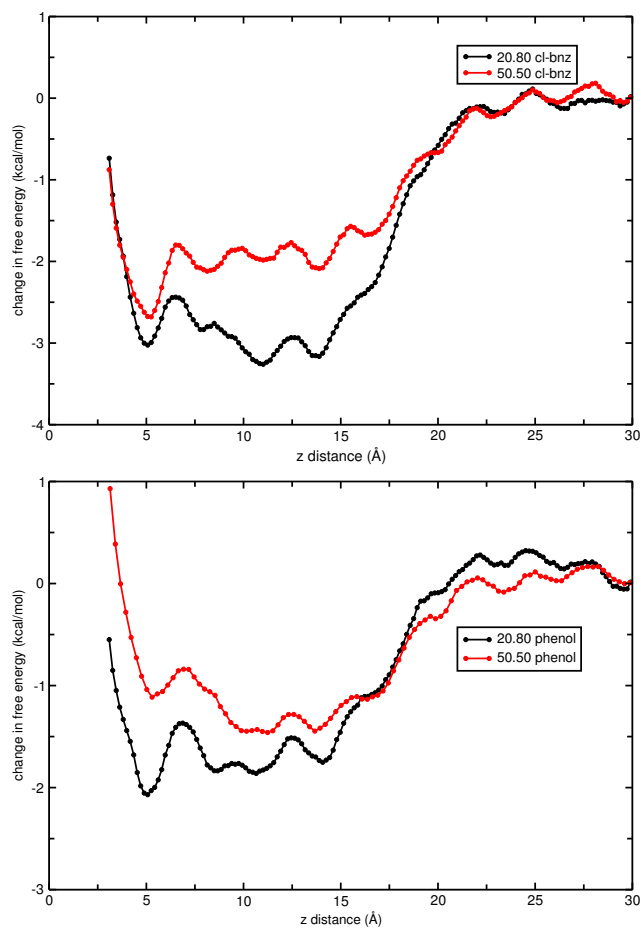


**Figure 4.8:** Comparison of free energy difference for Cl-benzene and phenol in 20.80 and 50.50 MeOH/W solvent composition.

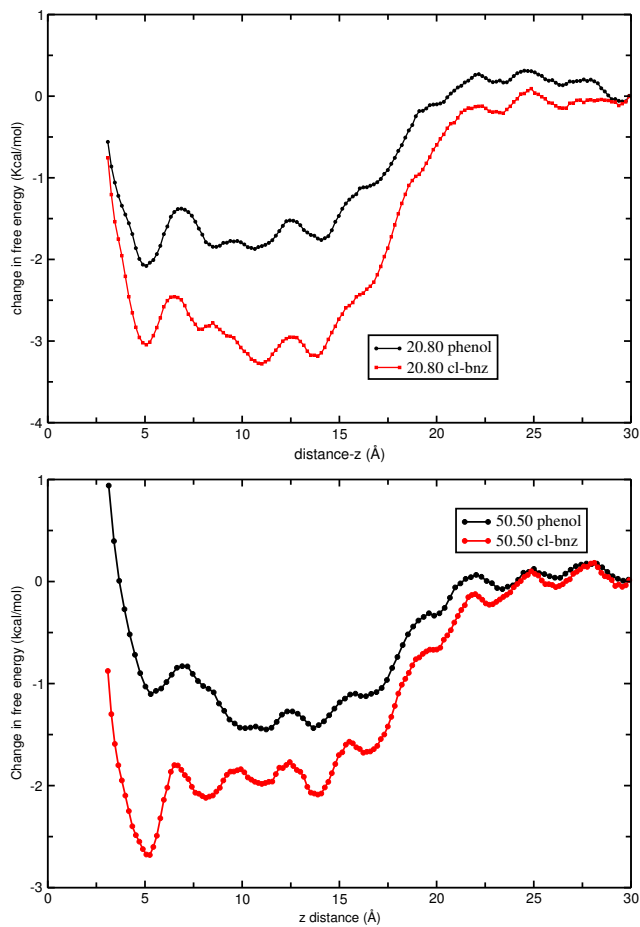


**Figure 4.9:** Comparison of free energy difference between phenol and Cl-benzene in 20.80 and 50.50 MeOH/W solvent composition.

## 4.4 Water at bare hydroxylated silica surface

Water molecules at the solid-liquid interface play important roles in surface science (adsorption/desorption), geology, material science, diffusion of ions in nanopores, biological membranes and in interfacial chemistry.<sup>6, 152–155</sup> A number of experimental and theoretical studies have provided deeper insight into the molecular level behavior of water itself and at interfaces. It has been found that properties of water at surfaces can be strongly affected by the existence and the nature of the solid substrate and is due to the heterogeneous environment generated by the surface itself. The resulting effects on water are observed through changes in the spectroscopic response, pronounced density layers, the change in the local dielectric constant and in different structural and dynamical properties of water at these interfaces. Such phenomena are also important technologically in the context of electrolytes near a charged surface and in chromatographic processes. As to the latter, various theoretical studies involving classical molecular dynamics, ab initio molecular dynamics and experimental techniques like non-linear optical spectroscopy have been used to characterize silica-water interfaces. Computer simulations considered interfacial water at quartz, metal and other mineral surfaces. These investigations clearly show how the solid substrate perturbs the local structure and hydrogen bond dynamics of water up to 10–15 Å away from the surface.

Water has been investigated particularly well at the water-air interface. These studies found spectroscopic features that extend from around 3200 to 3700  $\text{cm}^{-1}$ . The analysis of the spectroscopic signatures in terms of their origin and the local orientation of the water molecules has led to a number of, sometimes conflicting, interpretations. Also, water at mineral surfaces has been investigated by spectroscopic means. For water at silica surfaces the pH-dependent VSFG spectra were recorded at a quartz(0001) surface. A prominent two-peak structure with spectroscopic signals around 3200  $\text{cm}^{-1}$  and 3400  $\text{cm}^{-1}$  was found at high pH (SiO<sup>-</sup>) whereas at low pH (SiOH) the double-peak was less prominent.

The hydrogen bond and orientational dynamics of water in contact with nanoscopic environments has also attracted considerable attention. Of

particular relevance are experimental and simulation studies of water in reverse micelles, which provide a well defined chemical environment to study water dynamics in contact with a surface. The reorientational dynamics were found to contain multiple time scales, extending from the sub-picosecond librational dynamics to several ten picoseconds involving the reorganization of the water-hydrogen-bonded network. Comparing experimental and simulation results it was found that the nonexponential decay of the orientational diffusion is comparable although they do not agree quantitatively. In the context of chromatography, the role of water molecules has been recognized for quite some time. The existence of more or less ordered water networks has been postulated or found in chromatographic columns. Already 30 years ago, Scott and co-workers have suggested that individual water molecules can bind to the -OH groups of a silica surface and form a thermodynamically stable (fractional) monolayer. These water molecules, thought to be present up to temperatures of several hundred Kelvin, can serve as H-bond donors to additional water molecules, which eventually form filaments between the stationary (silica surface) and the mobile (solvent mixture) phase. The existence, morphology, and stability of such water filaments has been recently investigated by using atomistic simulations. These studies also corroborated the notion of water layers with differing stability depending on their separation from the stationary phase in chromatographic systems. The existence of surface-bound water molecules in chromatographic systems has been also established from atomistic simulations using a range of force fields and simulation strategies.

In the present study, classical molecular dynamics simulations are used to provide insight into atomistic details of water at the silica-water interface relevant to chromatographic studies. We report on the structural and dynamical properties of the solvent including the effect of multipolar interactions in the electrostatics on vibrational properties of water and provide an atomistic interpretation of the observed data. To this end, two different water models are used in the simulations - the widely used TIP3P parametrization<sup>189</sup> and a flexible, multipolar water model. First, the computational realization of the system and the analysis of the data is described. Then, static and dynamical properties of water at a silica (101) face at low pH are reported and finally, the infrared spectroscopy is discussed.

## 4.5 Computational part

### 4.5.1 Description of the system

The model silica layer was constructed by slicing two 8.75 Å thick segments of the (101) face of a quartz crystalline lattice with dimensions of  $36 \times 41$  Å. This resulted in two surfaces with 64 silica hydroxy groups. The distance between the two silica layers was 30 Å which resulted in a unit cell with dimensions  $36 \times 41 \times 47.5$  Å<sup>3</sup>. A 30 Å wide water box was superimposed and all water molecules overlapping with the silica layers were removed. Figure 4.10 shows a schematic representation of the system which has also been used previously in the study of chromatographic interfaces.<sup>32–34, 162</sup>

In the present work, two water models were employed. One is the TIP3P water model<sup>189</sup> and the second one is a flexible model based on the parametrization by Kumagai, Kawamura and Yokokawa (KKY)<sup>190</sup> which was used with a quadrupolar charge model (see below). The functional form of the KKY potential for the stretching and bending energies is

$$\begin{aligned} E_{\text{str}} &= D\{1 - \exp[-\beta(r - r_0)]\}^2 \\ E_{\text{bend}} &= 2f_k k_1 k_2 \sin^2(\theta - \theta_0) \end{aligned} \quad (4.8)$$

where

$$k_i = 1/\{\exp[g_r(r_i - r_m)] + 1\}$$

in which the  $r_i$  are the equilibrium distance of the O-H bond of the water molecule and  $g_r$  and  $r_m$  are reported in Table 4.4. For the electrostatics, a monopolar (i.e. TIP3P) and a multipolar charge model with a geometry independent quadrupole on the oxygen atom and up to monopoles on the hydrogens was used nuria:2009. The electrostatic parameters for the multipolar model were obtained from ab initio calculations at the MP2/aug-cc-pVQZ level of theory and are described in Table 4.4. The Lennard-Jones (LJ) parameter for this flexible water model was the same as for the TIP3P water model.<sup>189</sup> The parameters for the silica surface were taken from our previous work.<sup>32, 34, 162</sup> With the original parametrization of the KKY potential<sup>190</sup> for water the

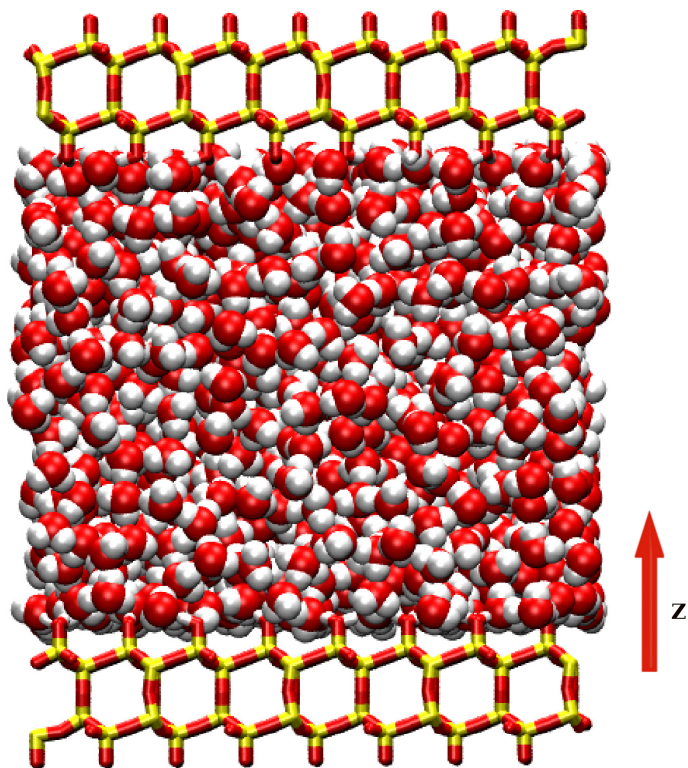


**Figure 4.10:** The solid silica layer with water. Water molecule are in CPK representation. Silica layer in licorice representation. Color code: oxygen atoms of water and silica layer are shown in red, silica atoms are shown in yellow and hydrogen atoms are shown in white. The  $z$ -axis is normal to silica surface.

**Table 4.4:** Parameters for water potential reported in the work of Kumagai et al. and used in this work, together with the harmonic frequencies computed from them. Atomic units are used for  $D$ ,  $\beta$ ,  $r_0$ ,  $f_k$ ,  $r_m$ ,  $g_r$ ,  $\theta_0$  is given in degrees. The literature data were converted to atomic units from the following parameters:  $D = 75.0$  kcal/mol,  $\beta = 2.74 \text{ \AA}^{-1}$ ,  $r_0 = \text{\AA}$ ,  $f_k = 1.1 \times 10^{-1}$  J,  $r_m = 1.40 \text{ \AA}$  and  $g_r = 7.0 \text{ \AA}^{-1}$ .

	$D(E_h)$	$\beta(\text{a}_0^{-1})$	$r_0(\text{a}_0)$	$f_k(E_h)$	$\theta_0(\text{deg})$	$r_m(\text{a}_0)$	$g_r(\text{a}_0^{-1})$
KKY	0.120	1.45	1.55	$2.5 \times 10^6$	99.5	2.65	3.7
this work	0.120	1.44	1.81	0.0388	99.5	2.65	3.7

stretching frequencies obtained were  $\nu_1 = 3720 \text{ cm}^{-1}$ ,  $\nu_2 = 1525 \times 10^4 \text{ cm}^{-1}$  and  $\nu_3 = 3763 \text{ cm}^{-1}$ , which does not yield correct frequencies for the water bending mode. In the present study a reparametrization was used which gives fundamentals at  $\nu_1 = 3689 \text{ cm}^{-1}$ ,  $\nu_2 = 1595 \text{ cm}^{-1}$  and  $\nu_3 = 3724 \text{ cm}^{-1}$ .<sup>191</sup>

**Table 4.5:** Multipole moments of H<sub>2</sub>O used in this work. MP2/aug-cc-pVQZ calculations were used for the parametrization. Each multipole component is static, i.e., it does not depend on the geometry of the molecule. In the multipole component  $Q_u^x$ ,  $u$  represents angular momentum labels (00, 10, 11c, 11s, 20, 21c, 21s, 22c, and 22s) and  $x$  represents the atom type (O or H). The units of  $Q_u^x$  are given in parentheses in the table. Only nonzero components are shown.

	$Q_{00}^O(\text{e})$	$Q_{10}^O(\text{ea}_0)$	$Q_{20}^O(\text{ea}_0^2)$	$Q_{22c}^O(\text{ea}_0^2)$	$Q_{00}^H(\text{e})$
H <sub>2</sub> O	-0.595922	-0.065831	-0.041591	-1.125991	0.297961

### 4.5.2 Molecular dynamics simulations

All MD simulations were carried out with the CHARMM program<sup>178</sup> with provisions for multipolar interactions.<sup>122</sup> The number of water molecules in the system was 1310. Simulations for H<sub>2</sub>O, HOD and D<sub>2</sub>O followed identical protocols as described below. All simulations were carried out with periodic boundary conditions (PBC) and nonbonded interactions (electrostatic and Lennard-Jones) were truncated at a distance of 12  $\text{\AA}$  and switched between 10 and 12  $\text{\AA}$ . The atomic position of the bulk quartz surfaces with the exception of the exposed hydrogen atoms of the silanol groups (1664 atoms) were held fixed during the simulations. Initially the system was heated and equilibrated

for 20 ps followed by 100 ps of production at 300 K in the *NVT* ensemble. The time step used was  $\Delta t = 0.4$  fs for all the simulations with the flexible KKY model. For these simulations, a Nose-Hoover thermostat with a thermal piston mass of  $Q = 50$  (kcal/mol) $\text{ps}^{-2}$  was used. For each of these systems with  $\text{H}_2\text{O}$ ,  $\text{D}_2\text{O}$  and HOD, multiple independent simulations each of 100 ps, were carried out and the results were averaged. For the TIP3P water model two simulations were run, one single trajectory of 5 ns length with  $\Delta t = 1$  fs using SHAKE and one trajectory for 100 ps with  $\Delta t = 0.4$  fs, to calculate the vibrational spectra of water. However for some specific analysis (exchange dynamics), simulations with the MTP water model are run for several nanoseconds. The MTP water model with inclusion of quadrupole is a computationally expensive water model and this is the reason for carrying out multiple short simulations (100 ps). It had been observed from other simulations performed on silica surfaces<sup>192, 193</sup> that the water dynamics (translational diffusion, orientational relaxation time) well converges within 10-30 ps. Furthermore, convergence tests for calculated IR spectra of single spectroscopic probes suggest that 500 ps simulations are appropriate for this property.<sup>194</sup>

### 4.5.3 Exchange dynamics

---

For the analysis of the water dynamics, the system was divided into layers of thickness 3 Å each, parallel to the Si-surface and commensurate with the typical size of a water molecule. The first layer (layer I) includes water molecules which are within 3 Å of the oxygen atoms of the silica layer, which serve as the reference  $z = 0$ . The second layer (layer II) extends from 3 to 6 Å, and the third layer (layer III) from 6 to 9 Å. The exchange of water molecules is quantified by considering water molecules which are in layer I at  $t = 0$  and move to layer II during the simulation and vice versa.

### 4.5.4 Infrared Spectra

---

The infrared (IR) spectrum is calculated from the Fourier transform of the dipole moment autocorrelation function  $C(t) = \langle \vec{\mu}(0)\vec{\mu}(t) \rangle$ , which is accumulated over  $2^n$  time origins, where  $n$  is an integer such that  $2^n$  corresponds to between 1/3 and 1/2 of the trajectory, with the time origins separated by 0.8 fs.  $C(\omega)$ , which



is the Fourier transform of  $C(t)$ , is computed using a fast Fourier transform (FFT) with a Blackman filter to reduce noise. The final infrared absorption spectrum  $A(\omega)$  is then calculated from

$$A(\omega) = \omega\{1 - \exp[-\hbar\omega/(k_B T)]\}\hat{C}(\omega) \quad (4.9)$$

where  $k_B$  is the Boltzmann constant and  $T$  is the absolute temperature in Kelvin.

## 4.6 Results and discussion

With a fully hydroxylated surface (SiOH), the simulations in the present work correspond to low-pH conditions in actual experiments. First, static properties are discussed after which the translational, rotational and exchange dynamics are considered and the infrared spectra are presented.

### 4.6.1 Static properties

**charge density profile** The charge density profile of water and deuterated water as a function of the distance away from the silica surface is shown in Figure 4.11, with the silanol oxygen atom defining  $z = 0$ . Figure 4.11 shows that the presence of the surface perturbs the interfacial water structure up to  $\approx 5 \text{ \AA}$  away from the silica surface. A similar behavior is observed for HOD and  $D_2O$ . The data in Figure 4.11 is consistent with an orientation of the interfacial water where the water-H atom points towards the surface. The positive charge excess at  $z = 0$  is due to the water oxygen H-bonded to the hydrogen of silanol group and the water-H atom pointing downwards between two adjacent silanol groups and was also found in previous studies.<sup>195–197</sup> The excess of negative charge at  $z = 4$  is due to the second layer of water molecules interacting through hydrogen bonding with the first layer, as shown in the inset. These charge density profiles are expected to affect the distribution of charged species at solid-water interfaces, possibly contributing to the adsorption of lactates<sup>198</sup> and amino acid<sup>199</sup> analogues on the hydrated silica surface.

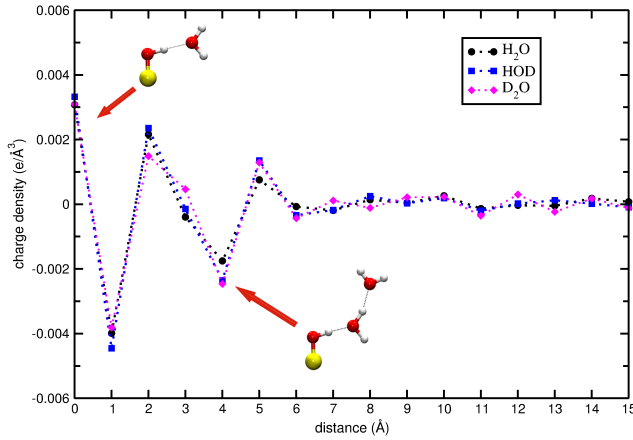


**Figure 4.11:** Charge density profile of water as a function of the vertical distance  $z$  from the silica layer. The  $z = 0$ , is considered as the oxygen atom of the silanol group. This data is plotted for  $\text{H}_2\text{O}$ ,  $\text{HOD}$ ,  $\text{D}_2\text{O}$  with the quadrupole moment on oxygen atoms. color code: black for  $\text{H}_2\text{O}$ , blue for  $\text{HOD}$ , magenta for  $\text{D}_2\text{O}$ .

#### 4.6.2 Orientational behavior of water

The presence of the surface is expected to perturb the local structure of water.<sup>200–202</sup> The orientation of water molecules near the surface can be quantified by considering the water-OH vector relative to the space fixed  $z$ -axis. For this, the scalar product  $\cos\alpha = \frac{\vec{r}_{\text{OH}} \cdot \vec{e}_z}{|\vec{r}_{\text{OH}}| |\vec{e}_z|}$  is computed for water in different layers. Figure 4.12 reports the orientational probability  $p(\alpha)$  for the OH-vectors involving both hydrogen atoms, H1 and H2, of the water molecules. For bulk water the water-OH vectors are expected to exhibit quite a uniform distribution as shown in Figure 4.12A, whereas water molecules near the surface should have clearly preferred orientations. This is indeed observed for the three orientations I to III in Figure 4.12B. For orientation I ( $\text{H}_w\text{-O}_w$  points towards the surface-O atom, i.e. "H<sub>w</sub>-down" configuration) the scalar product is  $\approx 0$  whereas for orientation II ( $\text{H}_w\text{-O}_w$  points towards the water above) it is  $-1.0 \leq \cos(\alpha) \leq -0.8$  or  $140^\circ \leq \theta \leq 180^\circ$ , see Figure 4.12B. For orientation III both water-H<sub>w</sub>-O<sub>w</sub> vectors form an equal angle with the SiOH-hydrogen atom and yield  $0.4 \leq \cos(\alpha) \leq 0.6$  as shown in Figure 4.12B. Comparing this result with the orientation of the water TIP3P model (see Figure 4.12C), we note that orientation III is considerably less populated when using a TIP3P water model. This can be understood in terms of a favourable and stabilizing multipole-charge interaction between the water molecules and

the surface-silanol hydrogen atoms compared to charge-charge interaction in the TIP3P water model. The increased population of state III should also affect other properties of the system, including the diffusional behaviour and the spectroscopy of surface-near water molecules.

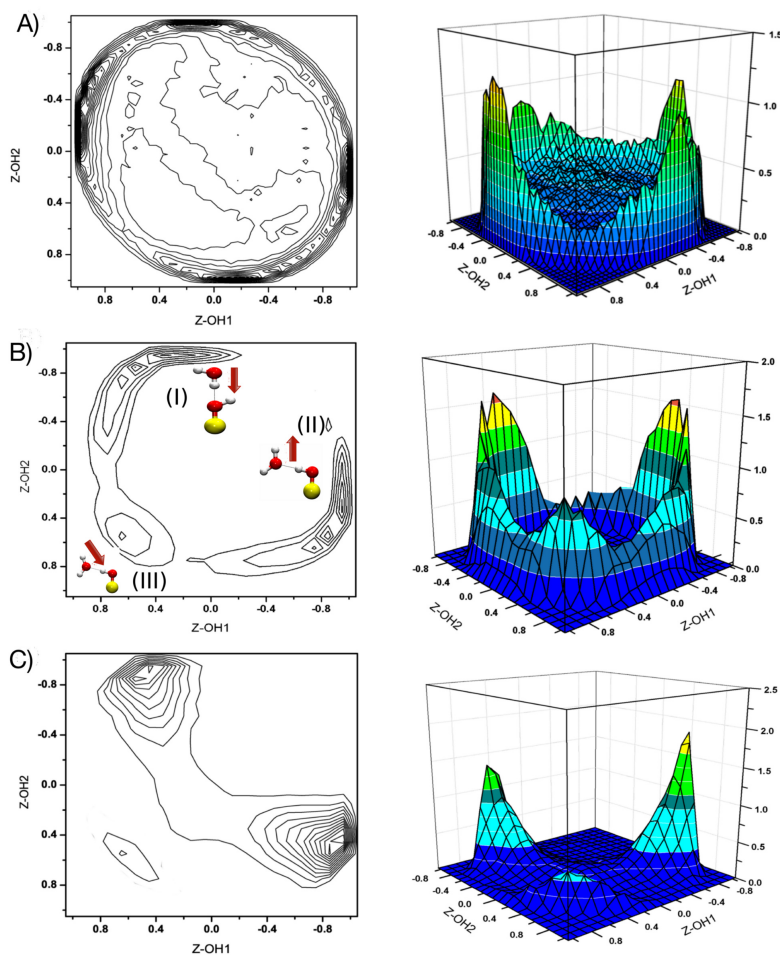


**Figure 4.12:** Contour plots (left) and normalized 3D probability distributions (right) for the orientation of water molecules in the system. A) Orientation of water molecules in the bulk with the MTP model. B) The three preferred orientations of MTP water molecules in the first hydration layer. State I corresponds to the OH-down configuration while state II corresponds to OH-up. In state III the water-OH vector is in a sideways orientation relative to the surface. C) Water orientation in the first hydration layer from simulations with the TIP3P water model.

### 4.6.3 Planar density distribution

The simulations allow to characterize the distribution and ordering of surface-bound water molecules. The planar density distribution of the first layer water molecules is shown in Figure 4.13. Due to the presence of the SiOH-groups, surface-bound water molecules can strongly interact with the surface which leads to pronounced density maxima between these attachment points. The distribution of water oxygen atoms was calculated separately in layers parallel to the surface ( $x-y$ -plane) and of thickness  $3 \text{ \AA}$  each. The silica oxygen atoms on the surface provide hydrogen bonding sites for interfacial water molecules and are shown as white dots in Figure 4.13A. We observe the formation of closed ring structures (yellow trace) of water molecules occupying the space around a single Si-OH group, see Figure 4.13A, which can be easily understood in terms of water molecules around -OH groups of the silica surface as shown in Figure 4.13B, (black dotted ring). Consequently, water molecules optimize their orientation relative to the surface SiOH groups. A similar analysis for simulations with the TIP3P water model is shown in the supporting information Figure S1 which displays a less ordered structuring for surface bound water. This corroborates the finding that including multipoles in intermolecular interaction affects the structuring of the interfacial layer.

### 4.6.4 Dynamical properties

**Translational Dynamics:** The translational dynamics of interfacial water molecules close to the surface perturbed by the presence of the SiOH groups can be further characterized in terms of their translational diffusion coefficients. The in-plane mean-square displacement  $\text{MSD}_{\parallel}$  for each layer is obtained from following the motion of the water-oxygen atoms according to

$$\begin{aligned}
 \langle D \rangle &= \lim_{t \rightarrow \infty} \frac{1}{4t} \langle \sum_{i \in \text{layer}} [(x_i(t) - x_i(t=0))^2 + (y_i(t) - y_i(t=0))^2] \rangle \\
 &= \lim_{t \rightarrow \infty} \frac{1}{4t} \langle \Delta r^2(t) \rangle
 \end{aligned} \tag{4.10}$$

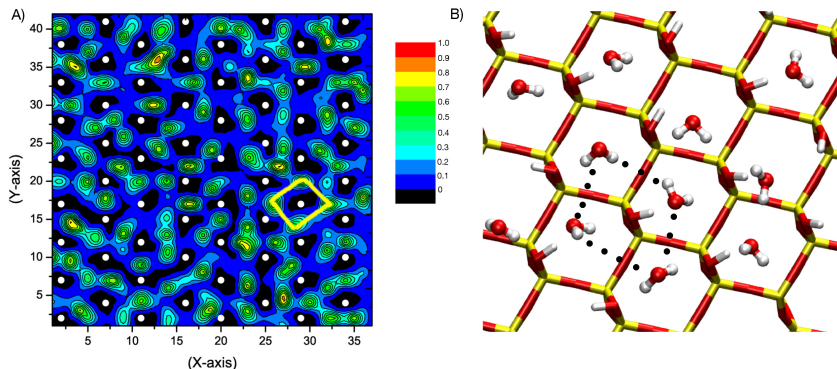


**Figure 4.13:** A) Surface water density distribution parallel to the surface ( $x - y$ -plane) for water molecules in the first hydration layer. The white dots in panel A correspond to the oxygen atoms of the silica surface. “0” and “1” correspond to the minimum and maximum occupation. Relative water occupations are color coded from black (0.0) to red (1.0). B) Top view for distribution of water molecules adsorbed on the silica layer due to hydrogen bonding with -OH group of silica layer. Water molecule is shown in CPK and hydroxylated silica surface in licorice representation.

from which the 2-dimensional self-diffusion coefficients  $D$  can be determined. This was done for the TIP3P, MTP and a modified MTP parametrization (see below) for the water molecules. As expected, the translational mobility of water molecules away from the interface is more rapid compared to layers close to the interface as shown in Figure 4.14. The in-plane diffusion coefficients  $D_{||}$  for different regions were determined by fitting the 4 to 20 ps portion of  $\langle \Delta r^2(t) \rangle$  to equation 4.10. With the MTP water model the in-plane diffusion coefficient for layer I ( $0.004 \text{ \AA}^2/\text{ps}$ ) is 35 times smaller than that in the middle of the column which is  $D_{||} = 0.14 \text{ \AA}^2/\text{ps}$ . This demonstrates that motion of water molecules adsorbed at the surface is slowed down due to strong electrostatic interactions with the surface. For the TIP3P model a similar observation is made although quantitatively, the numbers differ somewhat. They are  $0.007$  and  $0.21 \text{ \AA}^2/\text{ps}$ . For layer III the diffusion coefficients are  $0.06$  and  $0.08 \text{ \AA}^2/\text{ps}$ , respectively, for the MTP and TIP3P model.

In order to put these results into perspective, the (3-dimensional) diffusion coefficients for the MTP and TIP3P water models were also determined from 100 ps simulations of pure water (without silica surfaces) in a  $30 \times 30 \times 30 \text{ \AA}^3$  box with 1000 water molecules. They were found to be  $0.052 \text{ \AA}^2/\text{ps}$  and  $0.32 \text{ \AA}^2/\text{ps}$  for the MTP and TIP3P models, respectively, which compares with  $0.22$

$\text{\AA}^2/\text{ps}$  for the experimentally determined<sup>203</sup> diffusion coefficient. Hence, the quadrupolar model considerably underestimates the experimental value. This is related to the fact that the TIP3P van der Waals ranges were used in the simulations with the MTP electrostatic model. Repeating the MTP simulations with slightly increased (+2 %) van der Waals ranges on the oxygen atom yields diffusion coefficients in close agreement with the experimental value. Using these scaled van der Waals ranges for the MTP model in simulations of water in contact with the silica surface, the corresponding 2-dimensional diffusion coefficients for layer I ( $0.008 \text{ \AA}^2/\text{ps}$ ) which is 28 times smaller than that in the middle ( $0.28 \text{ \AA}^2/\text{ps}$ ). A similar behavior was already observed for water diffusion on hydroxylated aluminum<sup>204</sup> and other polar surfaces.<sup>201</sup>

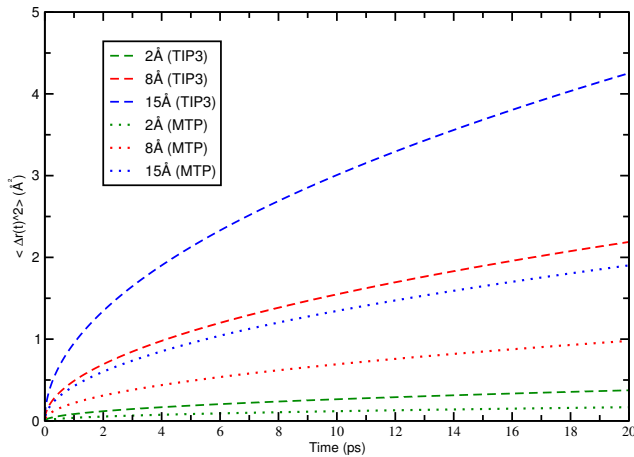


**Figure 4.14:** Mean square displacement for MTP and TIP3P water molecules in three different layers. The position of each layer is shown in the inset figure.

**Reorientational Relaxation:** The orientational behavior of water is highly dependent upon the surrounding environment and can result in slower dynamics close to the interface compared to bulk water. To characterize this we computed the reorientational autocorrelation functions for the water dipole moment vector ( $\vec{\mu}$ ) and the H-H vector ( $\vec{r}_{\text{HH}}$ ). The autocorrelation function used for this analysis is

$$C_{\hat{\rho}}(t) = \frac{\langle \hat{\rho}(0)\hat{\rho}(t) \rangle}{\langle \hat{\rho}(0)\hat{\rho}(0) \rangle} \quad (4.11)$$

where  $\hat{\rho}$  represents either the unit dipole moment vector  $\vec{\mu}$  or the H-H vector  $\vec{r}_{\text{HH}}$ ,

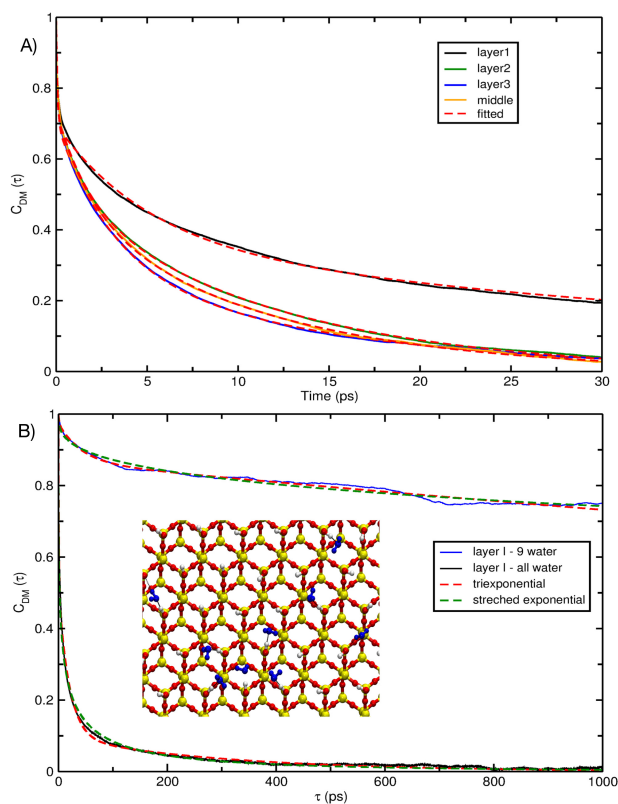
respectively. The data for H<sub>2</sub>O in different layers is reported in Figure 4.15A. The reorientational relaxation times can be obtained from  $C(\tau)$ . For water molecules in different layers we find that in the time regime from 0-30 ps the curves can be reasonably well described by triple exponentials  $A_1 \exp(-t/\tau_1) + A_2 \exp(-t/\tau_2) + (1 - A_1 - A_2) \exp(-t/\tau_3)$ , with decay constants  $\tau_1$ ,  $\tau_2$  and  $\tau_3$ . Furthermore, a stretched exponential  $\exp(-t/\tau)^\beta$  was considered to model the data and was found to equally well describe the data. The reorientational relaxation within the hydration layer (from  $z = 0$  to  $3 \text{ \AA}$ , layer I) is significantly slower than away from the surface (from  $z = 6$  to  $9 \text{ \AA}$ , layer III) and in the bulk (from  $z = 12$  to  $15 \text{ \AA}$ , middle). For all water molecules, irrespective of the layer they are in, the fastest decay occurs on a sub-picosecond time scale with  $\tau_1 = 0.5 - 0.8$  ps. The second decay constant ranges from 2-5 ps with faster time scales for water in the middle of the system (i.e. “bulk”) and longer time constants for water molecules in layer I. The third decay constant has values between 11 ps and 52 ps, for water molecules in the bulk and in layer I, respectively. When fitting  $C(\tau)$  with a stretched exponential,  $\beta$  assumes values between 0.38 and 0.53.

For the dynamics on the nanosecond time scale, water molecules adsorbed for the entire simulation were analyzed separately. There were 9 molecules, i.e. 10% of the total number of water molecules in layer I (see Figure 4.15B), which never exchange with neighboring layers. The corresponding rotational correlation function can be fit with time scales  $\tau_1 = 1.6$  ps,  $\tau_2 = 42$  ps and  $\tau_3 = 6.0$  ns. When all water molecules in layer I are analyzed together,  $\tau_1 = 0.6$  ps,  $\tau_2 = 19$  ps and  $\tau_3 = 307$  ps is obtained. Hence, the dynamics of the permanently adsorbed water molecules is distinctly different from that of the layer I molecules on average which also contains molecules that exchange with subsequent layers. It is also interesting to note that a stretched exponential fit yields  $\beta = 0.33$  for the 9 permanently adsorbed water molecules which is indicative of collective and frustrated behaviour as also found in glassy systems. This observation is consistent with rotational relaxations of water on silica or other surfaces, where molecules at the surface generally reorient more slowly than in the bulk.<sup>201,204,205</sup> Such long time decays have also been observed for water molecules at the surface of reverse micelles and hydrocarbons<sup>206,207</sup> and also measured by NMR experiments for water molecules at silica surfaces.<sup>205</sup> We further note that for  $\bar{\mu}$ , the relaxation in layer II (from  $z = 9$  to  $12 \text{ \AA}$ ) (Figure 4.15) is very similar to bulk water, demonstrating that at a distance of  $6 \text{ \AA}$  from the surface the rotational dynamics of water approaches that in the bulk. Another quantity, related to proton-NMR investigations, is the time

scale of the rotational dynamics of the H–H vector ( $\vec{r}_{\text{HH}}$ ). Fitting the  $\vec{r}_{\text{HH}}$  correlation function to a stretched exponential gives  $\beta = 0.34$  and  $\tau = 238$  ps for layer I water molecules and  $\beta = 0.49$  and  $\tau = 172$  ps for water molecules in the middle. This is consistent with the heterogeneous dynamics found from the dipole moment correlation functions.

**Exchange dynamics:** In chromatographic systems facile water exchange between neighbouring water layers within the alkyl chains was observed.<sup>32</sup> The water dynamics within the hydrophobic chains<sup>33</sup> can lead to formation of water filaments which allows intercalation of analyte molecules within hydrophobic regions.<sup>32</sup> It is therefore also of interest to consider the water exchange dynamics in the present system. As was mentioned in the previous section, on a time scale of 2.5 ns about 10 of the water molecules do not desorb from the surface. The absolute number of water molecules exchanged between the first and the second layer from the silica layer for the MTP water model, together with average number of water molecules in layer I and layer II are reported in Figure 4.16. Data from Figure 4.16 for individual layers suggest that layer I contains around 104 water molecules which is more than the number of silanol groups present at the surface. This is due to water molecules occupying interstitial sites between the silanol groups on the surface. Simulations with the MTP model find that the water flux equilibrates on the ns time scale and in equilibrium about 30 water molecules exchange between the two layers closest to the silica surface. However, it is interesting to note that even without the alkyl chains present, “avalanches” of water molecules can desorb or adsorb onto the silica surface, see e.g. the rapid change in the blue trace in Figure 4.16 around 1.5 ns, which also suggests collective behavior.

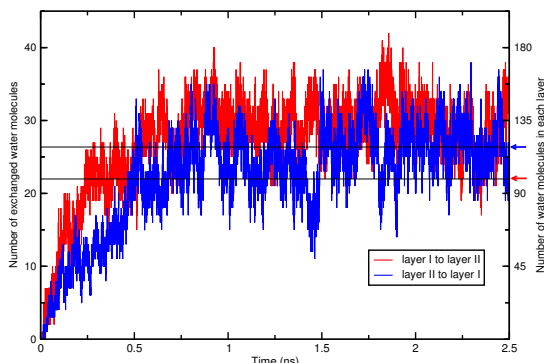




**Figure 4.15:** The dipole moment auto-correlation function for  $H_2O$  in different layers. A) Correlation function for  $\vec{\mu}$  for 4 different layers with the fitted data. Color code: layer I (black), layer II (green) and layer III (blue), middle (orange) and fitted data (red). Only the fit to layer I is shown. All other fits are of similar quality. The inset shows the correlation function on short times. B) Correlation function for the 9 water molecules which remain adsorbed to the surface for the entire 2.5 ns trajectory (blue) and for all water molecules in layer I (black).

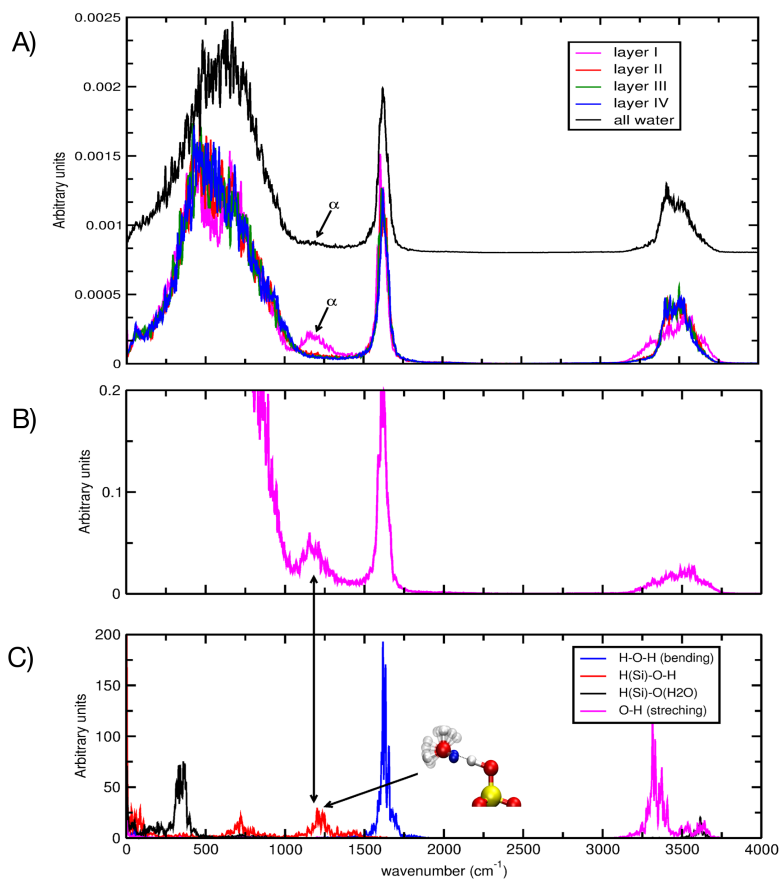
#### 4.6.5 Vibrational spectroscopy

Figure 4.17A gives an overview of the IR spectrum from simulations with the MTP model computed for all water molecules. Also the layer-specific spectra for layers I to IV are shown. By comparing the spectrum of layer I with those from layers II to IV it is evident that surface-bound water molecules give rise to considerably different spectroscopic signals. In particular the bonded -OH stretching region ( $3000$  to  $3750\text{ cm}^{-1}$ ) differs in its width and around



**Figure 4.16:** Exchange of water molecules between layers I and II. The red trace corresponds to water molecules which were initially in layer I and exchanged to layer II and the blue trace represents water molecules initially in layer II and exchanged to layer I. Each layer has a width of 3.0 Å. The two arrows on the right hand side correspond to the average number of water molecules in layers I and II which are 95 and 124, respectively.

$1150\text{ cm}^{-1}$  a new band, labeled  $\alpha$  in Figure 4.17A, arises which is absent for water molecules in layers II and beyond. Water molecules in layer I have a more heterogeneous environment compared to water molecules in layers II and beyond as they are surrounded by the silica layer and water molecules. Contrary to that, water molecules in layers away from the interface have a significantly more homogeneous environment. Experimentally, vibrational spectroscopy is a sensitive and powerful means to characterize structurally disordered condensed phase systems. In particular, surface sensitive SFG spectroscopy together with atomistic simulations<sup>60,201</sup> can provide detailed information about the relationship of structure and spectroscopy at interfaces. In order to better understand the spectroscopic features of water molecules in the first layer, power spectra for different coordinates involving water molecules were also determined. In Figure 4.17B, the water-IR spectrum for first layer molecules is enlarged. Figure 4.17C reports power spectra for coordinates including the water-HOH bend, the water-OH and the  $\text{O}_W\text{-H}_{\text{SiOH}}$  stretch, and the  $\text{HO}_W\text{-H}_{\text{SiOH}}$  bend modes. Comparison with the IR spectrum identifies the  $\text{HO}_W\text{-H}_{\text{SiOH}}$  bend to be responsible for the IR peak at  $\approx 1150\text{ cm}^{-1}$ . The SiOH-hydrogen atom and water-oxygen atom give rise to strong hydrogen bonding which leads to a libration mode as indicated in the inset Figure 4.17C. With the quadrupolar model for water, the tetrahedral geometry of the water molecules is captured more realistically. Simulations with the TIP3P water model without using SHAKE leads to a spectroscopic signal around  $1150\text{ cm}^{-1}$  but the power spectrum for the  $\text{HO}_W\text{-H}_{\text{SiOH}}$  bend is featureless and extends



**Figure 4.17:** A) Vibrational spectra of all water molecules (black) with the KKY plus quadrupolar water model together with layer-specific spectra for 4 different layers where each layer has a width of 3 Å. The arrow indicates the shoulder near the H(Si)-O(W)-H(W) bending mode. B) The enlarged IR spectra for water molecules in layer I. C) Power spectra corresponding to different modes as shown in the inset Figure. The black arrow shown in the figure make correspondence to mode which give rise to new peak in the spectra of water in the first hydration layer. A ball-and-stick model illustrating the H(Si)-O(W)-H(W) bending modes is drawn. Blue spheres indicate the oxygen lone pairs.

from a few hundred up to  $2000\text{ cm}^{-1}$  in stark contrast with simulations using the MTP model.

In order to study the isotope dependence, the same simulations were repeated for HOD and  $\text{D}_2\text{O}$  with the MTP model. The overall IR spectra are reported in Figure 4.18. The water-bending vibration shifts to the red as expected due to the larger mass in HOD and  $\text{D}_2\text{O}$  compared to  $\text{H}_2\text{O}$ . Concomitantly, the  $1150\text{ cm}^{-1}$  band shifts also to the red by  $-15\text{ cm}^{-1}$  and  $-35\text{ cm}^{-1}$  for HOD and  $\text{D}_2\text{O}$ , respectively. In the IR spectrum for  $\text{D}_2\text{O}$ , the  $\text{DO}_{\text{DOD}}\text{-H}_{\text{SiOH}}$  band is hidden under the DOD bending mode, confirmed by the power spectrum calculated for different modes of water ( $\text{D}_2\text{O}$ ) in layer I (not shown here). Experimentally,<sup>208</sup> this band appears at  $1209\text{ cm}^{-1}$  which compares with  $1180\text{ cm}^{-1}$  from the present simulations which emphasizes the quality of the MTP model together with the KKY parametrization for spectroscopic applications.

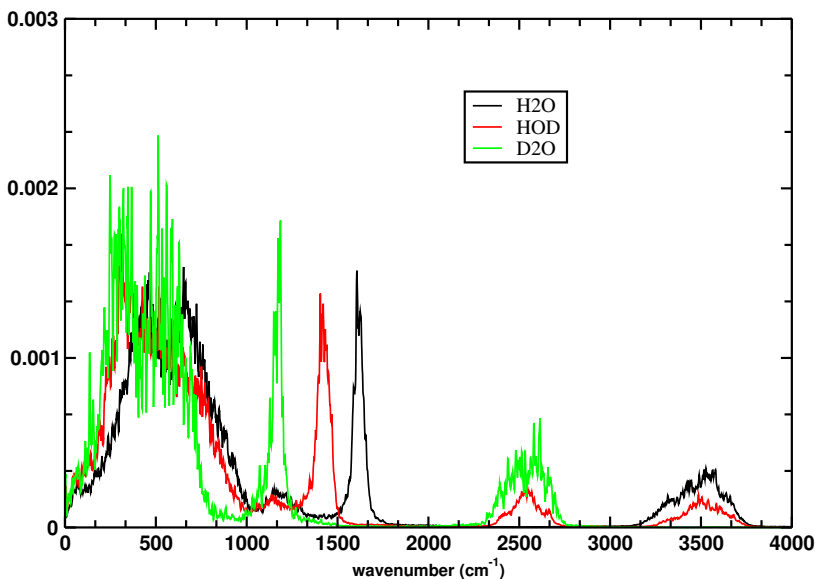


**Figure 4.18:** Vibrational spectra of  $\text{H}_2\text{O}$ , HOD and  $\text{D}_2\text{O}$  from simulations with the KKY model with multipolar electrostatics. The isotope effect on the vibrational spectra is evident. Specifically, the band at  $1150\text{ cm}^{-1}$  for  $\text{H}_2\text{O}$  shifts to the red upon isotopic substitution.

The orientation of water molecules with respect to the silanol group of the silica layer can be determined from angle distribution of the water-OH vector. The probability distribution is shown in Figures 4.19A and 4.19B. Figure 4.19A shows the distribution from simulations with the MTP model, whereas 4.19B reports that from using the TIP3P model. While the multipolar water model

yields a narrow distribution peaked around  $100^\circ$ , indicative of a tetrahedral environment of the surface-bound water molecules, the distribution for the TIP3P model is very broad and bimodal. A similar bimodal distribution is observed for TIP3P water molecules in contact with nanoporous silica layers in which the study was focused on the orientation of water depending upon the adsorbed amount of water<sup>196</sup> in the silica pore. This is due to the increased orientational freedom of water molecules described by simple point charge models - such as TIP3P - compared to parametrizations which account for higher electrostatic moments.

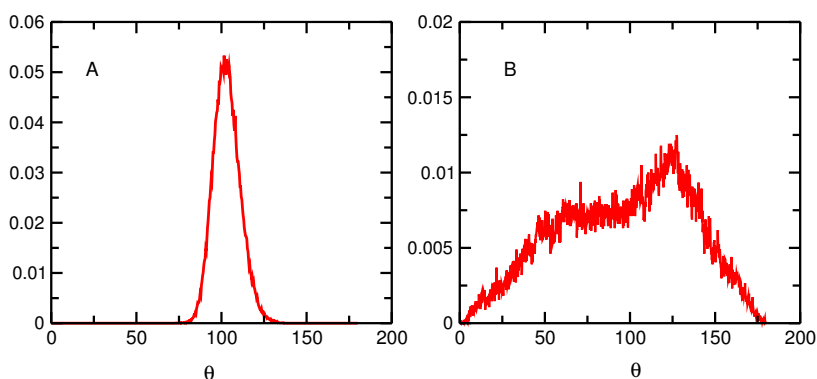


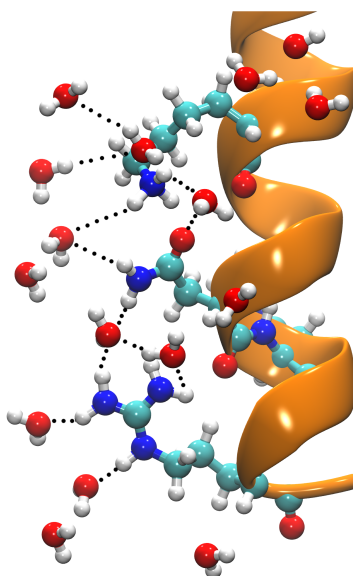
**Figure 4.19:** Distribution for the H(SiOH)-OH(water) angle with the KKY model and multipoles (panel A) and the TIP3P water model (panel B).



# 5

## WATER DYNAMICS AT PROTEIN INTERFACE

---



*It has been recognized that hydrogen bonds restrain protein molecules to their native configurations, and I believe that as the methods of structural chemistry are further applied to physiological problems it will be found that the significance of the hydrogen bond for physiology is greater than that of any other single structural feature.*

**Linus Pauling**

## Contents

---

<b>5.1</b>	<b>Introduction</b> . . . . .	<b>79</b>
5.1.1	Differences in the structures of oxy and deoxy state . .	80
<b>5.2</b>	<b>Theoretical methods</b> . . . . .	<b>82</b>
<b>5.3</b>	<b>Results</b> . . . . .	<b>85</b>
5.3.1	Role of Leu36 and Trp135 residue in CO migration . .	85
5.3.2	Presence of water in distal pocket . . . . .	93
5.3.3	Structural changes at the dimeric interface . . . . .	93
5.3.4	Free energy simulations . . . . .	103
<b>5.4</b>	<b>Conclusion</b> . . . . .	<b>104</b>
<b>5.5</b>	<b>Quaternary structural transition in HbA</b> . . . . .	<b>107</b>
<b>5.6</b>	<b>Computational methods</b> . . . . .	<b>107</b>
<b>5.7</b>	<b>Results</b> . . . . .	<b>108</b>
<b>5.8</b>	<b>Addition of chloride ions at <math>\beta_1\beta_2</math> interface</b> . . . . .	<b>121</b>
5.8.1	Reducing the force constant (k) between Fe and N . .	125
<b>5.9</b>	<b>2DN2 state in the presence of 2,3-DPG</b> . . . . .	<b>127</b>
<b>5.10</b>	<b>Outlook</b> . . . . .	<b>129</b>

---



This chapter mainly focuses on the dynamical behavior of two proteins. First of those protein is homodimeric *Scapharca inaequivalvis* hemoglobin from *mollusc*,<sup>209</sup> which shows cooperative behavior even in the crystal state.<sup>210</sup> The second protein is *human hemoglobin*, which is known as the paradigm of allosteric proteins, coined 50 years ago in a historical article by Monod and Jacob.<sup>211</sup> Part I of this chapter starts with a brief introduction of hemoglobin from *Scapharca inaequivalvis* followed by a motivation based on experimental findings, which encourage us to study the coupled dynamics of water at the dimeric interface of protein as well as ligand dynamics inside the protein. The rest of part I extensively discuss the results. Part II of this chapter starts with the motivation based on results obtained from MD simulations, which shows inconsistency with experimental findings. Rest of part II mainly deals with different approaches taken to study the quaternary structural transition (T  $\rightarrow$  R) in human hemoglobin in great details.

## 5.1 Introduction

Multimeric proteins offer the potential to study cooperativity and its relevance to controlling chemical and biological processes.<sup>211</sup> Specifically, it is of interest to understand the dynamics of and at the protein-protein interface<sup>212,213</sup> in view of the ligand dynamics<sup>214–217</sup> within each of the subunits of a particular di- or multimeric protein. The eventual coupling between two types of processes is potentially relevant for exercising control over ligand migration pathways<sup>216,218</sup> and the binding kinetics<sup>219–221</sup> in multimeric proteins. Because directly observing the real time spatial dynamics of ligands in proteins is experimentally very challenging,<sup>222,223</sup> atomistic simulations have become an attractive complementary technique for investigating such processes. There are a few examples for which the ligand dynamics could be observed in real time after preparing a well-defined initial state by photodissociating a ligand from a protein.<sup>224,225</sup> A system which is suitable to study such effects is the homodimeric hemoglobin HbI from *Scapharca inaequivalvis*. This protein has been characterized in structural,<sup>226,227</sup> thermodynamic,<sup>228</sup> kinetic<sup>222,229</sup> and computational<sup>216,230</sup> terms over the past 20 years. The accumulated information suggests that the dynamics at the interface is strongly influenced by structural changes and the water molecules between the two monomers. The most significant tertiary change between the deoxy (ligand unbound) and oxy

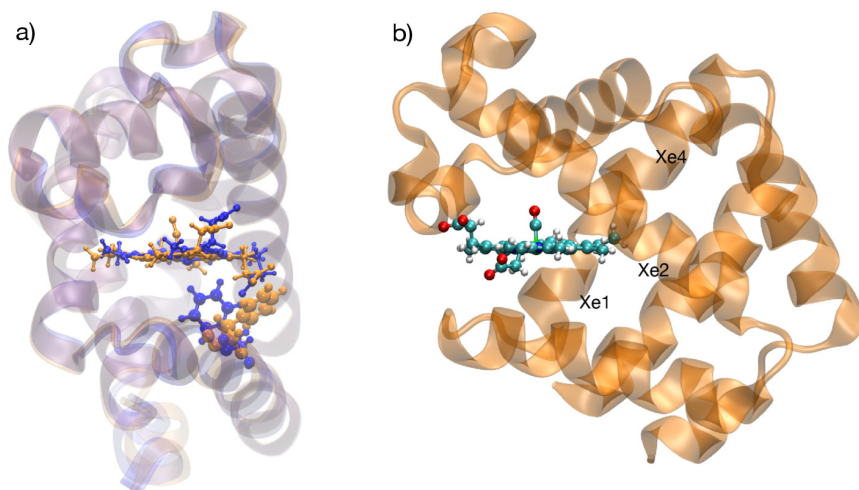


**Figure 5.1:** a)- The conformational change of the side-chain of Phe97 upon binding. Oxy and deoxy conformations are shown in orange and blue. The superimposed structures are taken from X-ray data. The protein is shown as cartoon representation and the heme and Phe97 residue as CPK representation. b)- It shows the location of Xe pockets inside the protein, Xe1 below the heme plane, Xe2 in the plane of heme and Xe4 pocket surrounded by A, B and G helix.

(ligand bound) state is the orientation of the phenyl side chain of Phe97 in which the  $\chi$  ( $C, C_\alpha, C_\beta, C_\gamma$ ) angle changes from  $50^\circ$  to  $160^\circ$  upon ligand binding.<sup>209</sup> The conformational change at the interface is accompanied by a change in the degree of hydration of the interface in that 17 water molecules are present in the deoxy state and only 11 water molecules are found for the ligand-bound protein. It has been proposed that the interfacial water molecules play a role in the subunit communication.<sup>230</sup> However, no precise, atomistically defined mechanism was suggested. Water molecules and the role of their dynamics at interfaces for regulating protein function have already been investigated for a longer time.<sup>231,232</sup>

### 5.1.1

#### Differences in the structures of oxy and deoxy state

There are two major structural differences found in the crystal state of oxy and deoxy state. These significant changes are due to different orientations of side-chain of Phe97 at the dimeric interface, whose dihedral angle  $\chi$  changes from  $\approx 50^\circ$  to  $\approx 160^\circ$  on binding of oxygen, Figure 5.1a. The other change

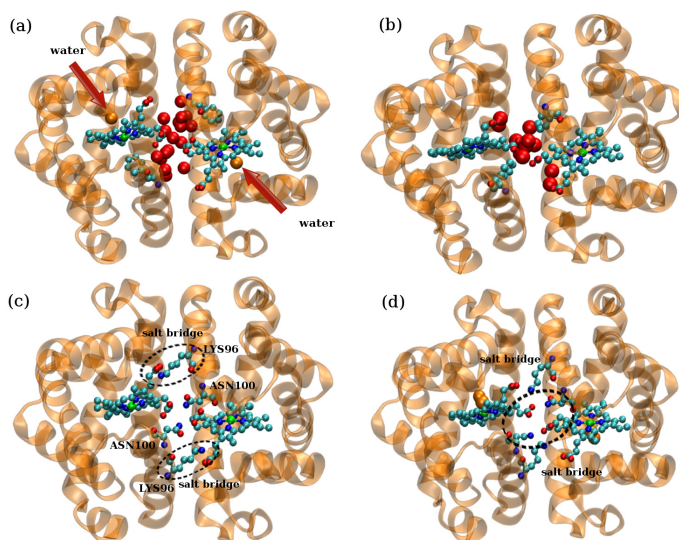


**Figure 5.2:** a) - correspond to the deoxy state of the protein with 17 interfacial water molecules. b) - correspond to the oxy state of the protein with 11 interfacial water molecules (red spheres). c) - deoxy state of the protein showing the salt bridge between Lys96 from one heme unit and propionate group of other heme subunit and d) - oxy state with broken salt bridge between Lys96 and propionate of the other heme subunit and formation of salt bridge between Lys96 and different propionate of the same heme. Oxygens of interfacial water molecules and water present in the heme pocket are shown in red and orange with CPK representation. The arrows indicate the crystallographic water present in the heme pocket. These known data are from the X-ray structures.

found in the oxy and deoxy state is the number of water molecules at the dimeric interface. This number varies from 11 to 17 in the oxy and deoxy state. This is shown in Figure 5.2a, b. Apart from this, the crystal structure of the deoxy state also have water molecule at the distal site<sup>209</sup> shown by an arrow in Figure 5.2a. The comparison between oxy and deoxy states further shows that during the oxy to deoxy state transition, the salt-bridge between Lys96 in one subunit and a propionate group of heme in the other subunit is replaced by the salt-bridge between Lys96 and a different propionate of the same heme, shown in Figure 5.2c, d. The breaking and formation of the salt-bridges acts as a gate for water molecules to move in and out of the interface.<sup>230</sup> The other difference is the distance between the heme center of two subunits, 16.56 Å in deoxy state to 18.43 Å in the CO-liganded oxy state. The overall quaternary difference between the CO-liganded state and deoxy state is relatively small, unlike in human hemoglobin.

All the experimental findings till now are based on data for either oxy or deoxy state. None of the previous studies account for the intermediate states which led to the finally observed experimental structures or the behavior of photodissociated CO. The specific questions that arise in the case of the homodimeric hemoglobin HbI concern the coupling between ligand migration pathways and their barriers on the one hand and modifications at the protein interface on the other hand. Specifically, it is of interest to understand how the heme-ligation-state in one subunit affects ligand migration in the second subunit and whether the dynamics at the interface transduces information. This can aid in understanding the cooperativity in this protein. How the dynamics for Phe97 flipping and water is coupled at the dimeric interface. What are the possible pathways for ligand migration inside the protein followed by photodissociation experiments. The presence of water molecules at the distal cite in the deoxy state crystal structure suggest that there must be a possible pathways for water to reach inside protein. This raises another question, whether the path for water insertion is the same as ligand binding pathway. Atomistic simulations is an alternative to study such problems and have repeatedly shown to be exquisitely useful to address such questions, both in qualitative and in quantitative terms. The understanding of protein dynamics at the atomistic detail cannot be easily obtained through experiments. MD simulations has provided fruitful insights and answered questions regarding protein dynamics, ligand binding and folding.<sup>233–236</sup>

## 5.2 Theoretical methods

For the MD simulations, crystal structures 2GRH<sup>237</sup> and 2GRF<sup>237</sup> from the PDB database are used for oxygenated and deoxygenated HbI structures, respectively. Both structures are M37V mutants of wild-type *Scapharca inaequivalvis* dimeric hemoglobin. The mutation was introduced to enlarge the distal pocket which was found to lower geminate rebinding of oxygen in solution. At the same time cooperative ligand binding is maintained and proceeds along structural transitions as wild-type HbI.<sup>237</sup> The structure of the protein is shown in Figure 5.3. HbI contains two subunits with one heme group each. Each subunit can be in an oxy (b, ligand-bound) or deoxy-state (u, unbound; e, empty) individually. From the available PDBs, the protein is found to be either both heme oxidized or deoxidized. No structural information is available regarding the mixed states

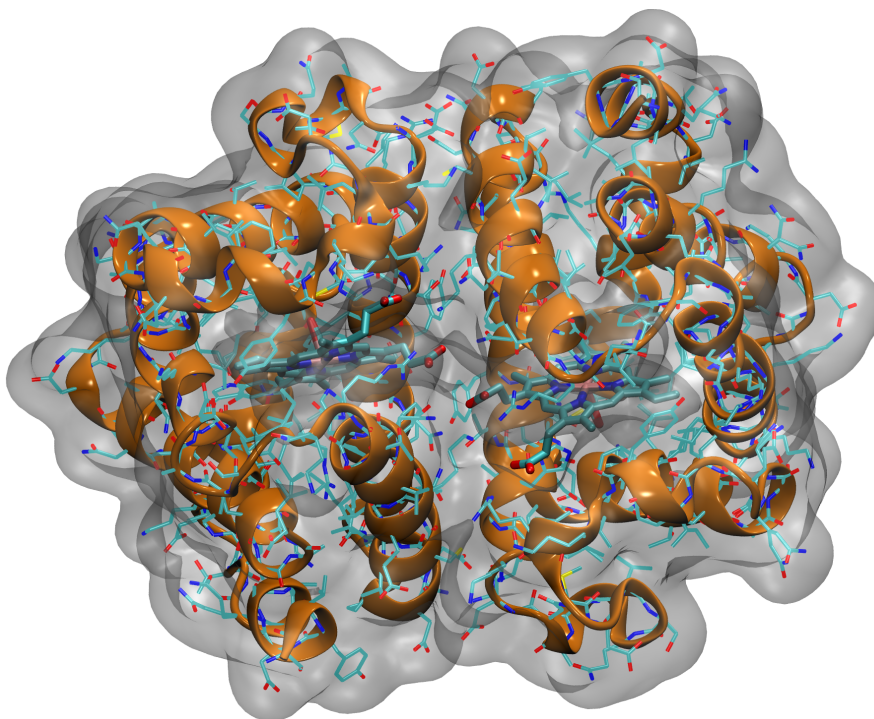


**Figure 5.3:** The structure of protein in cartoon representation (orange) with the heme and bound CO ligand in line representation. PDB structure 2GRH

either experimentally or theoretically. Therefore, there are different possibilities to study, depending upon the ligation state of heme groups in each monomer unit. There are both subunits deoxidized (1e2e), both subunits oxidized (1b2b), two mixed states (1e2b and 1b2e). Apart from the above studied systems, there are other intermediate states prepared depending upon the binding state of carbon monoxide (CO) with the iron atom of heme subunits. Both heme group contain CO but in unbound states (1u2u), two mixed states in which both units are oxidized but one in unbound state (1u2b and 1b2u) and in other two states in which one heme unit is in deoxidized state and the other oxidized but unbound (1e2u and 1u2e). The labels “b”, “u” and “e” corresponds to oxidized (bound), oxidized but not bonded to iron (unbound) and deoxidized (empty) states. The unbound states are prepared by removing the bond between iron atom of heme and carbon of carbon monoxide (CO). The deoxidized state is prepared by removing the bound CO and having the five coordinated potential for heme subunit. It was necessary to differentiate between the heme groups in mixed state, so from the force field point of view they had different parameters in order to maintain the domed structure of five-coordinated heme.

All the above systems were prepared using CHARMM.<sup>238</sup> Molecular dynamics (MD) simulations were carried out on all the above prepared systems using NAMD<sup>239</sup> with the CHARMM22 force field. Molecular dynamics simulation consisted of minimizing the starting structures to remove unrealistic contacts by the conjugate gradient methods, slowly heating the system upto 300K during 1.2 ns, followed by 1 ns of equilibration at constant temperature and pressure (NPT ensemble) and finally 100 ns of production in the NPT ensemble. The SHAKE<sup>240</sup> algorithm was used to constrain all the fast vibrational motions of hydrogen atoms. The nonbonded interaction was truncated at 16 Å, using a switching function starting from 12 Å. The nonbonded list was calculated for pairs within 16 Å. The protein was neutralized by adding explicit counterions (16 Na<sup>+</sup> and 18 Cl<sup>-</sup> ions) at physiological concentration (0.154 mol/L). The fully solvated systems contain 46216 number of atoms. The pictorial representation of protein is shown in Figure 5.3. After running MD simulations for 100 ns of each systems i.e. (1b2u, 1u2b, 1b2e, 1e2b, 1b2b, 1e2e) with NAMD we observed some important results, which shows the presence of dynamical asymmetry associated with individual heme units which leads to asymmetrical occupation states of CO to internal Xe pockets in two heme subunits. To calculate the number of water molecules at the dimeric interface we draw a sphere of 10.4 Å radius, centered around the center of mass of two heme subunits. Umbrella sampling were performed for estimating the free energy barriers for CO migration to different internal Xe cavities. The data from umbrella sampling<sup>241</sup> were analyzed with the weighted histogram analysis method (WHAM).<sup>242,243</sup> Umbrella sampling simulations were performed with a force constant of 5 kcal/mol/Å<sup>2</sup>, with step-size of 0.3 Å, considering Fe-CO distance as a reaction coordinate. The step size is chosen such as to have between 25 and 35 overlapping windows per reaction coordinate. The simulation time for each window is 51 ps, 1 ps of relaxation and 50 ps for production. Overall, a total of 45 ns simulation data was analyzed for two of the above studied systems. It has also been observed that individual subunit in these systems are identical but they don't behave similarly and it will be discussed later. Following section discuss the results which include role of Leu36 and Trp135 residue for ligand dynamics inside protein, time-average behavior of Phe97 residue coupled with water dynamics at the interface as well as dynamics of water itself inside the protein and calculation of the free energy barriers for the CO migration to different pockets.

## 5.3 Results

### 5.3.1 Role of Leu36 and Trp135 residue in CO migration

The migration of ligands within proteins often requires conformational changes that facilitates the movement of ligand between the internal cavities to their binding sites.<sup>244</sup> In case of myoglobin, ligand entry and exit from the distal pocket, is facilitated through distal histidine (His) gate. However, the distal histidine gate is not universally found among globins.<sup>245</sup> Additional complexities arises in case of dimeric HbI, where distal histidine now participates in inter subunits contacts. There are few experimental<sup>216,218,237</sup> and theoretical studies<sup>216</sup> made for the blood clam *Scapharca inaequivalvis*, where CO binds reversibly at the distal pocket with no known channel for ligand migration to other internal cavities or into the solvent. From time-resolved crystallography data,<sup>245</sup> it is known that there are 4 Xe site inside dimeric HbI, named as Xe4a, Xe4b, Xe2 and Xe1. The Xe4 sites are lined by B, G and E helix. Xe2 cavity lies in the plane of heme and Xe1 cavity is below the plane of heme, occupied by the Phe97 residue in unliganded HbI. All these cavities are shown in Figure 5.1b for a single monomer unit. In our present study, number of observations has been made regarding the migration of CO in the internal cavities of dimeric HbI: (1) Leu36 residue acting as a gate for the migration of ligand (CO) from the distal pocket to the other internal cavities. (2) Trp135 residue which connect the Xe4 and Xe2 cavities and (3) dynamical asymmetry present due to different occupation states of CO in those internal cavities as well as difference in the time scale for the migration of CO in the individual subunits of protein. What follows now is the result obtained for different studied systems.

**1b2u:** In this studied system migration of CO in the unbound unit is observed around 5 ns to other internal cavity of the protein, mainly Xe4 and remain there for 40-45 ns, after which it return back to the distal pocket and then migrates back to Xe4. However it doesn't stay in Xe4 pocket for long time and migrates to Xe2 and stay there for rest of the simulation time (B → Xe4 → B → Xe4 → Xe2). This migration dynamics of CO is observed by the change in

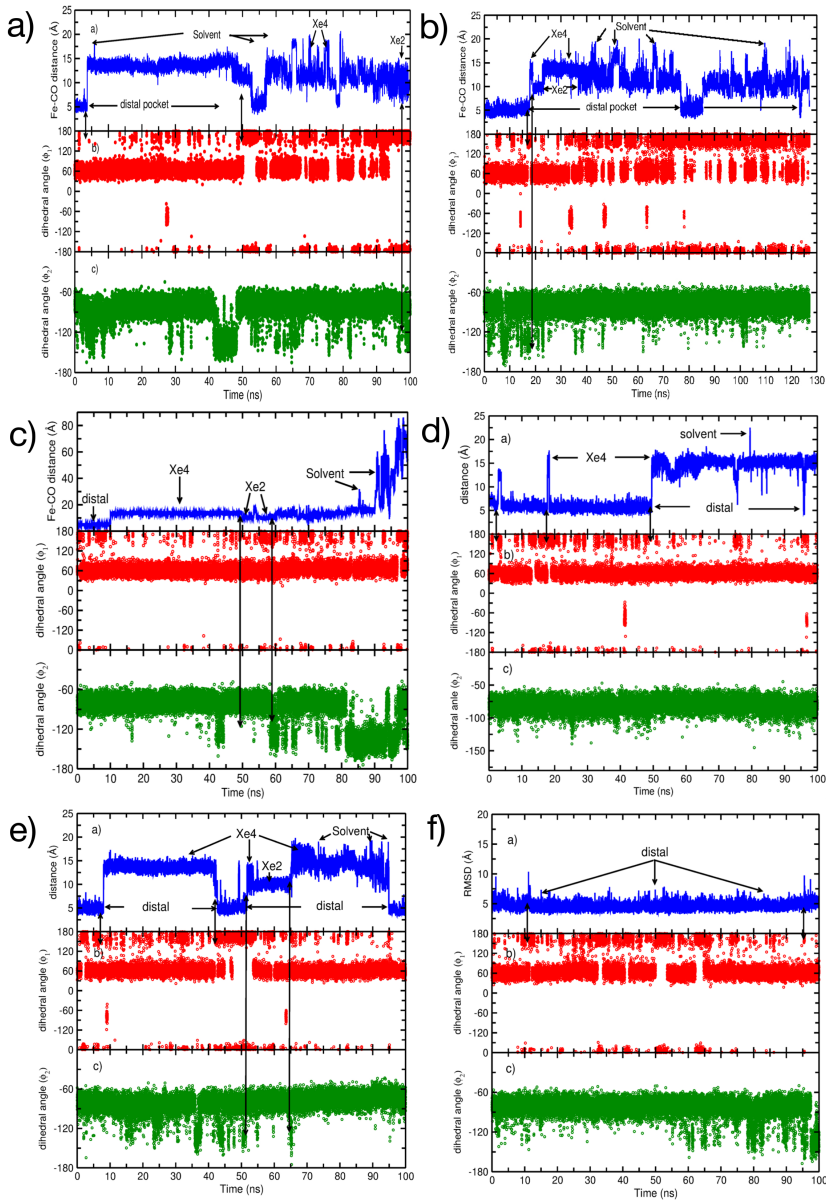


**Figure 5.4:** The data shown here is for 5 different systems. a)- 1b2u, b)- 1u2b, c)- 1e2u, d)- 1u2e, e)- 1u2u subunit P1 and f)- 1u2u subunit P2. Each of these figures contain a)- distance between Xe and CO b)- dihedral angle of Leu36 and c)- dihedral angle of Trp135.



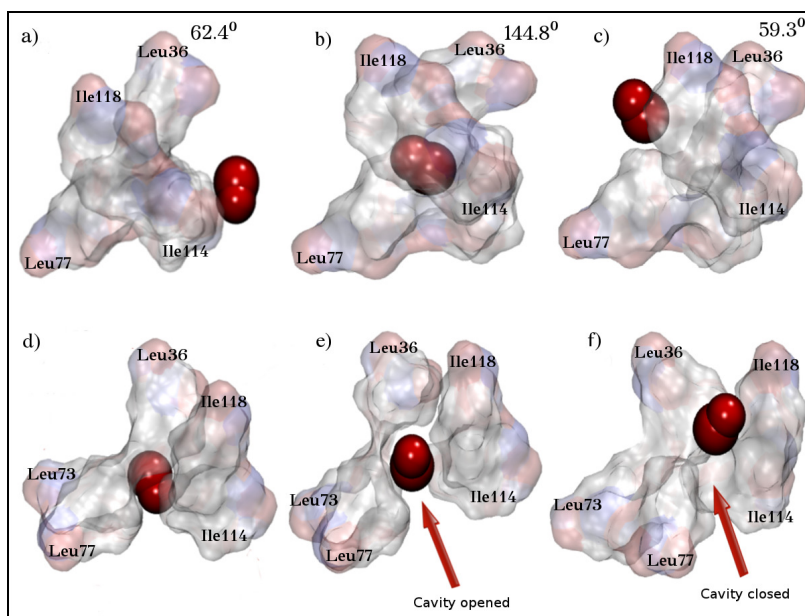


**Figure 5.5:** Surface representation of Leu36, Ile114, Ile118, Leu77 and Leu73 residues and changes regarding the dihedral angle of Leu36. a, b, c shows the side view of the CO molecule and the residues forming the gate between protein internal cavities and distal pocket and d, e, f shows the front view before, during and after the migration of CO from distal pocket. Figure b clearly shows the change in Leu36 dihedral angle as the Leu36 surface gets broaden during the migration and comes to the initial state as shown in a and c. CO molecule is shown in CPK representation in red color. All the residues around the heme pocket is labeled.

the distance between Fe and CO molecules together with the conformational change observed in side chain dihedral angle of Leu36 and Trp135 residue which link the migration of CO molecule from the distal pocket to either Xe4 or Xe2 cavity, shown by an arrow in Figure 5.4a. The change in the dihedral angle of side chain of the Leu36 ( $C_{\alpha}$ ,  $C_{\beta}$ ,  $C_{\gamma}$ ,  $C_{\delta 1}$ ), from  $60^{\circ}$  to  $160^{\circ}$ , shown by an arrow in Figure 5.4a, around 5 and 45 ns, provide spatial freedom for CO molecule to migrate in and out of the distal pocket. This is clearly shown in Figure 5.5, where the surface representation of residues forming the distal pocket is shown. From Figure 5.5, one can observe the opening and closing of the gate due to conformational change in Leu36 residue, which is also observed in the oxy and deoxy crystal structure of HbI.<sup>209</sup> Migration of CO molecule to Xe2 cavity happens due to conformational change in Trp135 residue. The change in the dihedral angle ( $C_{\alpha}$ ,  $C_{\beta}$ ,  $C_{\gamma}$ ,  $C_{\delta 2}$ ) of side chain of Trp135 from  $-60^{\circ}$  to  $-160^{\circ}$  create a passage for CO to move into Xe2 cavity. This change can be observed around 95-100 ns as shown in Figure 5.4a. The arrow indicative of the solvent

in Figure 5.4a shows the attempt made by CO to reach the exterior of Xe4 cavity connected to the solvent. Figure 5.6(a) shows a pictorial representation for the unbound subunit of protein with occupation of CO inside protein for entire 100 ns simulation.

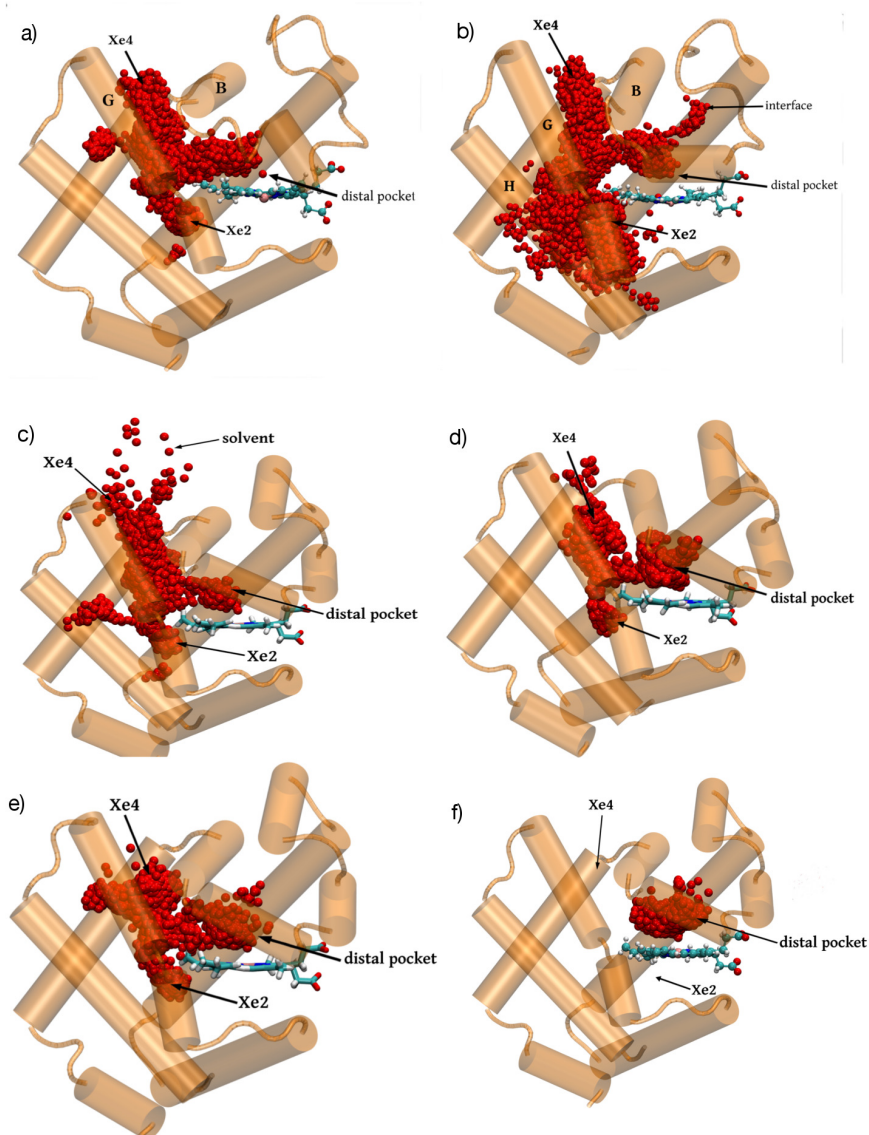


**Figure 5.6:** The data reported here is for 5 different systems. a)- 1b2u, b)- 1u2b, c)- 1e2u, d)- 1u2e, f)- 1u2u-P1 and g)- 1u2u-P2 system. Dynamics of CO molecule taken as a snapshot in the unbound monomer unit over the entire 100 ns trajectory. CO molecules are represented by red balls.

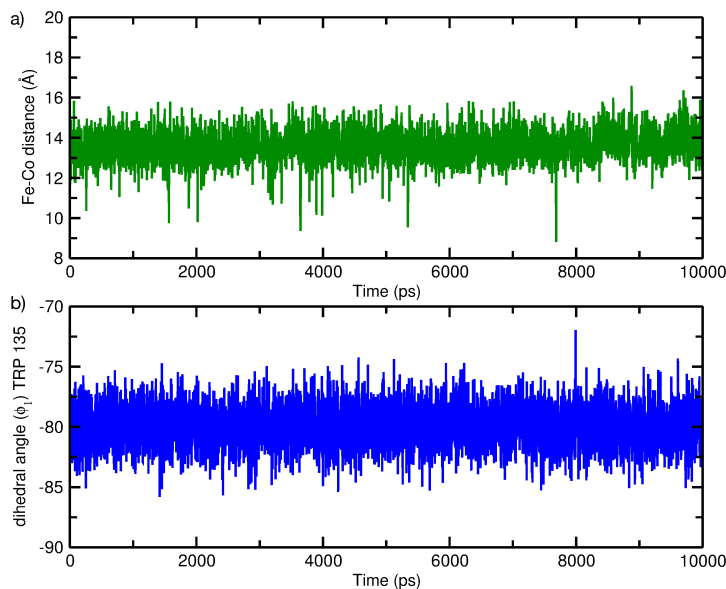


**Figure 5.7:** It shows the data for the dihedral angle of Trp135 and Fe-CO distance for 1u2b system for 10 ns during the constraint dynamics of 1u2b system. a)- represent the Fe-CO distance and b)- represents the change in the dihedral angle of Trp135 as a function of time.

**1u2b:** Migration of CO in this system is different from 1b2u discussed above. From Figure 5.4b it can be seen that migration of CO from distal pocket to Xe4 occurs around 20 ns, followed by the migration of CO to Xe2. This migration to Xe2 happens due to the conformational change in Trp135 residue, shown by an arrow in Figure 5.4b. The Fe-CO distance plot in Figure 5.4b shows frequent migration of CO between Xe4 and Xe2 cavities within 50 ns. This is clearly shown in Figure 5.6(b) where the occupation state of CO molecule over the entire trajectory is plotted. There is frequent migration of CO between Xe2 and Xe4 in 1u2b compare to 1b2u system as shown in Figure 5.6(b). This is due to frequent fluctuation in the conformation of Trp135 side chain. Comparing the initial migration time between 1b2u and 1u2b from our simulation shows the presence of asymmetry in the time scale of migration. This time-asymmetry for CO migration is also observed in the time-resolved crystallographic study as well.<sup>216</sup> From Figure 5.6(b) it can be also be seen that CO shows tendency to migrate through another route between helix G and H, not found in 1b2u. In order to make sure that conformational change in the dihedral angle of Trp135 residue is responsible for the migration of CO from Xe4 to Xe2 cavity, we performed a test simulation for 10 ns in which the

dihedral angle of Trp135 residue was held constant around  $-80^\circ$ . This data is reported in Figure 5.7, which gives clear indication that CO remain in Xe4 pocket and never migrated to Xe2 pocket. This also indicates that change in the side chain dihedral angle of Trp135 is an essential component for CO migration to Xe2 pocket.

**1e2u:** Migration behavior of CO in this system is very similar to 1b2u. Figure 5.4c shows the Fe-CO distance together with the behavior of Leu36 and Trp135. The data clearly indicates high propensity for CO to occupy Xe4 cavity compare to Xe2. It can be observe from Figure 5.4c that conformational change in Leu36 around 5-10 ns initiate CO migration to the Xe4 pocket. However after 45 ns first conformational change in Trp135 led CO to reach the Xe2 pocket but never stay there for long. Figure 5.6(c) shows a pictorial representation for the unbound subunit of protein with occupation of CO inside protein during entire 100 ns simulation. It can be observed from Figure 5.4c that CO ligand diffuses into the solvent after 90 ns through Xe4 cavity. This cavity is speculated as the major pathway (BG pathway)<sup>245</sup> for the CO migration but had not been explicitly observed before, either in photolysis experiments or in MD simulations.

**1u2e:** Similar to the 1e2u, migration of CO is restricted to Xe4 for most of the simulation time as can be seen from the Fe-CO distance profile in Figure 5.4d. This suggest that CO occupy Xe4 with higher probability to compare to Xe2 during 100 ns of simulation time. Occupation state of CO observe from 1e2u or 1u2e is restricted to Xe4 when one of the subunits of protein is in the deoxy state. Figure 5.6(d) shows a pictorial representation for the unbound subunit of protein with occupation of CO inside protein during entire 100 ns simulation.

**1u2u:** From the Fe-CO distance data plotted in Figure 5.4e and 5.4f, it can be observed that migration of CO is observed only in one of the subunits (P1) and in the other subunit (P2), CO remains in the distal pocket. This is quite surprisingly as CO is unbound in both the subunits and have equal probability to migrate to either of these Xe cavities. Comparing Figure 5.4e and 5.4f one can observe that although the Leu36 conformational behavior are almost same in both subunit, however CO doesn't migrate in one of the subunits. This indicate that opening of Leu36 gate doesn't guarantee the migration of ligand

however for each migration of ligand, Leu36 gate must be open. Figure 5.6e and 5.6f, shows the occupation states of CO in different cavities over 100 ns time scale.

It would be of interest to understand the dynamics of one individual monomer units either in 1u2b or 1b2u to find out whether the unbound/bound units behaves similarly or independent of the overall state of the system. In order to find out the differences we calculated the RMSF of individual residues in the bound and unbound units of both 1b2u and 1u2b systems and made one-to-one comparison. The data for this comparison is shown in Figure 5.8 (top) and Figure 5.8 (bottom). From Figure 5.8 (top) one can observe that the difference in the RMSF value for the  $C_{\alpha}$  atoms in the bound subunits of 1b2u and 1u2b are relatively small and the difference for residues 38-45 is due to the random loop slightly being twisted and residues 110-116 is due to spatial movement of small part of helix. This data is compared with the RMSF value evaluated from the experimental B-factor data from the PDB of oxy state. Figure 5.8 (bottom) shows the compared RMSF data for unbound subunits in 1b2u and 1u2b systems. For the unbound states the differences lies mainly in the residues 40-60 which is due to spatial movement of the random loop and residue 110-116 which is due to same helix movement as in the bound state. This RMSF data obtained from simulations is compared with the RMSF value obtained from experimental B-factor data of protein.

From all the above studied system it can be concluded that (1) time scale regarding migration of ligand CO to Xe pockets is not same in both the subunits of protein and early migration of CO is preferred in subunit 1, (2) CO has higher probability to occupy Xe4 compare to Xe2 and (3) Xe1 is never visited by CO during the entire simulation, because this cavity is surrounded by 3 phenyl ring which makes the space crowded and reduce the probability to be occupied by CO molecule. Similar trend for occupation of CO ligand is observed in time-resolved crystallographic experiment,<sup>216</sup> however these experiments doesn't shows the clear indication for the key residues responsible for the ligand migration inside the protein. This difference in the occupation of CO in internal Xe cavities state leads to inherent asymmetry within the subunits regardless of the global symmetry of the entire protein. The main cause of this different migrating behavior lies in different dynamics of specific residue (Trp135) within a monomer unit of protein. Similar asymmetrical observation for ligand diffusion was reported before by Chiancone et. al.<sup>227</sup> and Knapp et. al.<sup>216</sup>

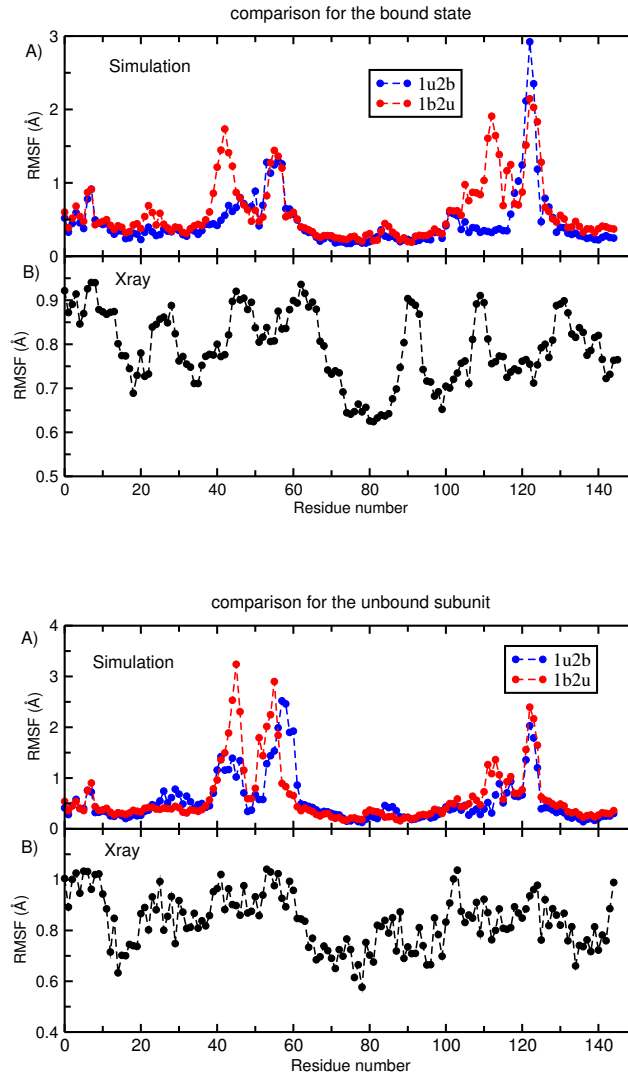


**Figure 5.8:** top- RMSF value for each C $\alpha$  atoms of the protein and the comparison is made between the bound units in 1u2b and 1b2u systems, i.e. 2b<sub>1u2b</sub> vs 1b<sub>1b2u</sub>. The B-factor is taken from the oxy state of the protein. bottom- RMSF value for each C $\alpha$  atoms of the protein and the comparison is made between the unbound units in 1u2b and 1b2u systems, i.e. 1u<sub>1u2b</sub> vs 2u<sub>1b2u</sub>. The B-factor is taken from the deoxy state of the protein.

### 5.3.2 Presence of water in distal pocket

The presence of single water molecules in the distal pocket of the deoxy state crystal structure suggest the possibility of water molecule to enter inside the protein either through the solvent or through the distal histidine gate present at the dimeric interface. It is likely that a swinging distal histidine gate in the dimeric interface could accommodate the entry of water molecules, suggesting a more direct route for water to enter the distal pocket. This diffusive behavior of interfacial water molecule into the distal pocket is observed in 1b2u system as shown in Figure 5.9 (top). Similar behavior for water diffusion to distal pocket is also observed for 1u2b system as shown in Figure 5.9 (bottom). However migration of water from the interface doesn't neglect the possibility of water diffusion from the solvent to the distal pocket. From our simulations it is also found that water from the solvent diffuses inside the protein shown as snapshots from the simulations in Figure 5.10, through the “**BG pathway**”.<sup>216</sup> Diffusion of water from the solvent to the distal pocket in the presence of CO inside the protein suggest multiple ligand occupancy. However both water and ligand don't occupy the same cavity at the same time inside the protein which can be seen in Figure 5.10. Water diffusion inside the protein found in our simulations suggest different possible pathways and a qualitative explanation for the presence of crystallographic water in the distal pocket in the crystal structure of deoxy state.

### 5.3.3 Structural changes at the dimeric interface

As for human hemoglobin, the X-ray crystallographic studies on deoxy and liganded-HbI reveal the details of the structural rearrangements that occur upon ligand binding. The backbone atoms of the deoxy- and oxy species are very similar in structure with an RMSD difference of 0.6 Å, indicating that no significant ligand-related quaternary changes takes place.<sup>209,246</sup> Tertiary structural transitions include the movement of Phe97 (F4), which is tightly packed against the proximal histidine His-101 in the deoxy state (2GRF), but extrudes into the dimer interface in the oxidized species (2GRH), where it disrupts the well ordered water molecules. The dihedral angle ( $\chi$ ) for Phe97 {C, C<sub>α</sub>, C<sub>β</sub>, C<sub>γ</sub>} is  $\approx 42^\circ$  and  $162^\circ$  for deoxy and oxy state of hemoglobin.

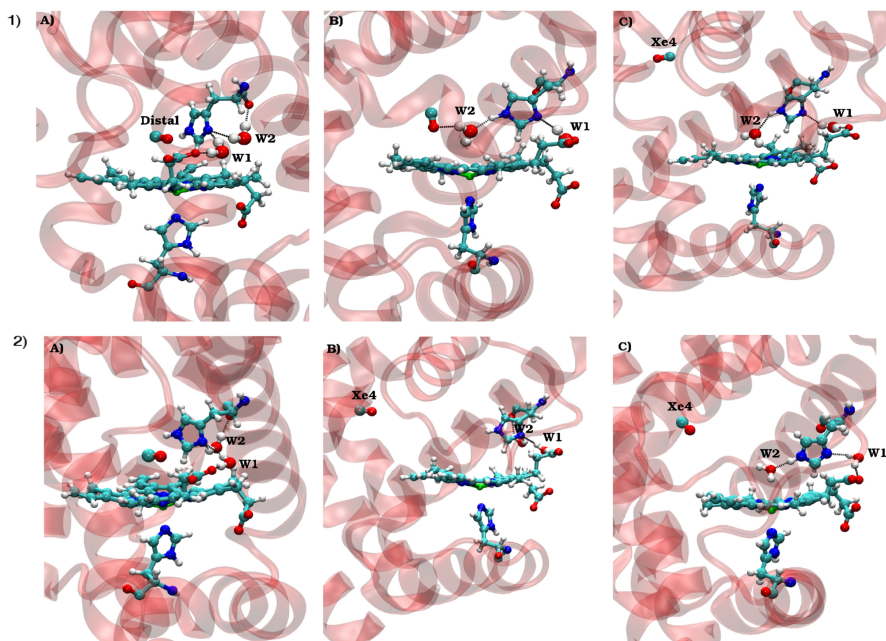


**Figure 5.9:** The data reports 1)- 1b2u and 2)- 1u2b systems. It shows the snapshots for the migration of CO to Xe4 pocket and occupation of crystallographic water molecule(W2) to distal pocket in 1u2b. W1 and W2 are the crystallographic water molecule close to histidine residue, W2 forming hydrogen bond with histidine and W1 forming hydrogen bond with histidine and propionate group. W1 molecule is very stable and don't migrates during the whole course of simulation. a)- showing the CO molecule and position of crystallographic water molecule (W1 and W2), b)- water molecule(W2) and CO both in the distal pocket and c)- water occupying the distal pocket and CO migrates to Xe4. Bond between proximal histidine and Fe is not shown.



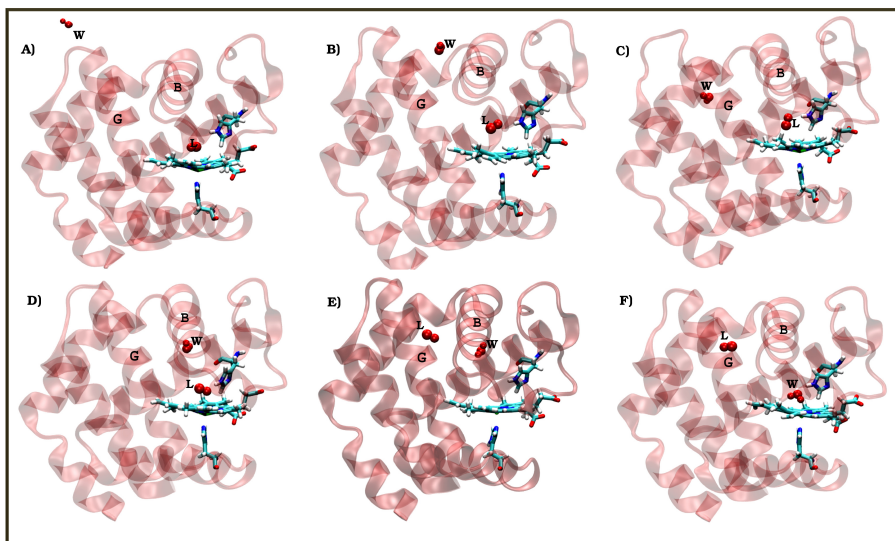


**Figure 5.10:** It shows the snapshots for the migration of a single water molecule from the solvent to the internal cavities through BG pathway in of one monomer occupying the distal pocket after the migration of CO to Xe4 pocket. L represent the CO molecule, W represent water. A)- shows the water(W) outside the protein, B)- represent the water within the B and G helix, C)- represent water occupying the Xe4 pocket D)- water close above the distal pocket below the helix B, E)- shows the migration of CO from the distal pocket F)- shows the CO molecule in Xe4 pocket and water occupying the distal pocket.

Thus 6 out of 17 water molecules that characterize the dimeric interface are absent in the liganded (oxidized) protein. Thus the salt bridge of Asn100 with propionates in the deoxy derivative, is no longer present in the liganded species, whereas at the same time rupture of salt bridges of Lys96 from one heme propionate to other. These residues are shown in Figure 5.2. Therefore the structural changes underlying the cooperative binding appeared to be more localized within a symmetrical unit at the interface including two heme pockets. These known facts regarding the change in number of water molecules at the dimeric interface, dihedral angles ( $\chi$ ) of Phe97, distance between center of mass between two heme units, iron-iron distance and other structural parameters are observed for different systems and are discussed below.

**1b2u:** This intermediate state corresponds in which first subunit is in the oxy state while the other subunit is oxidized but the CO is in the unbound state. To check the stability and the presence of large movement of the protein the RMSD is calculated for protein and has value around 2 Å (not shown here).

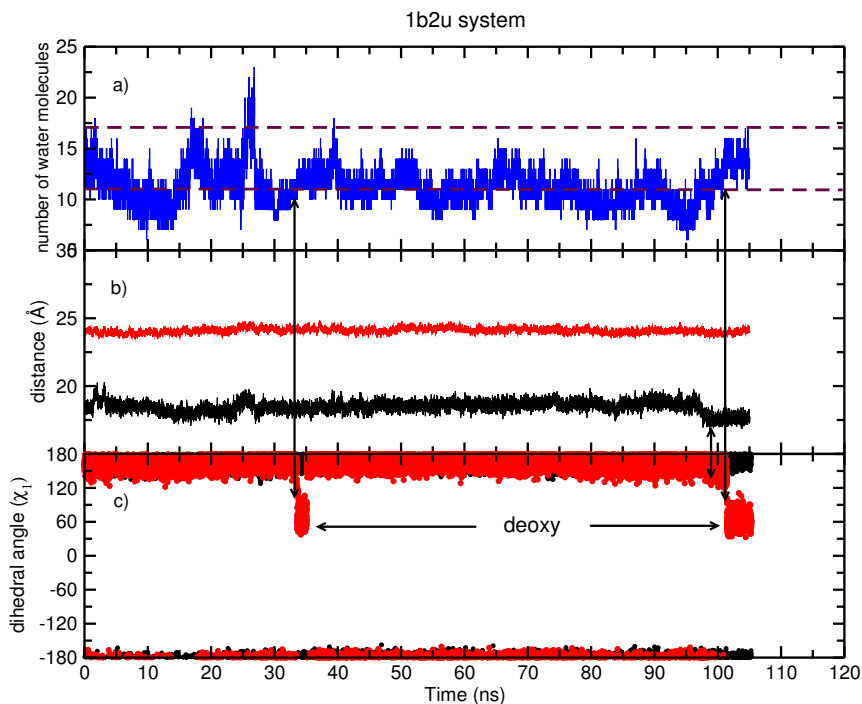


**Figure 5.11:** These data are shown for 1b2u system a)- Number of water molecules at the dimeric interface, b)- distance between the COM of monomer units (red) and Fe-Fe center (black) of two heme subunits and c)- change in dihedral angle of Phe97. The word “unbound” corresponds to the dihedral angle of Phe97 in the deoxy state of the protein. Data shows the correlation between the flipping of Phe97 and number of water molecules at the dimeric interface.

The dihedral angle change for Phe97 is observed and plotted as a function of time in Figure 5.11c. Change in the dihedral angle is accompanied by the slight increment of water molecules at the interface as shown in Figure 5.11a. These results are manifestation of coupled dynamics associated with flipping of the Phe97 side-chain and intrusion of water molecules at the dimeric interface. The final conformation for Phe97 observed from our simulations indicate the tendency of the unbound subunit to attain the deoxy state once the bond between CO and Fe is removed. The distance between the heme units also changes after the conformation of Phe97 and number of water at the interface increased, plotted in Figure 5.11b, during the time scale of our simulation.

**1u2b:** This intermediate state corresponds in which first subunit is oxidized but CO is in the unbound state while the second subunit is in the oxy state. To check the stability and large movement of the protein the RMSD is calculated

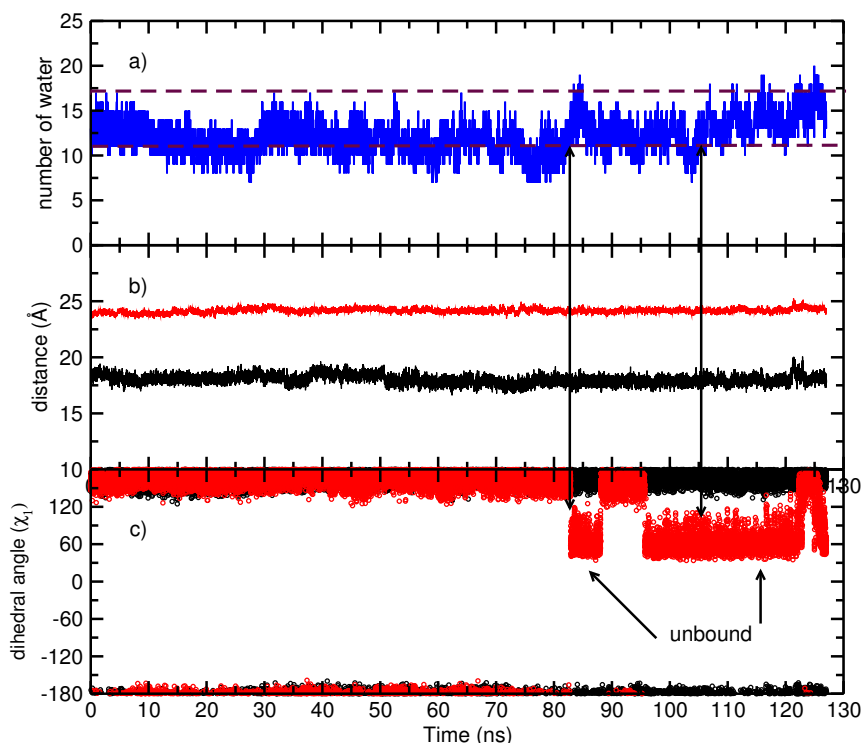


**Figure 5.12:** These data are shown for 1u2b system a)- Number of water molecules at the dimeric interface, b)- distance between the COM of monomer units (red) and Fe-Fe center (black) of two heme subunits and c)- change in dihedral angle of Phe97. The word “unbound” corresponds to the dihedral angle of Phe97 in the deoxy state of the protein. Data shows the correlation between the flipping of Phe97 and number of water molecules at the dimeric interface.

for protein (not shown here), with its value around 2 Å. There are cascade of processes happening at the dimeric interface as observed from our simulations. The change in the conformational state of side-chain Phe97 dihedral angle ( $\chi$ ) led the phenyl ring to move underneath the heme ring which consequently increases the number of water molecules at the dimeric interface and slightly reduce the Fe-Fe distance between two protein subunits. These results are plotted in Figure 5.12. From Figure 5.12a and 5.12c it can be observed that the number of water molecules at the interface mostly remains between fully oxy or fully deoxy states, however when there is conformational change in the dihedral angle of Phe97, intrusion of water molecules starts at the dimeric interface and the value reaches around 17, found in the crystal structure of deoxy state. These changes are shown by black arrow in Figure 5.12. The increase of water molecules at the dimeric interface followed by conformational change in Phe97

is rather slow, indicative of breaking and formation of hydrogen bonds among waters and side chains of the protein at the interface. These changes are consistent with the data for the 1b2u system mentioned above.

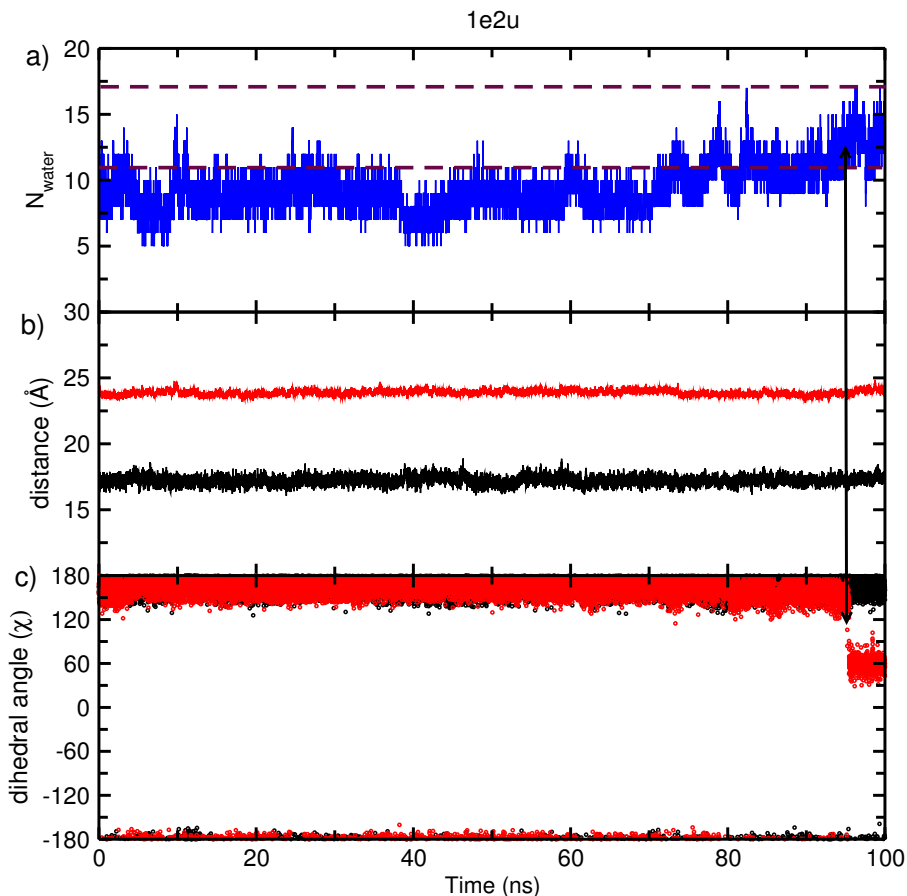


**Figure 5.13:** These data are shown for 1e2u system a)- Number of water molecules at the dimeric interface, b)- distance between the COM of monomer units (red) and Fe-Fe center (black) of two heme subunits and c)- change in dihedral angle of Phe97. Data shows the correlation between the flipping of Phe97 and number of water molecules at the dimeric interface.

**1e2u:** This intermediate state correspond in which the subunit 1 is in deoxy state while subunit 2 has unbound CO present in the distal pocket. RMSD data for this protein (not shown) has value around 2 Å during 100 ns of simulations, which suggest that there is no large quaternary structural changes in the protein on this time scale. Time series data for the number of water molecules at the interface, change in the dihedral angle of Phe97 and distance between Fe

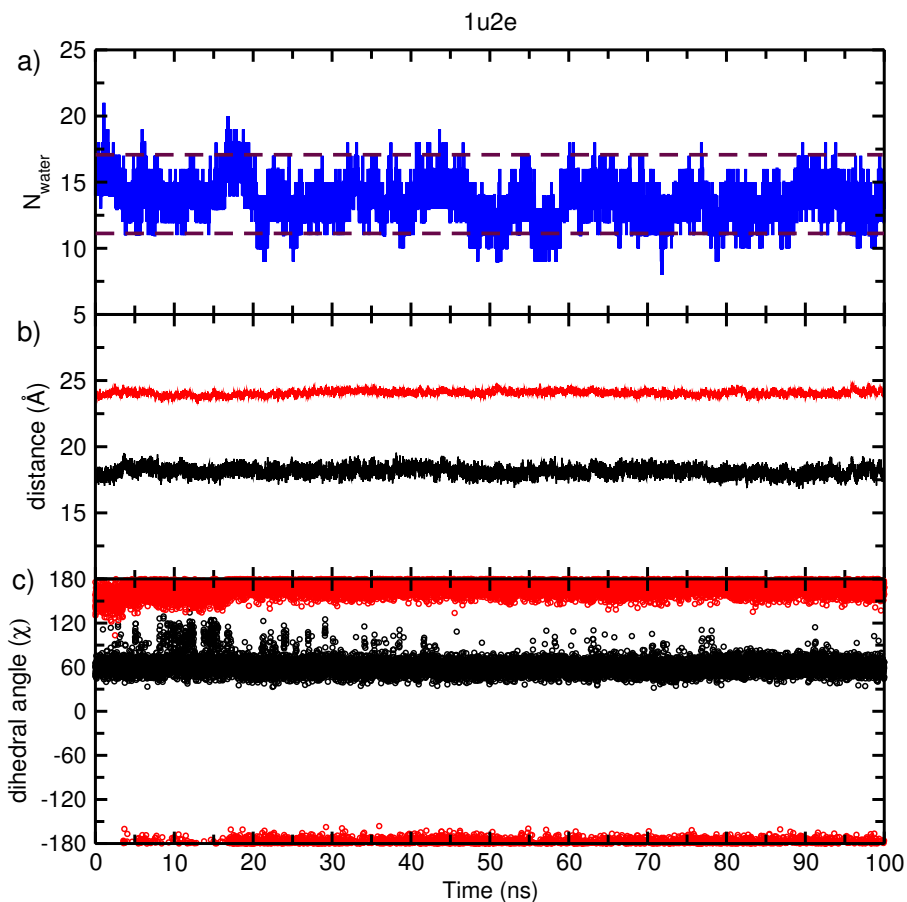


**Figure 5.14:** These data are shown for 1u2e system a)- Number of water molecules at the dimeric interface, b)- distance between the COM of monomer units (red) and Fe-Fe center (black) of two heme subunits and c)- change in dihedral angle of Phe97. Data shows that subunit 1 has conformation characteristic of deoxy state.

centers are plotted in Figure 5.13. From the data shown in Figure 5.13 shows the presence of coupled dynamics between Phe97 and water at the interface, similar to the other two above mentioned systems, however flipping of the Phe97 side chain took place around 95 ns.

**1u2e:** This intermediate state correspond in which the subunit 2 is in deoxy state while subunit 1 has unbound CO present in the distal pocket. The change in the number of water molecules at the interface, dihedral angle of Phe97 and distance between Fe centers are plotted in Figure 5.14. In this system the Phe97 conformation in the one of the system was initially set to deoxy state

conformation. The number of water molecules at the dimeric interface was found on average greater than that of other above mentioned system, due to the conformation of Phe97 residue.

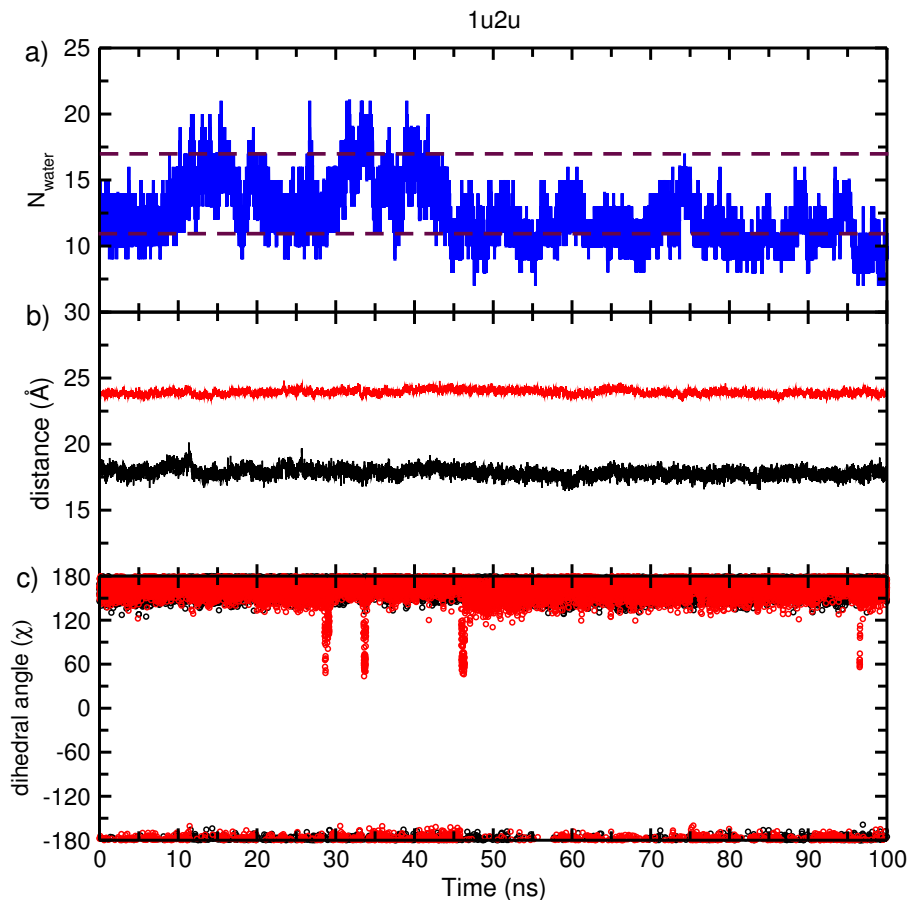


**Figure 5.15:** These data are shown for 1u2u system a)- Number of water molecules at the dimeric interface, b)- distance between the COM of monomer units (red) and Fe-Fe center (black) of two heme subunits and c)- change in dihedral angle of Phe97. In this studied system the conformational change for Phe97 was not observed for long time.

**1u2u:** This intermediate state correspond in which both the subunits are in unbound state. The change in the number of water molecules at the interface, dihedral angle of Phe97 and distance between Fe centers are plotted in Figure 5.15. From the data plotted, one can observe that conformational change made by Phe97 was not consistent for long time, which also doesn't allow more number of water to accommodate at the interface. The data for water shown

has some inconsistencies around 15 and 35 ns. These water molecules are not the one at the interface, but one which gets close to heme bottom from other side and are over counted in the calculations.

From the data regarding structural changes discussed above, one understands how conformational change in the Phe97 dihedral angle leads to inclusion of water molecule at the interface, which is the only conformational change known from the crystal structures. Other important structural observable is the distance between the iron centers known from the crystal data which is shown in Figure 5.11 as well. However within the time scale of the simulations we haven't observed the decrease in the distance between iron centers. One possible reason for the decrement in the distance might be related to the small rotation ( $3.3^\circ$ ) of one monomer unit with respect to other as found in the crystal structure or the conformation for both the Phe97 residue should be similar as in the deoxy state ( $45.6^\circ$ ). Which of these processes triggers each other is still a valid and an open question. Apart from this we can see from Figure 5.11, number of water molecules at the interface, change in dihedral angle of Phe97 and distance between two iron centers are slightly off the experimental value from the crystal structure, shown as a brown dash line. One possible explanation could be the final state of the dynamic system, which never samples the complete deoxy state, in which both the subunits the Phe97 residue is found below the heme plane. Another experimental reason could be the crystal packing and the temperature at which the crystal data was obtained, whereas we observed data at 300K in our simulations. Apart from these structural changes inside the protein there are some global structural changes which lead towards the progression of R  $\rightarrow$  T transition. Two of these important parameters are the iron-iron distance and the change in the rotation angle between two monomer units in R and T state.<sup>237</sup> Within the time scale of our simulations we observed 1 Å of decrement in the iron-iron distance for 2 of our studied system, which is half the value of experimental difference. However the experimental data is for oxy or deoxy state. This suggests that for the difference of 2 Å, the Phe97 conformation in the other subunit should be similar to deoxy state. These observations are consistent with the experimental observation made by Knapp et. al.,<sup>237</sup> where the distance change starts occurring at around  $1\mu\text{s}$  and a rotation of  $0.6^\circ$  from the R state is observed by  $80\mu\text{s}$ .<sup>223</sup>

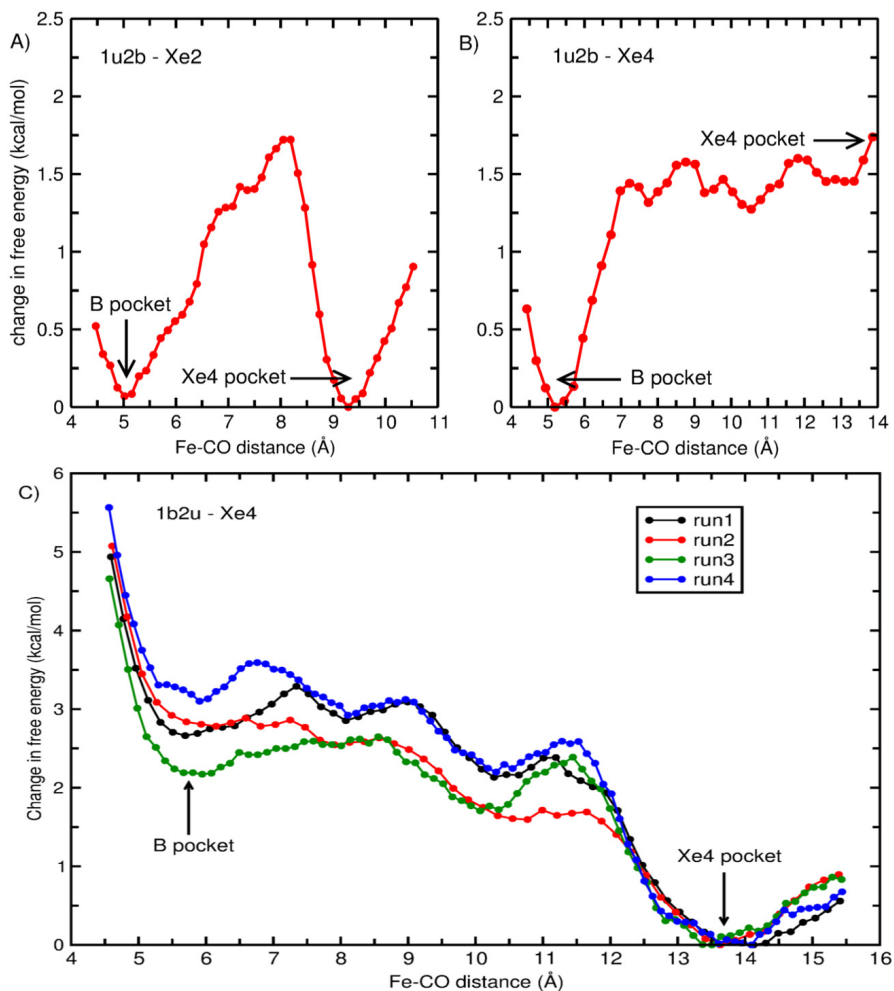


**Figure 5.16:** Free energy profile for migration of CO to Xe2 and Xe4 pockets in 1u2b and 1b2u systems. A)- free energy profile for migration of CO from distal pocket to Xe2 pocket in 1u2b and B)- free energy profile for migration of CO from distal to Xe4 pocket in 1u2b and C)- free energy profile for migration of CO to Xe4 in 1b2u system. Magenta and green color represent profile for CO migration without and with multipole, while black and blue represent the average profile.



### 5.3.4 Free energy simulations

To understand the energy landscape of CO migration in different Xe cavities, it was important to calculate the change in free energy associated with different migration pathway. This is computationally performed by umbrella sampling for the process of CO migration from distal pocket to Xe2 and Xe4 pocket. The free energy data from umbrella sampling are shown in Figure 5.16. From Figure 5.16b we can observe that barrier for Xe4 migration is high compare to Xe2 in 1u2b , while for 1b2u system the barrier for Xe4 cavity is low compare to distal pocket, which makes CO migration to Xe4 energetically favorable (Figure 5.16c). The same calculation is repeated by changing the seed number and with different initial structures. The energy profile looks exactly same, except for some energy refinements. The calculated value of free energy change suggests that the barrier height for CO migration changes from 3.0 kcal/mol in 1b2u to  $\approx 1.5$ -2.0 kcal/mol in 1u2b state. Although the free energy barrier itself doesn't account for the underlying mechanism for migration of CO, but it shows the presence of asymmetry in the energy landscape. This is quite surprising that the subunits in *Scapharca inaequivalvis* hemoglobin has different affinity for Xe pockets although they are identical. In order to make correlation between CO migration and protein dynamics we plotted the RMSD for each residues in different windows of the umbrella sampling. We have selected 4 windows which shows the average flexibility of protein residues for different locations of CO ligand within protein in Figure 5.17. From Figure 5.17 one can see that the RMSD of the protein individual residues is changing depending upon the location of CO ligand inside the protein. In Figure 5.17a it shows that helix E and F are rigid when CO is present in the distal pocket compared to other helices, however as CO migrates from distal pocket the helix E and F become more dynamic. Interestingly helix B which has the Leu36 residue which acts as gate for the distal pocket and other region inside the protein has increased RMSD compared to the initial stage which is indicative of the influence of CO movement on the individual residues (Figure 5.17b). Helix A, B and G line up to form Xe4 pocket and there RMSD values has increased compared to the initial stage when CO is present in Xe4 pocket (Figure 5.17c, d). From this analysis one can easily follow protein motion at different time and find the correlated moves coupled with the migration of ligand inside the protein. This provides time average local fluctuations mediated from one part of the protein to other.

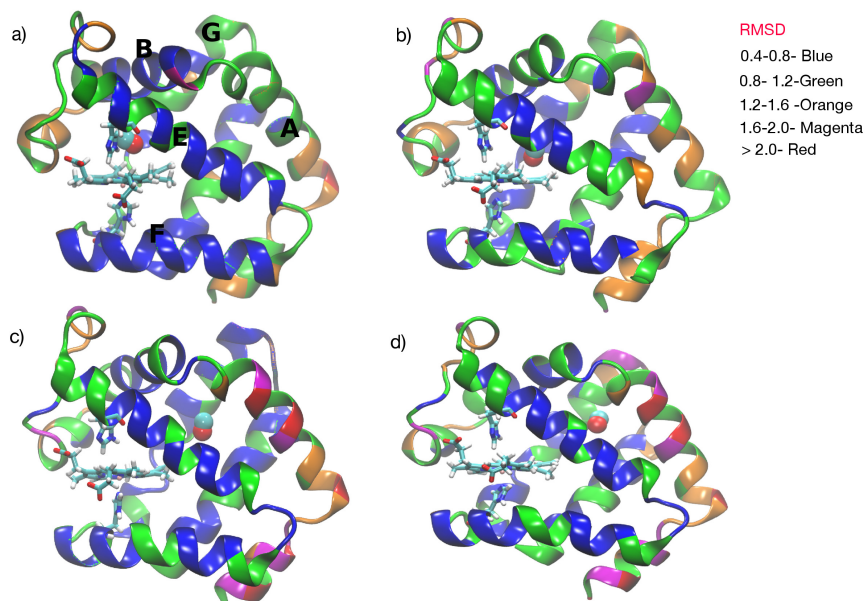


**Figure 5.17:** RMSD value of individual residues of protein in different umbrella windows which depends on the location of CO inside the protein. The different color coding for the RMSD value is shown in the figure.

## 5.4

## Conclusion

From the present molecular dynamics study we looked at structural and dynamical changes occurring inside and at the dimeric interface of the protein and correlate it to the migration behavior of CO ligand. Unlike Xe3 cavity found in myoglobin all other cavities are present in HbI, however their location are slightly different compared to myoglobin. Xe4 cavity is surrounded by A, B and G helices. Xe1 is filled by Phe97 side chain in deoxy state and Xe2 cavity lies in the heme plane. These pockets are known from high pressure Xe experiments. It had been observed from photolysis experiments that unbound CO resides in these pockets before geminate rebinding or diffusing to the solvent. From all the experimental and simulation studies till now not much information is known about the binding pockets and key residues responsible for CO migration within internal pockets. From our simulations qualitative information about the key residues responsible for CO migrations within these internal cavities, the pathway for CO migration into the solvent and dynamics of water at the interface are known. First time from the simulation studies

made so far, we have observed the flipping of Phe97 residue on the time scale of 80-100 ns, followed by the water inclusion at the interface, migration of CO in Xe cavities, which quantitatively shows the coupled dynamics of Phe97 flipping and water inclusion at the dimeric interface. The possible pathways for water insertion inside the protein at the distal pocket is observed in our simulations which quantitatively describe how the water molecule initially bound to the interfacial side of distal histidine moves inside the protein. These information are the signatures to quantify the deoxy and oxy state. However other structural transitions like change in the iron-iron distance and rotation of monomer subunits with respect to each other are not observed, which occur on the time scale of several  $\mu$ s known from experiments.

Observing the intermediate dynamic states of protein in which one subunit has unbound CO while the other is in oxidized or deoxidized states shows the presence of dynamical asymmetry regarding the time scale of CO migration observed in experiments by Royer et. al., inherent in the protein, although the protein has global  $C_2$  symmetry. This local asymmetry of individual monomer units is due to different behavior of residues as known for the Scapharca dimeric hemoglobin where major changes are observed inside the protein, unlike human hemoglobin. From the CO migration dynamics we can say that Xe4 is the most preferred site for occupation compare to other internal cavities (Xe2 and Xe1) as found in time-resolved crystallographic studies as well. One of the possible reason for higher occupancy of Xe4 compare to Xe2 is because distal pocket is directly connected to Xe4 through Leu36 gate, as well as it provides the direct route for CO to migrate into the solvent. In two of the above studied system (1b2u and 1u2e), we observed CO migrates to the solvent through Xe4 cavity which was predicted as the possible pathway (the BG pathway) from other previous computational analysis, however we can't neglect the possibility of minor pathway which is through G and H helices and exit at the dimeric interface. Few attempts has been made by CO to exit through G and H helix however it never exit through this minor route. The other important observation is that migration behavior of CO does not depend on the occupation states of the other heme subunit. Observations made by our simulations explicitly address many of the questions from the literature, and provides qualitative understanding mainly the coupled dynamics of Phe97 flipping and water inclusion at the dimeric interface, important residues responsible for CO migration and presence of water at the distal site in the deoxy state. Many of the other questions which where not addressed in the present work will be the motivation for the future study of the present system

for longer time scale in order to extract more quantitative understanding of the phenomenon occurring at the atomistic level to complement the experimental results.

## 5.5 Quaternary structural transition in HbA

Conformational changes in oligomeric proteins are related to their biological functionality. The change in the conformational state is mediated through several reasons, which includes ligand binding<sup>247-249</sup> or mutation of a residue.<sup>250-252</sup> This part of the chapter will discuss about the quaternary conformational change in Human hemoglobin. There are number of experimental studied on human hemoglobin based on thermodynamic data.<sup>253</sup> These data discuss properties like linkage between dimer and tetramer association<sup>254</sup> and oxygen binding,<sup>255,256</sup> the effects of pH<sup>257</sup> and chloride ion<sup>258,259</sup> on the dimer-tetramer reaction and properties of isolated chains, including their ligand binding. Based on the thermodynamic data by Ackers et. al.,<sup>260</sup> the deoxy state of hemoglobin is more stable than oxy state by 6.3 Kcal/mol. These data are largely derived from x-ray analysis. Recent simulation<sup>261-263</sup> studies by several groups has shown that structural transition in hemoglobin takes place within ns time scale. These results shows contradiction with experimental data based on thermodynamic.

## 5.6 Computational methods

The starting structure to perform the MD simulations were taken from the protein data bank (PDB). The X-ray structures with the PDB code 2DN2<sup>264</sup> and 2DN3<sup>264</sup> were taken for simulating the deoxy and oxy states. The protonation states of the histidines were evaluated by the program WHATIF,<sup>265</sup> which were different for the deoxy and oxy state. The protein was solvated with water and neutralized by adding the counter ions. The total number of atoms in the simulation for the deoxy state (2DN2) was 72081, having 20981 water molecules and 42 sodium ions ( $\text{Na}^+$ ) and 36 chloride ions ( $\text{Cl}^-$ ), while for oxy state (2DN3) the total number of atoms were 67610, having 19490 water molecules and 40 sodium ions ( $\text{Na}^+$ ) and 34 chloride ions ( $\text{Cl}^-$ ). There were other two systems prepared from 2DN3 structure with bound CO removed, one with heme in planar form (using the six coordinated heme potential) and other in which heme with domed structure as in five coordinated deoxy state using the five coordinated heme potential. These states with removed CO from 2DN3

are called as deoxy-6 and deoxy-5 states in our simulations. All the simulations were carried out with NAMD<sup>239</sup> package and with CHARMM force field using TIP3P water model. The energy of the system was minimized with conjugate gradient method by fixing the protein atoms and let the water and ions relax around the protein and then another minimization was done with no atoms fixed in the system. The entire system was heated up from 0 to 300 K at the intervals of 25 K, while the protein atoms were kept fixed. The whole system was then equilibrated for 250 ps, while removing the constraints on the protein atoms every 50 ps. After this the entire system was equilibrated for another 1 ns with no constraints on the system, except the constraint on water bonds which were kept fixed during the entire simulation. The electrostatic interactions were computed every fourth step with particle-mesh Ewald summation algorithm.<sup>266</sup> Short-range repulsive and attractive interactions were described by a Lennard-Jones potential with a cut-off of 12 Å. The MD simulations were carried out at constant temperature and pressure (NPT) of 300 K and 1 atm with a time step of 1 fs. Each simulation was performed for 100 ns till now.

---

## 5.7 Results

**2DN2** This PDB file represents the deoxy state of tetrameric hemoglobin (HbA) in which all the four monomer units are in the unbound state. Figure 5.18 contains data regarding the RMSD of the entire protein, RMSD of each monomer unit ( $\alpha_1$ ,  $\beta_1$ ,  $\alpha_2$ ,  $\beta_2$ ) and distance between C $\alpha$  carbon atoms of terminal histidine residues in the two  $\beta$  units, compared with the starting structure (2DN2) of the protein simulation. Figure 5.19a, b plots the distance between iron of the heme center and nitrogens of the distal histidine (NE2 and ND1). From Figure 5.19 it is clear that in one of the monomer units (P2), the distal histidine residue has more flexibility compare to other subunits in which the Fe and N distances fluctuates around the average value in the crystal structure (2DN2). Figure 5.19c shows the probability distribution of distance between Fe and center of mass (COM) of 4 nitrogens of porphyrin ring and Figure 5.19d shows the distance between Fe and the NE2 of the proximal histidine. Figure 5.19c clearly shows that in the deoxy state there is zero probability of iron to be in the plane of porphyrin ring.

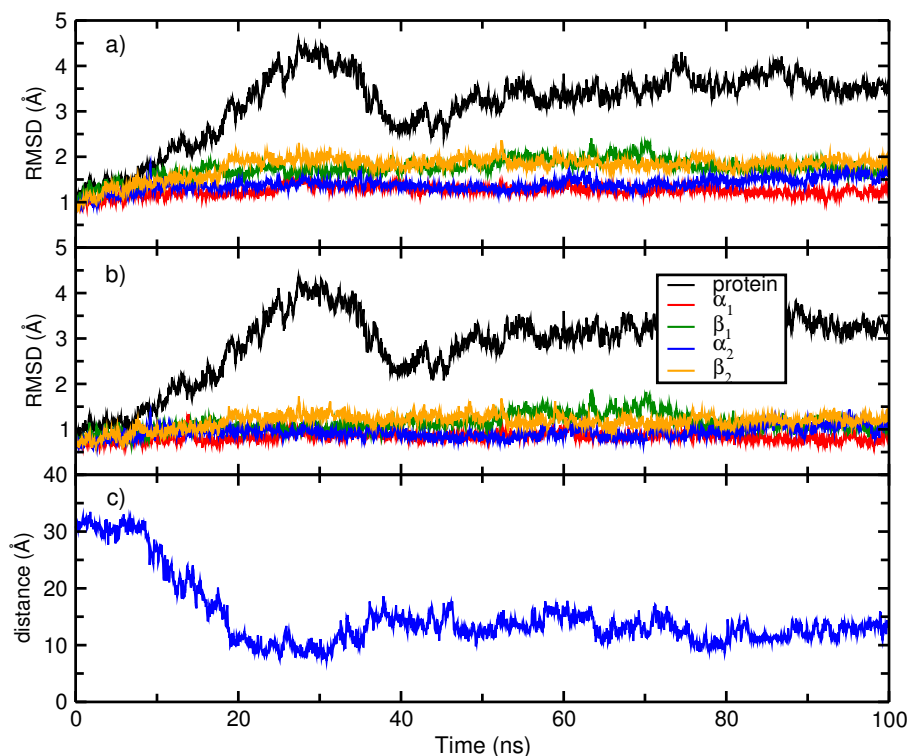


**Figure 5.18:** RMSD data for deoxy state (2DN2). a)- RMSD data is calculated by aligning each of the monomer units with their starting crystal structure considering *all atoms except hydrogens* b)- RMSD data is calculated by aligning each of the monomer units with their starting crystal structure considering only *backbone atoms* and c)- distance between  $C_\alpha$  atoms of 2 histidine residue present at the terminal of 2  $\beta$  chains.

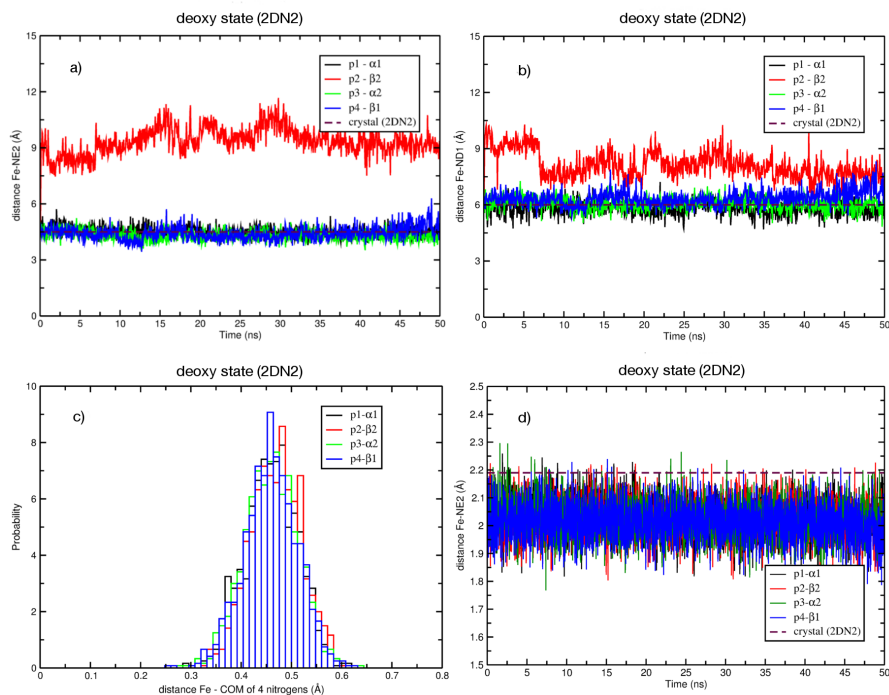


**Figure 5.19:** a)- shows the distance between Fe of heme and NE2 of the distal histidine and b) - shows the distance between Fe of heme and ND1 of the distal histidine in the deoxy state compared with the initial structure 2DN2. c) - It shows the probability distribution of the average distance between Fe and center of mass (COM) of 4 nitrogens of porphyrin ring in the deoxy state (2DN2) for all the four monomer units. d) - shows the distance between the nitrogen of proximal histidine (NE2) and Fe atom of heme.



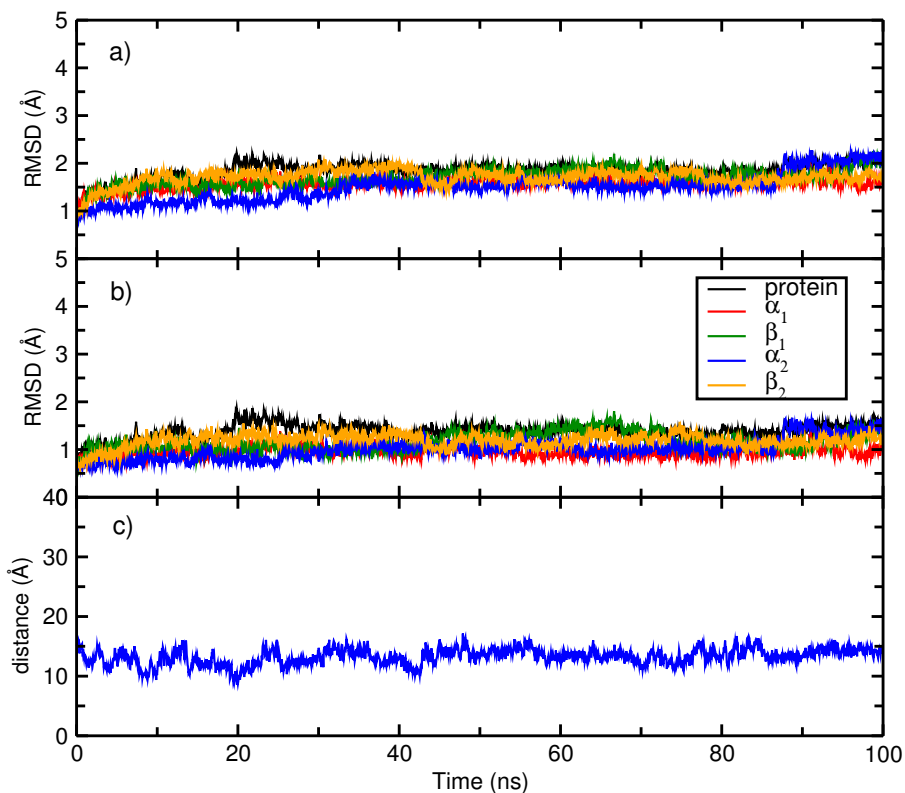


**Figure 5.20:** RMSD data for deoxy state (2DN3). a)- RMSD data is calculated by aligning each of the monomer units with their starting crystal structure considering *all atoms except hydrogens* b)- RMSD data is calculated by aligning each of the monomer units with their starting crystal structure considering only *backbone atoms* and c)- distance between  $C_{\alpha}$  atoms of 2 histidine residue present at the terminal of 2  $\beta$  chains.

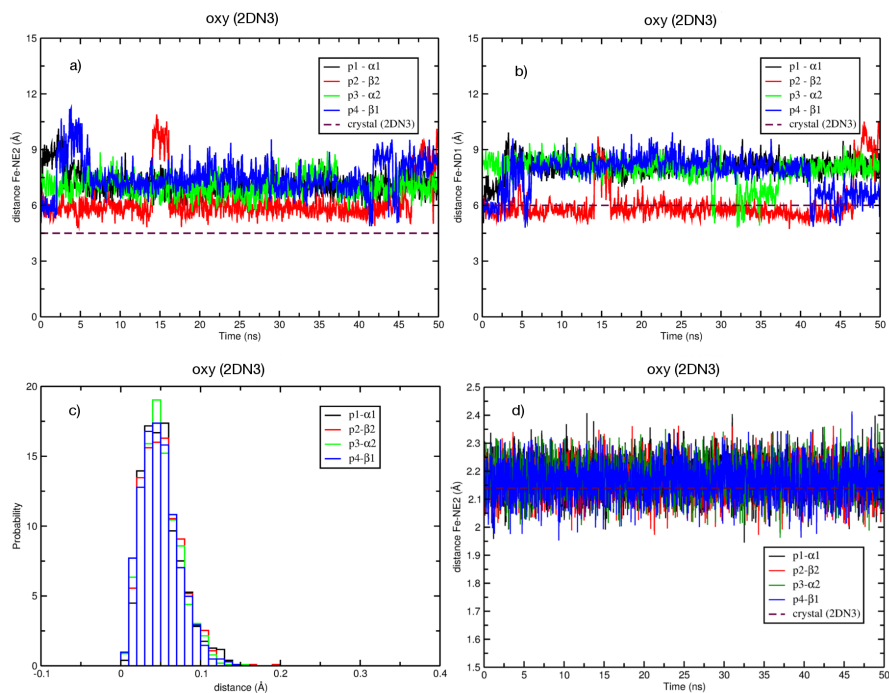


**Figure 5.21:** a)- shows the distance between Fe of heme and NE2 of the distal histidine and b) - shows the distance between Fe of heme and ND1 of the distal histidine in the deoxy state compared with the initial structure 2DN3. c)- It shows the probability distribution of the average distance between Fe and center of mass (COM) of 4 nitrogens of porphyrin ring in oxy state (2DN3) for all the four monomer units. d) - shows the distance between the nitrogen of proximal histidine (NE2) and Fe atom of heme.

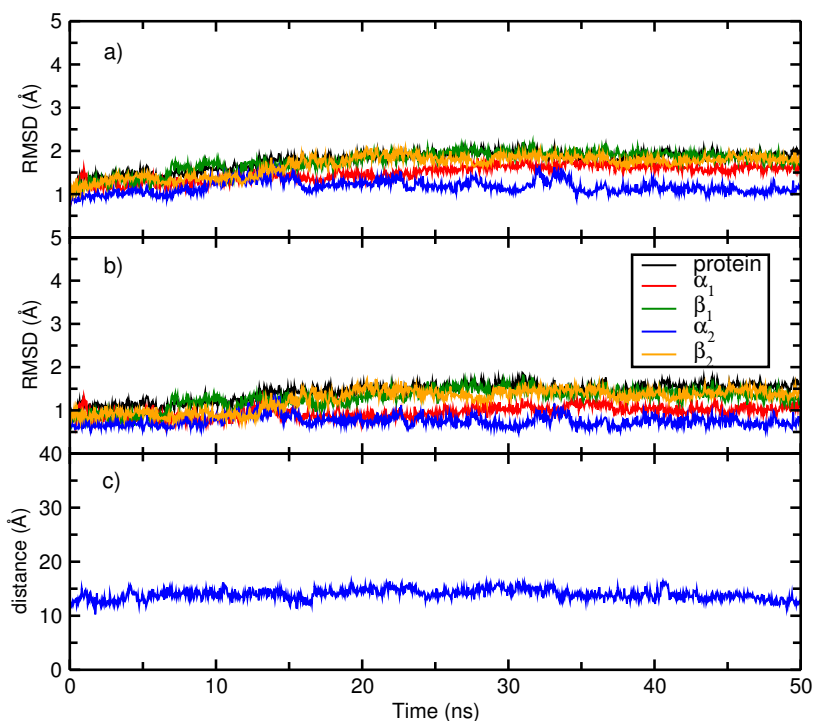


**Figure 5.22:** RMSD data for 2DN3 deoxy-6 protein (tetramer). a)- RMSD data is calculated by aligning each of the monomer units with their starting crystal structure considering *all atoms except hydrogens* b)- RMSD data is calculated by aligning each of the monomer units with their starting crystal structure considering only *backbone atoms* and c)- distance between  $C_{\alpha}$  atoms of 2 histidine residue present at the terminal of 2  $\beta$  chains. All these data are made in comparison with the starting structure (2DN3) in which CO was removed.

**2DN3** This PDB file represents the oxy state of the tetrameric hemoglobin in which all the four monomer units were oxygenated. Figure 5.20 contains data regarding the RMSD of the entire protein, RMSD of each monomers ( $\alpha_1$ ,  $\beta_1$ ,  $\alpha_2$ ,  $\beta_2$ ) and distance between  $C_{\alpha}$  carbon atoms of terminal histidine residues in the two  $\beta$  units, compared with the starting structure of the protein (2DN3). Figure 5.21 plots the distance between iron at the heme center and nitrogens of the distal histidine (NE2 and ND1). Figure 5.21c shows that probability distribution of distances between Fe and center of mass (COM) of 4 nitrogens of porphyrin ring in four monomer units and Figure 5.21d shows the distance between Fe and the nitrogen (NE2) of the proximal histidine. Figure 5.21c clearly shows that in the oxy state there is zero probability of iron moving out of the plane of porphyrin ring.

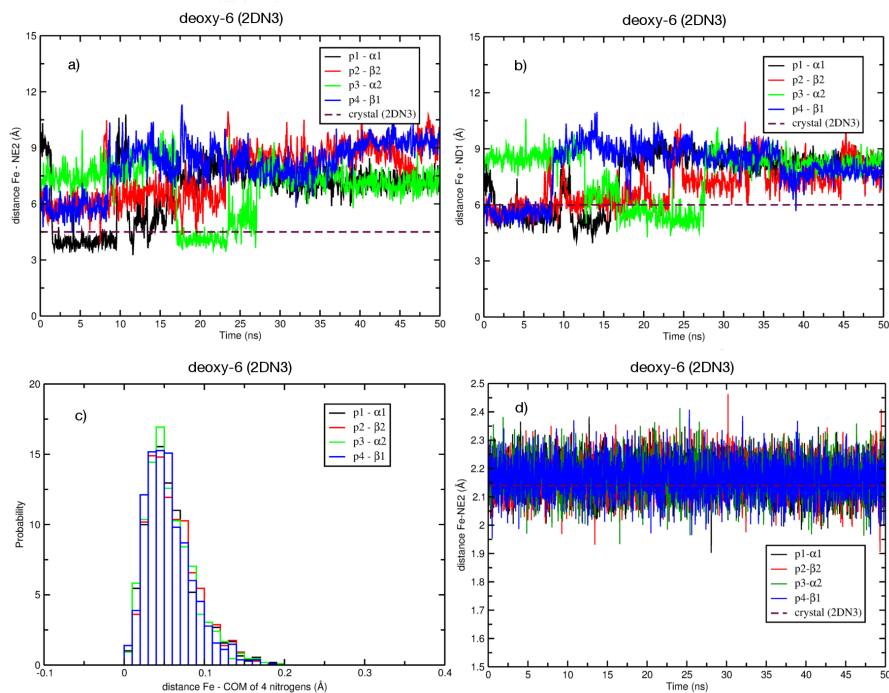


**Figure 5.23:** a)- shows the distance between Fe of heme and NE2 of the distal histidine and b) - shows the distance between Fe of heme and ND1 of the distal histidine in the deoxy state compared with the initial structure (2DN3 deoxy-6). c)- It shows the probability distribution of the average distance between Fe and center of mass (COM) of 4 nitrogens of porphyrin ring in oxy state (2DN3 deoxy-6) for all the four monomer units. b) - shows the distance between the nitrogen of proximal histidine (NE2) and Fe atom of heme.

**2DN3 deoxy-6** It represents the deoxy state of tetrameric hemoglobin in which all the four CO groups bound to the Fe is removed and the heme is made to be in planar form with six coordinated potential. Figure 5.22 contains data regarding the RMSD of the entire protein, RMSD of each monomers ( $\alpha_1, \beta_1, \alpha_2, \beta_2$ ) and distance between C $\alpha$  carbon atoms of histidine residues in the two  $\beta$  units, compared with the starting structure of the protein (2DN3) but with removed CO. Figure 5.23 plots the distance between iron at the heme center and nitrogens of the distal histidine (NE2 and ND1). Figure 5.23c shows that probability distribution of distances between Fe and center of mass (COM) of 4 nitrogens of porphyrin ring in four monomer units and Figure 5.23d shows the distance between Fe and the NE2 of the proximal histidine. Comparing this data with 2DN3 oxy state, we found that there is no substantial difference in the RMSD of entire protein or in the monomer units. Apart from this it seems that after removing the bound CO there is more space in the distal pocket which leads to more spacial freedom for distal histidine, which is clearly represented in increased distance between Fe and nitrogens of distal histidine as compared in Figure 5.21 and 5.23.

**2DN3 deoxy-5** It represents the deoxy state of tetrameric hemoglobin in which all the four CO groups bound to the Fe is removed and heme is made non-planar by applying five coordinated heme potential. Figure 5.24 contains data regarding the RMSD of the entire protein, RMSD of each monomers ( $\alpha_1, \beta_1, \alpha_2, \beta_2$ ) and distance between C $\alpha$  carbon atoms of terminal histidine residues in the two  $\beta$  units, compared with the starting structure of the protein (2DN3) but with removed CO. Figure 5.25 plots the distance between iron at the heme center and nitrogens of the distal histidine (NE2 and ND1). Figure 5.25a shows that probability distribution of distances between Fe and center of mass (COM) of 4 nitrogens of porphyrin ring in four monomer units and Figure 5.25b shows the distance between Fe and the NE2 of the proximal histidine. Comparing the data from the fully deoxygenated state 2DN2, there are substantial difference in the RMSD of entire protein or in the monomer units. Comparing the RMSD data from Figure 5.18 and 5.24 it seems that changing the potential from six coordinated heme to five coordinated heme the overall behavior of the protein (global structure) doesn't changes to complete deoxy state after 50 ns, apart from local changes in the distal pocket which is observed in the calculated distances between Fe and nitrogens of distal histidine in Figure 5.19 and 5.25.

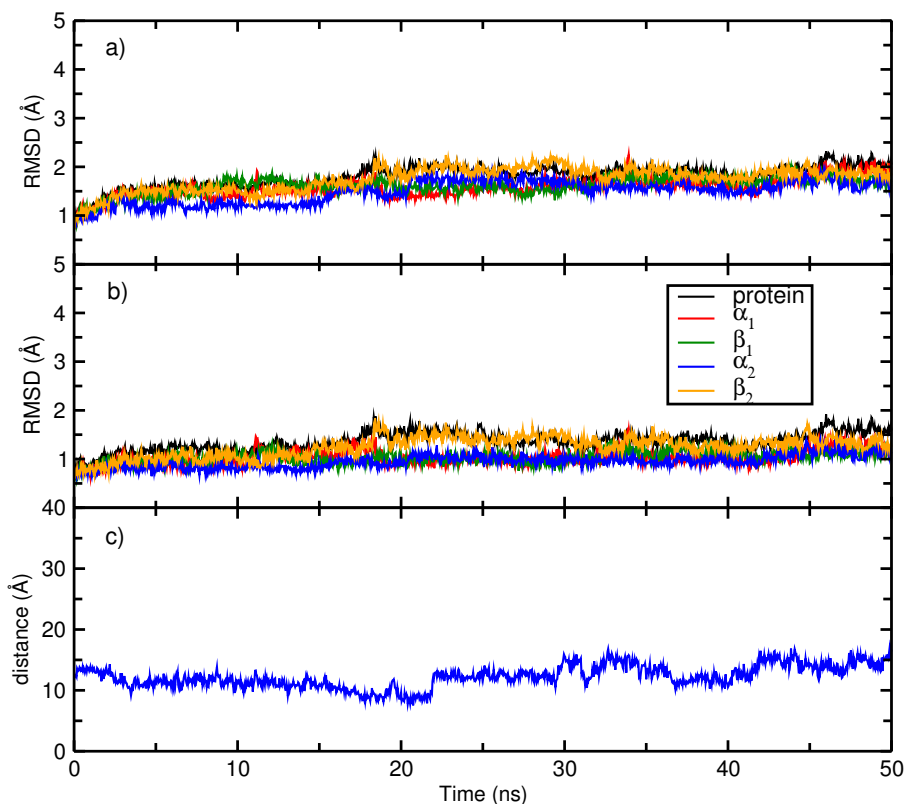


**Figure 5.24:** RMSD data for 2DN3 deoxy-5 protein (tetramer). a)- RMSD data is calculated by aligning each of the monomer units with their starting crystal structure considering *all atoms except hydrogens* b)- RMSD data is calculated by aligning each of the monomer units with their starting crystal structure considering only *backbone atoms* and c)- distance between  $C_{\alpha}$  atoms of 2 histidine residue present at the terminal of 2  $\beta$  chains. All these data are made in comparison with the starting structure in which CO was removed and the Fe was moved out of plane.

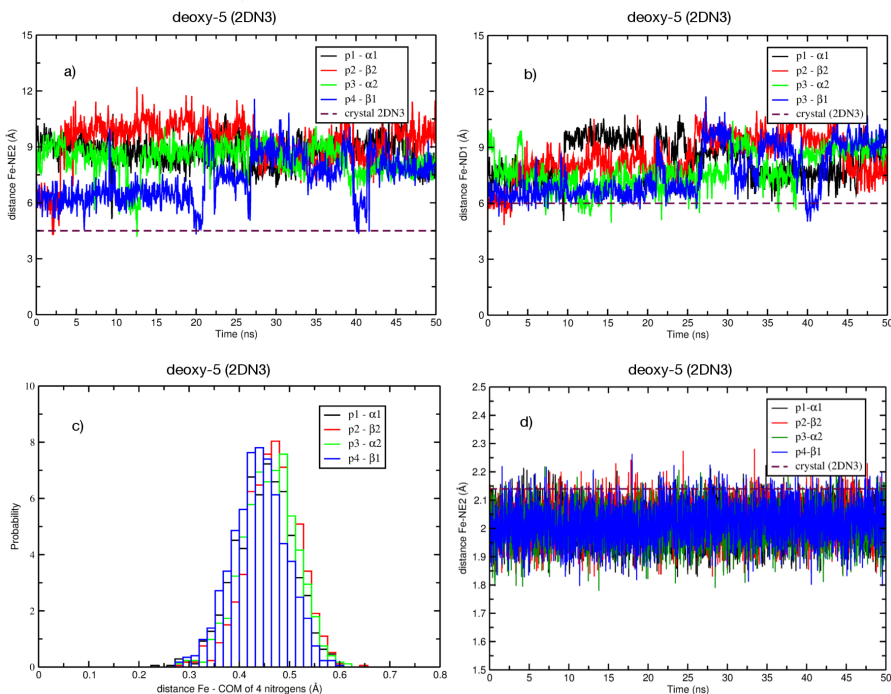


**Figure 5.25:** a)- shows the distance between Fe of heme and NE2 of the distal histidine and b) - shows the distance between Fe of heme and ND1 of the distal histidine in the deoxy state compared with the initial structure (2DN3, deoxy-5) in which CO was removed and Fe was moved out of plane. c)- It shows the probability distribution of the average distance between Fe and center of mass (COM) of 4 nitrogens of porphyrin ring in oxy state (2DN3 deoxy-5) for all the four monomer units. It shows that there is zero probability of Fe atom to move in the porphyrin plane. b) - shows the distance between the nitrogen of proximal histidine (NE2) and Fe atom of heme.

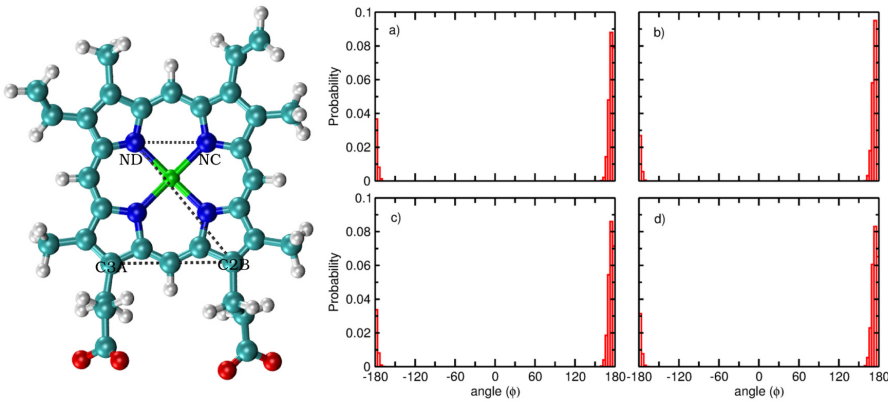


**Figure 5.26:** left)- It shows the dihedral angle formed by the atoms C3A, C2B, ND, NC of heme unit. right)- It shows the probability distribution of the dihedral angle formed by the atoms C3A, C2B, ND, NC of heme unit. a) - Probability distribution for 2ND2 (deoxy state) b) - Probability distribution for 2ND3 (oxy state) c) - Probability distribution for 2ND3 (deoxy-5 state) and d) - Probability distribution for 2ND3 (deoxy-6 state). These It shows the probability distribution of the dihedral angle formed by the atoms C3A, C2B, ND, NC of heme unit. These probability distributions show that heme unit maintain the planarity during the simulation.

**Rigidity of heme units** The overall planarity of heme units is also an important measure compare to in-plane movement of Fe during T to R transition. There are many ways of measuring the planarity of the whole heme units. We measure the dihedral angle formed by four atoms around the Fe atom of the heme unit. These atoms are shown in Figure 5.26. The probability distribution of these dihedral angles are shown in Figure 5.26 for all the 4 systems discussed above, which gives us an idea of the overall planarity of the heme units during the entire simulation time. These data show that these four atoms tend to maintain the planarity of the heme units in all the four studied system.

**Reason for high RMSD of deoxy state** From the RMSD of deoxy protein (2DN2) it seems that there is large structural changes (tertiary/quaternary), which leads to such high value of RMSD around 30 ns but the RMSD value at the 50 ns is lower in comparison to value at 30 ns 5.18. It is not understood, how much the rotation of one dimer with respect to the other contributes to the overall RMSD. Figure 5.27 shows comparison of starting structure and the structures at 30 and 50 ns. From Figure 5.27a and b (top), which shows the front and side view of the 30 ns structure superimposed on the initial structure (2DN2), we can see that there is rotation of the whole protein dimer



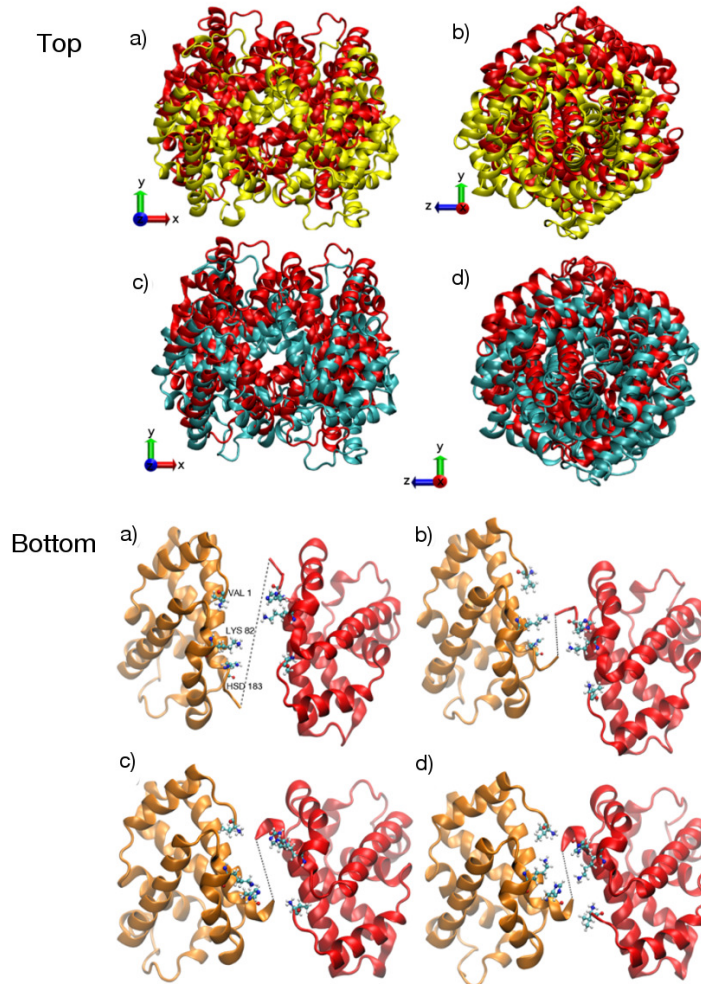


**Figure 5.27:** Color code: red - represent the initial crystal structure, yellow - represent the structure at 30 ns and grey - represent the structure at 50 ns. Top - represents the superimposed structure between initial structure (2DN2) and after simulation at 30 ns while bottom row - represents the superimposed structure between initial structure (2DN2) and after simulation at 50 ns. a) - shows the front view and b)- shows the side view of the superimposed structure after 30 ns. c) - shows the front and d) - shows the side view of the superimposed structure after 50 ns. Bottom- a)- represent the starting structure for deoxy state (2DN2), b) - structure after 30 ns. c)- represent the starting structure for oxy state (2DN3) and d)- structure after 30 ns.

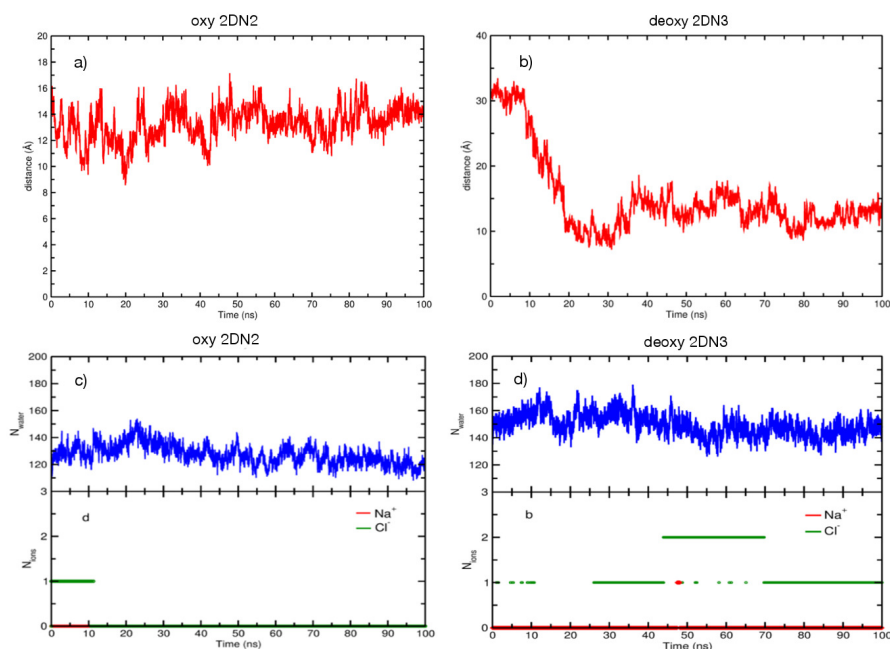


**Figure 5.28:** a)- RMSD of the deoxy state (2DN2) simulation for all protein heavy atoms relative to X-ray 2DN3 (reference) structure. b)- RMSD of the oxy state (2DN3) for all protein heavy atoms relative to X-ray 2DN2 (reference) structure. All protein heavy atoms were align to the reference structure. Time series for the change in the number of water molecules and ions ( $\text{Cl}^-$  or  $\text{Na}^+$ ) present at the interface formed by 4 subunits of protein. a)- number of water molecules in the deoxy state (2DN2), b)- number of ions in the deoxy state, c)- number of water molecules in the oxy state (2DN3) and d)- number of ions in the oxy state.

(quaternary structural change) with respect to other dimer. However, from Figure 5.27c and d (top), which is superimposed structure at 50 ns it is observed that after global rotation there is tight packing of the structure which leads to reduced value of RMSD compare to 30 ns structure. On measuring the rotation between the structure at 30 ns and initial structure, the overall rotation of the protein itself is around  $14^\circ$ , but the relative rotation of one dimer with respect to other is around  $4^\circ$ . This small rotation may contribute and give rise to higher RMSD value. The rotation angle is measured by the *CHIMERA* package. This small relative rotation observed in the simulation corresponds to more flexibility observed in deoxy state (T) compare to oxy state (R) as predicted in the published work done by Yusuff et. al.<sup>262</sup> recently.

**Dynamical comparison between the oxy and the deoxy state** DPG (2,3-diphosphoglycerate) is found in human red cells in approximately equimolar concentration to that of Hb. It regulates the oxygen transport by binding preferentially to deoxy Hb. This DPG binding site is located at the entrance of the central cavity with val 1, lysine 82 and histidine 143 of both  $\beta$ -chains. In the case of deoxy form (2DN2), this binding site has large structural change which is due to the rotation of  $\beta$ -chains relative to each other, shown in Figure 5.27. However large structural change is not observed in the oxy state (2DN3). Comparing the structure of deoxy state (2DN2) after 30 ns, Figure 5.27b (bottom) with the structure of the oxy state, Figure 5.27d (bottom), it can be observed that both the structures look similar. This implies that deoxy state is unstable in the absence of DPG. One way to observe this behavior is to plot the distance between C $\alpha$  atoms of the terminal histidine residue of  $\beta$ -chains, shown in Figure 5.28. Data in Figure 5.28b suggest that after the distance is reduced to 14 Å between two C $\alpha$  atoms, it fluctuates around this mean value. This distance is quite close to the value observed in the oxy state as shown in Figure 5.28a. The other observable is the number of water molecules ( $N_{\text{water}}$ ) or ions at the interface formed by 4 subunits of protein. This result is shown in Figure 5.28c, d. From Figure 5.28d we can observe that  $N_{\text{water}}$  in the deoxy system fluctuates around 140 and 2 Cl $^-$  ions are found at the interface as well, however in the starting structure for the deoxy state (2DN2) contains only 60 water molecules. This increase in the number of water molecules can be attributed to large structural changes observed in the deoxy state around  $\beta_1 - \beta_2$  interface where DPG binds. On contrary to this,  $N_{\text{water}}$  at the interface in the oxy state (2DN3), Figure 5.28c, fluctuates around 120, where the starting structure for oxy state contain 118 water molecules and there is no Cl $^-$  or Na $^+$  observed at the interface.

**5.8**Addition of chloride ions at  $\beta_1\beta_2$  interface

**Addition of 4 chloride ions:** Starting the simulations from the 2DN2 structure and intensely adding 4 chloride ions at the  $\beta_1\beta_2$  interface, to observe the effect of chloride ions at structural transition (T $\rightarrow$ R). These chloride ions were placed in the cavity where the DPG is found in T-state crystal structure. Initially the whole protein was constrained except the two helices lying at the  $\beta_1\beta_2$  interface, where chloride ions are placed, shown in Figure 5.29 (top) and simulations

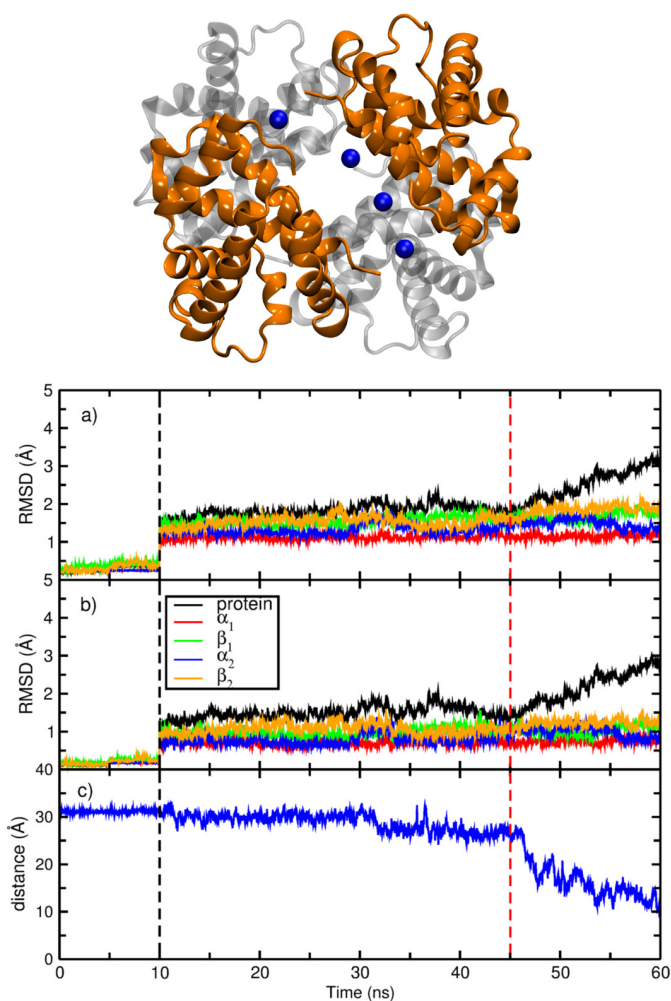


**Figure 5.29:** Starting structure for the protein simulations with 4 chloride ions present at the  $\beta_1\beta_2$  interface. 2  $\beta$  chains are shown in orange with 4 chloride ions in blue and 2  $\alpha$  units in transparent gray color. a)- RMSD data for deoxy state (2DN2), starting with 4 chloride ions at the  $\beta_1\beta_2$  interface where RMSD data is calculated by aligning each of the monomer units with their starting crystal structure, considering *all atoms except hydrogens*. b)- RMSD data for deoxy state (2DN2), same as a) above, but considering *only  $C\alpha$  atoms* for alignment. c)- distance between  $C\alpha$  atoms of 2 histidine residue present at the terminal of 2  $\beta$  chains. The dashed line shows the time scale for the constrained dynamics. The black dash line represent the time scale for constrained dynamics and red line represent the complete removal of chloride ions at the  $\beta_1\beta_2$  interface.

was run for 10 ns. After this we removed the constrain on the protein and run the simulations further upto 60 ns. The RMSD calculation from this simulation is shown in Figure 5.29 (bottom). From the RMSD data it is clear that after removing the constrain the RMSD value start increasing, however it is stable around 2-2.2 Å. RMSD data is shown considering all atoms except hydrogens and only for C $\alpha$  atoms in Figure 5.29a and Figure 5.29b. Once all the chloride ions are pushed out of the  $\beta_1\beta_2$  interface, which is around 45 ns in our simulations there is abrupt quaternary change in protein which is followed by measuring the distance between 2 terminal histidine residue present in 2  $\beta$  chains, shown in Figure 5.29 (top). From this simulations we can infer that presence of chloride ions at the interface slow down the structural transition. Snapshots of the presence of chloride ions at the  $\beta_1\beta_2$  interface at different time during the simulations is shown by there resid in Figure 5.30. As far as the chloride ions are present at the interface the structure of T-state is quite stable. In these snapshots important residues are highlighted (HSE:146, VAL:1 and LYS:82). These residues are part of  $\beta$  chains and are found interacting with chloride ions at the interface. The same residues interact with DPG (2,3 diphosphoglycerate), allosteric effector found at the interface of T-state crystal structure.

**Number of water molecules inside the protein:** The number of water molecules present inside the protein formed by 4 monomer units is shown in Figure 5.31. We can observe that as the constrained is removed the amount of water start increasing and reaches around 160 which start decreasing after the chloride ions start diffusing from the interface and due to structural transition the cavity at the interface becomes smaller and number of water decreases and saturates around 150.

**Addition of 2 chloride ions with the positional constraint:** In order to slow down the structural T $\rightarrow$ R transition we put a harmonic distance constraint between 2 chloride ions and interfacial residues like VAL1 and LYS82 on the two  $\beta$  units. The RMSD and the distance data for the terminal HSE C $\alpha$  atoms for 60 ns simulations are shown in Figure 5.32. From the simulation result we can observe that after 50 ns the protein start to have structural transition and by the end of 60 ns it is more close to the R structure.

**Comparison between chloride ions and DPG:** We observe that chloride ions at the interface provide some stability to the T-state structure compare to bare

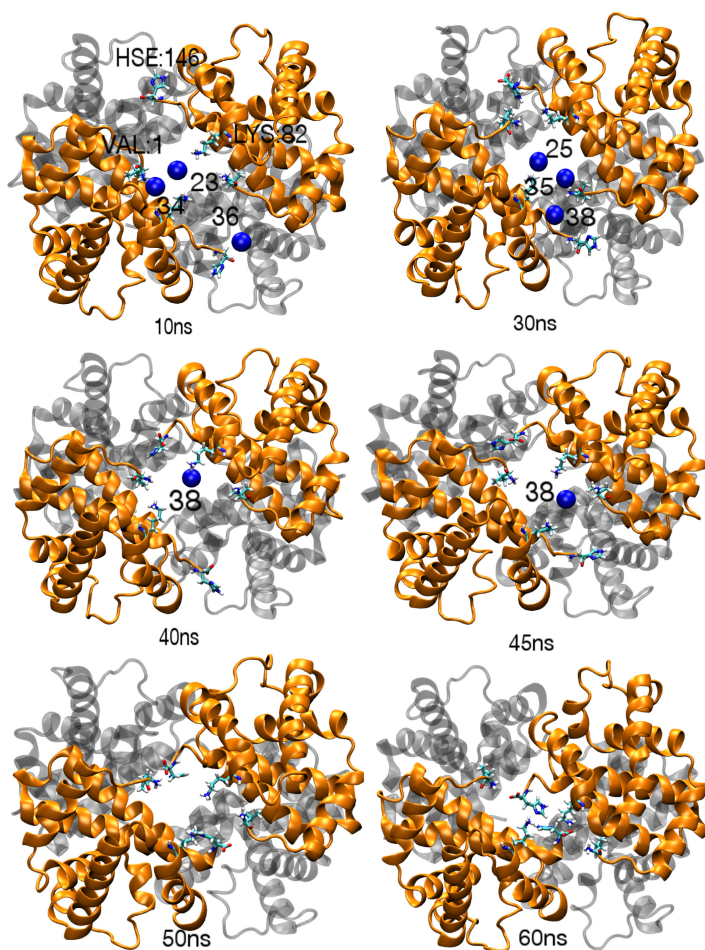


**Figure 5.30:** Snapshots for whole protein monomer units and chloride ions (blue) at the  $\beta_1\beta_2$  interface.  $\beta_1\beta_2$  units are shown in orange while  $\alpha_1\alpha_2$  in transparent gray color. Time scale for the snapshots are written below the figures and important residues (HSE:146, VAL:1 and LYS:82) interacting with ions are shown in Licorise representation.

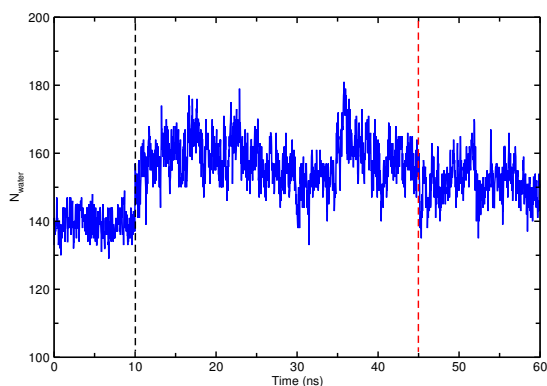


**Figure 5.31:** Number of water molecules present inside the protein. The change in the number of water molecules is due to changes occurring at the interface due to diffusion of chloride ions in solvent followed by the structural changes.

interface having no chloride ions. On adding more chloride ions (8 in number) at the interface, due to strong electrostatic repulsion they diffuse out quickly and were not stable. Comparing with DPG having 10 oxygens, out of which 8 oxygens are part of phosphate groups and 2 of acidic group, is a large molecule compare to chloride ions. Large size of DPG with more electronegative atoms provide more interacting sites at the interface compare to chloride ions and fits well into the cavity. In order to put more chloride ions at the interface, close to residues as in case of DPG, one can reduce the charge of chloride ions from  $-1e$  which would reduce the electrostatic repulsion and have more interaction which can bind the  $\beta$  units together stronger than 4 chloride ions. One can understand that due to less number of chloride ions/less interactions the size of the cavity gets larger which allow more water diffusion through the interface which can easily replace chloride ions as appeared in our simulations.

### 5.8.1 Reducing the force constant (k) between Fe and N

**Reduction by 10%:** This simulation setup was prepared exactly as the deoxy state simulation with the only difference that force constant for the Fe-N (nitrogen of porphyrin ring) bond was reduced by 10%. This was done to look at the possibility that weakening the bond at the center of the monomer unit will slow down the global structural changes, however it appears from the simulations result that reducing the force constant for Fe-N bond doesn't have

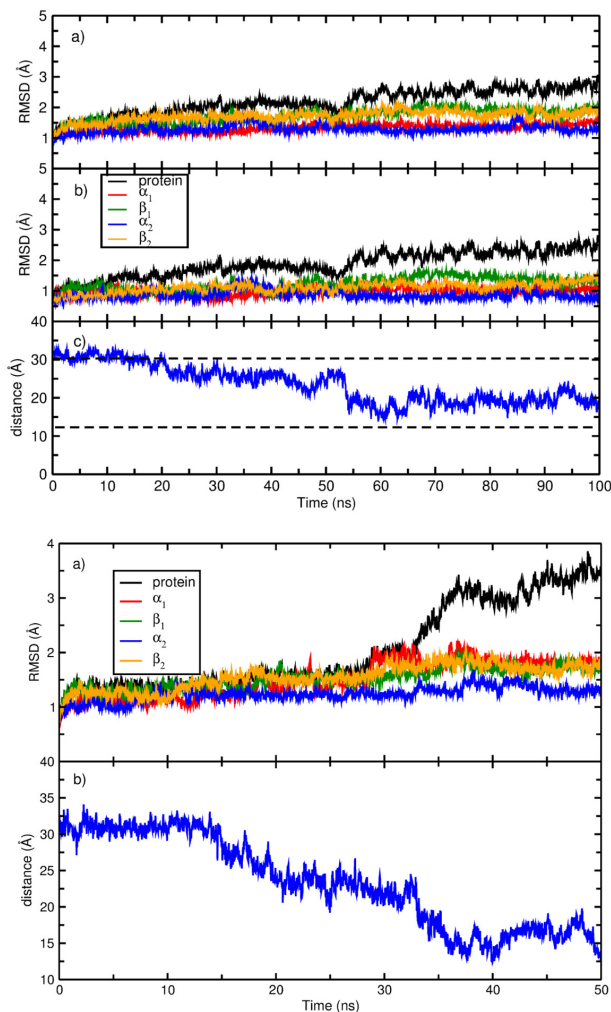


**Figure 5.32:** Top- a)- RMSD data for deoxy state (2DN2), starting with 2 chloride ions with harmonic constraint at the  $\beta_1\beta_2$  interface where RMSD data is calculated by aligning each of the monomer units with their starting crystal structure, considering *all atoms except hydrogens*. b)- RMSD data for deoxy state (2DN2), same as a) above, but considering *only backbone atoms* for alignment. c)- distance between  $C_\alpha$  atoms of 2 histidine residue present at the terminal of 2  $\beta$  chains. The dash lines in the figure corresponds to the distance found in the crystal structure of R (which is 30 Å) and T (which is 12 Å) state. Bottom- a)- RMSD data for deoxy state (2DN2), with reduced force constant for Fe-N (nitrogen of porphyrin ring) bond. RMSD data is calculated by aligning each of the monomer units with their starting crystal structure. b)- distance between  $C_\alpha$  atoms of 2 histidine residue present at the terminal of 2  $\beta$  chains.



much effect on the structural transition. The RMSD data and the distance between  $C_\alpha$  atoms of histidine residues are shown in Figure 5.32 (bottom).

**Reduction by a factor of 10:** This simulation setup was prepared exactly as the deoxy state simulation with the only difference that force constant for the Fe-N (nitrogen of porphyrin ring) bond was reduced by a factor of 10 (from 272.2 to 27.2 kcal/mol/Å<sup>2</sup>). This was done to look at the possibility that weakening the bond at the center of the monomer unit will slow down the global structural changes, however it appears from the simulations result that reducing the force constant for Fe-N bond slow down the structural transition. From the RMSD data (not shown here), it is evident that the protein structural transition has frozen upto 60 ns. After 60 ns the structural transition begins and distance between two terminal histidines starts to decrease.

**Reduction by a factor of 10 and having additional harmonic distance constraint of 2 chloride ions:** This simulation was performed to observe the combined effect of the presence of chloride ions as well as reduced force constant for the Fe-N bond. The RMSD and the distance data (not shown here), suggest the stability of the structure upto 75 ns. The stability of T state structure is maintained upto 50 ns and after that structural change starts to take place however the the two end of the histidine residues don't completely collapse as in case of 2DN2 structure due to the presence of chloride ions.

## 5.9 2DN2 state in the presence of 2,3-DPG

As pointed out in the article by Benesch et. al.<sup>267</sup> that DPG bind deoxy-hemoglobin in a ratio of one mole of DPG per mole of tetramer hemoglobin and energy required to dissociate DPG from tetramer-DPG complex is 6.4 Kcal/mol, same energy difference found between T and R state structure. In order to the look at the dynamics of 2DN2 state of protein in the presence of DPG we perform the simulation with DPG at the  $\beta_1$ - $\beta_2$  interface with harmonic constraint to stay close to the interfacial residue. However, this constraint was not enough strong after 40 ns. Later, we completely fix the phosphate group and then further run the dynamics upto 100 ns. The RMSD data for 2DN2+DPG is shown in Figure 5.33. From Figure 5.33 one can observe that

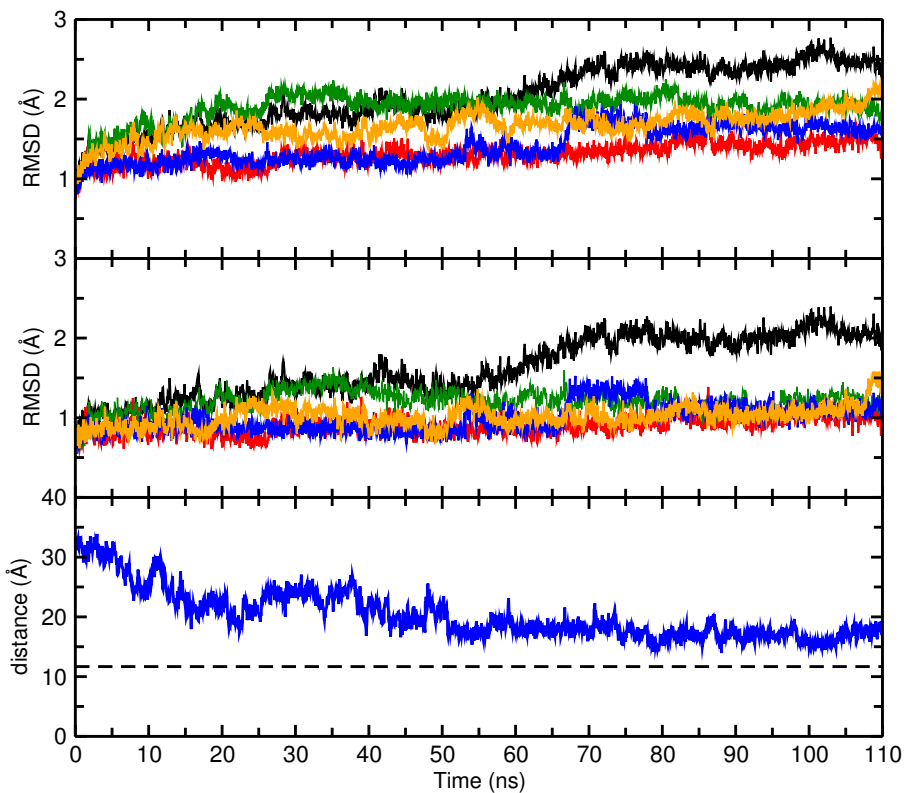


**Figure 5.33:** a)- RMSD data for deoxy state (2DN2), with DPG present at the interface. RMSD data is calculated by aligning each of the monomer units with their starting crystal structure considering *all atoms except hydrogens* b)- RMSD data by aligning each of the monomer units with their starting crystal structure considering only *backbone atoms*. c)- distance between  $C_{\alpha}$  atoms of 2 histidine residue present at the terminal of 2  $\beta$  chains.

the distance between 2  $C_\alpha$  of terminal histidine residues decays to 20 Å within 50 ns and after that it fluctuates between 16 and 20 Å till 110 ns. Even with the presence of DPG at the interface we found that T state has a tendency to move towards R state however it doesn't completely collapse to R due to the presence of DPG at the interface which block the movement of terminal histidine towards each other as in R state.

## 5.10 Outlook

From these new simulations with additional structural constraints on the 2DN2 state provide insight into parameters which can tune the stability of the T state however these parameters can't hold the system completely to T state. So far we have looking into the protein through thermodynamic point of view but one can also consider the kinetics of the whole process. As pointed out by W. A. Eaton et. al.<sup>268</sup> the transition state of T  $\rightarrow$  R conversion has more R like features. It may be possible that the barrier for T  $\rightarrow$  R conversion is small compare to R  $\rightarrow$  T. From the previous work of Hub et. al.<sup>261</sup> they have tried different structural constraints like us except trying with chloride ions at the interface or reduction in the force constant value of Fe-N bonds. From their work one can see that with constraint on all the salt bridges present in the system T state is stable upto 200 ns with this constraint dynamics and when they remove this constraint the system collapse completely to R state.



# BIBLIOGRAPHY

---

- [1] R. T. Hall and J. M. Dowling. Pure rotational spectrum of water vapor. *J. Chem. Phys.*, 47(7):2454–2461, 1967.
- [2] M. Falk and T. A. Ford. Infrared spectrum and structure of liquid water. *Canadian Journal of Chemistry*, 44(14):1699–1707, 1966.
- [3] F. Franks. *A matrix of life*. Royal Society of Chemistry, Cambridge, 2000.
- [4] L. W. Dahl and H. C. Andersen. A theory of the anomalous thermodynamic properties of liquid water. *J. Chem. Phys.*, 78(4):1980–1993, 1983.
- [5] S. I. Mamatkulov, P. K. Khabibullaev, and R. R. Netz. Water at Hydrophobic Substrates: Curvature, Pressure, and Temperature Effects. *Langmuir*, 20(11):4756–4763, 2004.
- [6] David Chandler. Interfaces and the driving force of hydrophobic assembly. *Nature*, 437(7059):640–647, 2005.
- [7] R. Francis, P. Chakrabarti R. P. Bahadur, and Joël Janin. Hydration of protein-protein interfaces. *Proteins*, 60(1):36–45, 2005.
- [8] L Lo Conte, C. Chothia, and J. Janin. The atomic structure of protein-protein recognition sites. *J. Mol. Biol.*, 285(5):2177–2198, 1999.
- [9] Sunil K. Panigrahi and Gautam R. Desiraju. Strong and weak hydrogen bonds in the protein-ligand interface. *Proteins*, 67(1):128–141, 2007.
- [10] C. K. Reddy, A. Das, and B. Jayaram. Do water molecules mediate protein-DNA recognition? *J. Mol. Biol.*, 314(3):619–632, 2001.
- [11] Y. Maruyama and Y. Harano. Does water drive protein folding? *Chemical Physics Letters*, 581:85–90, 2013.
- [12] L. Zhang, L. Wang, Y. T. Kao, W. Qiu, Y. Yang, O. Okobiah, and D. Zhong. From the Cover: Mapping hydration dynamics around a protein surface. *Proc. Nat. Acad. Sci. USA*, 104(47):18461–18466, 2007.
- [13] M. Chaplin. Do we underestimate the importance of water in cell biology? *Nature reviews.*, 7(11):861–866, 2006.
- [14] F. Franks. Protein stability: the value of 'old literature'. *Biophys. Chem.*, 96(2-3):117–127, 2002.
- [15] D. M. Leitner, M. Gruebele, and M. Havenith. Solvation dynamics of biomolecules: modeling and terahertz experiments. *HFSP J.*, 2(6):314–323, 2008.
- [16] D. Zhonga, S. K. Pal, and A. H. Zewail. Biological water: A critique. *Chem. Phys. Lett.*, 503(1-3):1–11, 2011.
- [17] W. E. Royer, A. Pardanani, Q. H. Gibson, E. S. Peterson, and J. M. Friedman. Ordered water molecules as key allosteric mediators in a cooperative dimeric hemoglobin. *Proc. Nat. Acad. Sci. USA*, 93(25):14526–14531, 1996.

- [18] J. L. Junta and M. F. Hochella. Manganese (ii) oxidation at mineral surfaces: A microscopic and spectroscopic study. *Geochim. Cosmochim. Acta.*, 58:4985–4999, 1994.
- [19] M. R. Kriegman-King and M. Reinhard. Transformation of carbon tetrachloride in the presence of sulfide, biotite, and vermiculite. *Environ. Sci. Technol.*, 26:2198–2206, 1992.
- [20] M. R. Kriegman-King and M. Reinhard. Transformation of carbon tetrachloride by pyrite in aqueous solution. *Environ. Sci. Technol.*, 28:692–700, 1994.
- [21] A. T. Stone. *Geochemical Processes at Mineral Surfaces*. ACS Symposium Series 323. American Chemical Society, Washington DC, 1986.
- [22] G. L. Richmond. Molecular bonding and interactions at aqueous surfaces as probed by vibrational sum frequency spectroscopy. *Chemical Reviews*, 102(8):2693–2724, 2002.
- [23] Y. R. Shen and V. Ostroverkhov. Sum-Frequency Vibrational Spectroscopy on Water Interfaces: Polar Orientation of Water Molecules at Interfaces. *Chemical Reviews*, 106(4):1140–1154, 2006.
- [24] P. Jungwirth and D. J. Tobias. Specific ion effects at the air/water interface. *Chemical Reviews*, 106(4):1259–1281, 2006.
- [25] C. J. Mundy and I-Feng W. Kuo. First-principles approaches to the structure and reactivity of atmospherically relevant aqueous interfaces. *Chemical Reviews*, 106(4):1282–1304, 2006.
- [26] Tsun-Mei Chang and L. X. Dang. Recent advances in molecular simulations of ion solvation at liquid interfaces. *Chemical Reviews*, 106(4):1305–1322, 2006.
- [27] W. Kauzmann. Thermodynamics of unfolding. *Nature*, 325(6107):763–764, 1987.
- [28] W. Kauzmann, K. Moore, and D. Schultz. Protein densities from x-ray crystallographic coordinates. *Nature*, 248(5447):447–449, 1974.
- [29] F. M. Richards. The interpretation of protein structures: Total volume, group volume distributions and packing density. *Journal of Molecular Biology*, 82(1):1–14, 1974.
- [30] F. M. Richards. Areas, volumes, packing, and protein structure. *Annual Review of Biophys. and Bioeng.*, 6(1):151–176, 1977.
- [31] Sergey M. Melnikov, A. Hoitzel, Andreas Seidel-Morgenstern, and Ulrich Tallarek. Influence of Residual Silanol Groups on Solvent and Ion Distribution at a Chemically Modified Silica Surface. *J. Phys. Chem. C*, 113(21):9230–9238, 2009.
- [32] P. K. Gupta and M. Meuwly. Dynamics of water/methanol mixtures at functionalized chromatographic interfaces. *J. Phys. Chem. B*, 116(35):10951–9, 2012.
- [33] M. Orzechowski and M. Meuwly. Dynamics of water filaments in disordered environments. *J. Phys. Chem. B*, 114(38):12203–12212, 2010.
- [34] J. Braun, A. Fouqueau, Raymond J. Bemish, and M. Meuwly. Solvent structures of mixed water/acetonitrile mixtures at chromatographic interfaces from computer simulations. *Phys. Chem. Chem. Phys.*, 10(32):4765–4777, 2008.

- [35] J. L. Rafferty, J. Ilja Siepmann, and M. R. Schure. Molecular-level comparison of alkylsilane and polar-embedded reversed-phase liquid chromatography systems. *Anal. Chem.*, 80(16):6214–6221, 2008.
- [36] J. van de Loosdrecht, A. M. van der Kraan, A. J. van Dillen, and J. W. Geus. Metal-support interaction: Titania-supported and silica-supported nickel catalysts. *Journal of Catalysis*, 170(2):217 – 226, 1997.
- [37] D. W. Goodman, A. K. Santra, and B. K. Min. Understanding silica-supported metal catalysts: Pd/silica as a case study. *Catalysis Today*, 85:113–224, 2003.
- [38] R. K. Iler. *The Chemistry of Silica: Solubility, Polymerization, Colloid and Surface Properties and Biochemistry of Silica*. A Wiley-Interscience publication, 1979.
- [39] S. P. Zhdanov, L. S. Kosheleva, and T. I. Titova. Ir study of hydroxylated silica. *Langmuir*, 3(6):960–967, 1987.
- [40] L. Zhang, S. Singh, Chuanshan Tian, Y. R. Shen, Yan Wu, Mark A. Shannon, and C. Jeffery Brinker. Nanoporous silica-water interfaces studied by sum-frequency vibrational spectroscopy. *J. Chem. Phys.*, 130(15):154702, 2009.
- [41] J. J. Yang, S. Meng, L. F. Xu, and E. G. Wang. Water adsorption on hydroxylated silica surfaces studied using the density functional theory. *Phys. Rev. B*, 71:12, 2005.
- [42] S. Leonardelli, L. Facchini, C. Fretigny, P. Tougne, and A. P. Legrand. Silicon-29 nmr study of silica. *J. Am. Chem. Soc.*, 114(16):6412–6418, 1992.
- [43] A. Tuel, H. Hommel, A. P. Legrand, and E. S. Kovats. A silicon-29 nmr study of the silanol population at the surface of derivatized silica. *Langmuir*, 6(4):770–775, 1990.
- [44] G. E. Maciel and D. W. Sindorf. Silicon-29 nmr study of the surface of silica gel by cross polarization and magic-angle spinning. *J. Am. Chem. Soc.*, 102(25):7606–7607, 1980.
- [45] L. Lichtenstein, C. Buchner, B. Yang, S. Shaikhutdinov, M. Heyde, M. Sierka, R. Włodarczyk, J. Sauer, and H. J. Freund. The atomic structure of a metal-supported vitreous thin silica film. *Angew. Chem. Int. Ed.*, 51(2):404–407, 2012.
- [46] A. Pedone, G. Malavasi, M. C. Menziani, U. Segre, F. Musso, M. Corno, B. Civalleri, and P. Ugliengo. Ffsioh: a new force field for silica polymorphs and their hydroxylated surfaces based on periodic b3lyp calculations. *Chemistry of Materials*, 20(7):2522–2531, 2008.
- [47] Garofalini S. H. Molecular dynamics computer simulations of silica surface structure and adsorption of water molecules. *Journal of Non-Crystalline Solids*, 120(1–3):1–12, 1990.
- [48] T. S. Mahadevan and S. H. Garofalini. Dissociative chemisorption of water onto silica surfaces and formation of hydronium ions. *J. Phys. Chem. C*, 112(5):1507–1515, 2008.
- [49] A. A. Hassanali and S. J. Singer. Model for the Water-Amorphous Silica Interface: The Undissociated Surface. *J. Phys. Chem. B*, 111(38):11181–11193, 2007.
- [50] A. A. Hassanali and S. J. Singer. Static and dynamic properties of the water/amorphous silica interface: a model for the undissociated surface. *Journal of Computer-Aided Materials Design*, 14(1):53–63, 2007.

- [51] Jincheng Du and Alastair N. Cormack. Molecular dynamics simulation of the structure and hydroxylation of silica glass surfaces. *Journal of the American Ceramic Society*, 88(9):2532–2539, 2005.
- [52] S. Tsuneyuki, M. Tsukada, H. Aoki, and Y. Matsui. First-principles interatomic potential of silica applied to molecular dynamics. *Phys. Rev. Lett.*, 61:869–872, 1988.
- [53] B. W. H. van Beest, G. J. Kramer, and R. A. van Santen. Force fields for silicas and aluminophosphates based on ab initio calculations. *Phys. Rev. Lett.*, 64:1955–1958, 1990.
- [54] I. Li, J. Bandara, and M. J. Shultz. Time evolution studies of the h2o/quartz interface using sum frequency generation, atomic force microscopy, and molecular dynamics. *Langmuir*, 20(24):10474–10480, 2004.
- [55] Nora H. de Leeuw, F. M. Higgins, and S. C. Parker. Modeling the surface structure and stability of  $\alpha$ -quartz. *J. Phys. Chem. B*, 103(8):1270–1277, 1999.
- [56] Z. Du and N. H. de Leeuw. Molecular dynamics simulations of hydration, dissolution and nucleation processes at the [small alpha]-quartz (0001) surface in liquid water. *Dalton Trans.*, pages 2623–2634, 2006.
- [57] M. C. F. Wander and A. E. Clark. Structural and dielectric properties of quartz-water interfaces. *J. Phys. Chem. C*, 112(50):19986–19994, 2008.
- [58] D. Argyris, D. R. Cole, and A. Striolo. Dynamic behavior of interfacial water at the silica surface. *J. Phys. Chem. C*, 113(45):19591–19600, 2009.
- [59] D. Argyris, D. R. Cole, and A. Striolo. Hydration structure on crystalline silica substrates. *Langmuir*, 25(14):8025–8035, 2009.
- [60] M. Sulpizi, Marie-Pierre Gaigeot, and M. Sprik. The silica-water interface: How the silanols determine the surface acidity and modulate the water properties. *J. Chem. Theory. Comput.*, 8:1037–1047, 2012.
- [61] M. Henderson. The interaction of water with solid surfaces: fundamental aspects revisited. *Surface Science Reports*, 46(1-8):1–308, 2002.
- [62] Ilan Benjamin. Hydrogen bond dynamics at water/organic liquid interfaces. *J. Phys. Chem. B*, 109(28):13711–13715, 2005.
- [63] J. Carrasco, A. Hodgson, and A. Michaelides. A molecular perspective of water at metal interfaces. *Nature Materials*, 11(8):667–674, 2012.
- [64] Y. I. Jhon, H. G. Kim, and M. S. Jhon. The structure of water near platinum and its significance in water-adsorbent system: molecular dynamics study. *Journal of Colloid and Interface Science*, 260(1):9–18, 2003.
- [65] Lawrence F. Scatena and Geraldine L. Richmond. Orientation, Hydrogen Bonding, and Penetration of Water at the Organic/Water Interface. *J. Phys. Chem. B*, 105(45):11240–11250, 2001.
- [66] J. Raul Grigera, Susana G. Kalko, and Jorge Fischbarg. Wall-Water Interface. A Molecular Dynamics Study†. *Langmuir*, 12(1):154–158, 1996.



- [67] A. Morita and J. T. Hynes. Hydrogen bonding strength of interfacial water determined with surface sum-frequency generation. *Chem. Phys. Lett.*, 470(1-3):7–12, 2009.
- [68] P. Ball. Life's matrix: water in the cell. *Cellular and molecular biology*, 47(5):717–720, 2001.
- [69] R. K. Murarka M. E. Johnson, C. Malardier-Jugroot and T. Head-Gordon. Hydration water dynamics near biological interfaces. *J. Phys. Chem. B*, 113(13):4082–4092, 2009.
- [70] M. J. Higgins, M. Polcik, T. Fukuma, J. E. Sader, Y. Nakayama, and Suzanne P. Jarvis. Structured water layers adjacent to biological membranes. *Biophys. J.*, 91(7):2532–2542, 2006.
- [71] Philip Ball. Water as an active constituent in cell biology. *Chem Rev*, 108(1):74–108, 2008.
- [72] K. Dill, T. Truskett, and V. Vlachy. Modeling water, the hydrophobic effect, and ion solvation. *Annu. Rev. Biophys. Biomol. Struct.*, 2005.
- [73] L. D. Barron, L. Hecht, and G. Wilson. The lubricant of life: a proposal that solvent water promotes extremely fast conformational fluctuations in mobile heteropolypeptide structure. *Biochemistry*, 36(43):13143–13147, 1997.
- [74] V. Kurkal-Siebert, R. Agarwal, and J. C. Smith. Hydration-dependent dynamical transition in protein: protein interactions at approximately 240 K. *Phys. Rev. Lett.*, 100(13):138102, 2008.
- [75] V. P. Denisov and B. Halle. Protein hydration dynamics in aqueous solution. *Faraday Disc.*, 103:227–244, 1996.
- [76] R.G. Bryant. The dynamics of water-protein interactions. *Annu. Rev. Biophys. Biomol. Struct.*, 25:29–53, 1996.
- [77] E. Meyer. Internal water molecules and H-bonding in biological macromolecules - A review of structural features with functional implications. *Protein Science*, 1(12):1543–1562, 1992.
- [78] C. Malardier-Jugroot, M. E. Johnson, R. K. Murarkab, and T. Head-Gordon. Aqueous peptides as experimental models for hydration water dynamics near protein surfaces. *Phys. Chem. Chem. Phys.*, 10(32):4903–4908, 2008.
- [79] S. K. Pal, J. Peon, and Ahmed H. Zewail. Biological water at the protein surface: dynamical solvation probed directly with femtosecond resolution. *Proc. Nat. Acad. Sci. USA*, 99(4):1763–1768, 2002.
- [80] N. Nandi and B. Bagchi. Dielectric Relaxation of Biological Water. *J. Phys. Chem.*, 101(97):10954–10961, 1997.
- [81] N. Nandi, K. Bhattacharyya, and B. Bagchi. Dielectric relaxation and solvation dynamics of water in complex chemical and biological systems. *Chem Rev*, 100(6):2013–46, 2000.
- [82] I.D. Kuntz Jr. and W. Kauzmann. Hydration of proteins and polypeptides. *Advan. Protein Chem.*, 28:239 – 345, 1974.

- [83] Sudipta K. Sinha and Sanjoy Bandyopadhyay. Local heterogeneous dynamics of water around lysozyme: a computer simulation study. *Phys. Chem. Chem. Phys.*, 14(2):899, 2012.
- [84] L. Lupi, L. Comez, M. Paolantoni, D. Fioretto, and Branka M. Ladanyi. Dynamics of biological water: insights from molecular modeling of light scattering in aqueous trehalose solutions. *J. Phys. Chem. B*, 116(25):7499–7508, 2012.
- [85] W. Gu and B. P. Schoenborn. Molecular dynamics simulation of hydration in myoglobin. *Proteins*, 22(1):20–26, 1995.
- [86] V. A. Makarov, M. Feig, B. K. Andrews, and B. M. Pettitt. Diffusion of solvent around biomolecular solutes: a molecular dynamics simulation study. *Biophys. J.*, 75(1):150–158, 1998.
- [87] D. I. Svergun, S. Richard, M. H. Koch, Z. Sayers, S. Kuprin, and G. Zaccai. Protein hydration in solution: experimental observation by x-ray and neutron scattering. *Proc. Nat. Acad. Sci. USA*, 95(5):2267–2272, 1998.
- [88] M. Marchi, F. Sterpone, and M. Ceccarelli. Water rotational relaxation and diffusion in hydrated lysozyme. *J. Am. Chem. Soc.*, 124(23):6787–6791, 2002.
- [89] F. T. Burling, W. I. Weis, K. M. Flaherty, and A. T. Brünger. Direct observation of protein solvation and discrete disorder with experimental crystallographic phases. *Science*, 271(5245):72–77, 1996.
- [90] M. Gerstein and C. Chothia. Packing at the protein-water interface. *Proc. Nat. Acad. Sci. USA*, 93(19):10167–10172, 1996.
- [91] Anna R. Bizzarri and S. Cannistraro. Molecular Dynamics of Water at the Protein-Solvent Interface. *J. Phys. Chem. B*, 106(26):6617–6633, 2002.
- [92] F. Pizzitutti, M. Marchi, F. Sterpone, and Peter J. Rossky. How protein surfaces induce anomalous dynamics of hydration water. *J. Phys. Chem. B*, 111(26):7584–7590, 2007.
- [93] X. D. Cheng and B. P. Schoenborn. Neutron diffraction study of carbonmonoxymyoglobin. *J. Mol. Biol.*, 220(2):381–399, 1991.
- [94] M. Bonn, D. Paparo, Klaas-Jan Tielrooij, and H. Bakker. TeraHertz Dielectric Relaxation of Biological Water Confined in Model Membranes made of Lyotropic Phospholipids. *Molecular Crystals and Liquid Crystals*, 500(1):108–117, 2009.
- [95] U. Kaatzte. On the existence of bound water in biological systems as probed by dielectric spectroscopy. *Physics in medicine and biology*, 35(12):1663–1681, 1990.
- [96] G. Otting, E. Liepinsh, and K. Wüthrich. Protein hydration in aqueous solution. *Science*, 254(5034):974–980, 1991.
- [97] V. Helms and R.C. Wade. Thermodynamics of water mediating protein-ligand interactions in cytochrome p450cam: a molecular dynamics study. *Biophys. J.*, 69:810–824, 1995.

- [98] M. Paolantoni, L. Comez, M. E. Gallina, P. Sassi, F. Scarponi, D. Fioretto, and A. Morresi. Light scattering spectra of water in trehalose aqueous solutions: evidence for two different solvent relaxation processes. *J. Phys. Chem. B*, 113(22):7874–7878, 2009.
- [99] Y. Levy and José N. Onuchic. Water and proteins: a love-hate relationship. *Proc. Nat. Acad. Sci. USA*, 101(10):3325–3326, 2004.
- [100] H. S. Frank and M. W. Evans. Free Volume and Entropy in Condensed Systems III. Entropy in Binary Liquid Mixtures; Partial Molal Entropy in Dilute Solutions; Structure and Thermodynamics in Aqueous Electrolytes. *J. Chem. Phys.*, 13(11):507, 1945.
- [101] W. Kuazmann. Some factors in the interpretation of protein denaturation. *Advances in protein chemistry*, 14:1–63, 1959.
- [102] B. J. Alder and T. E. Wainwright. Phase Transition for a Hard Sphere System. *J. Chem. Phys.*, 27(5):1208–1209, 1957.
- [103] W. W. Wood and J. D. Jacobson. Preliminary results from a recalculation of the monte carlo equation of state of hard spheres. *The Journal of Chemical Physics*, 27(5):1207–1208, 1957.
- [104] B. R. J. A. McCammon, Gelin and M. Karplus. Dynamics of folded proteins. *Nature*, 267(5612):585–590, 1977.
- [105] L. Verlet. Computer "experiments" on classical fluids. i. thermodynamical properties of lennard-jones molecules. *Phys. Rev.*, 59(1):98–103, 1967.
- [106] R. D. Ruth. A canonical integration technique. *IEEE T. Nucl. Sci.*, 30(4):2669–2671, 1983.
- [107] C. W. Gear. *Numerical initial value problems in ordinary differential equations*. Prentice-Hall, Englewood Cliffs, NJ, 1966.
- [108] K. Vanommeslaeghe, E. Hatcher, C. Acharya, S. Kundu, S. Zhong, J. Shim, E. Darian, O. Guvench, P. Lopes, I. Vorobyov, and A. D. Mackerell. CHARMM general force field: A force field for drug-like molecules compatible with the CHARMM all-atom additive biological force fields. *J. Chem. Comp.*, 31(4):671–690, 2010.
- [109] D. Ferguson, T. E. Cheatham, G. Seibel, D. A. Pearlman, D. A. Case, P. Kollman, W. S. Ross, J. W. Caldwell, and S. DeBolt. AMBER, a package of computer programs for applying molecular mechanics, normal mode analysis, molecular dynamics and free energy calculations to simulate the structural and energetic properties of molecules. *Comput. Phys. Commun.*, 91(1-3):1–41, 1995.
- [110] C. Oostenbrink, A. Villa, A. E. Mark, and W. F. Van Gunsteren. A biomolecular force field based on the free enthalpy of hydration and solvation: The gromos force-field parameter sets 53a5 and 53a6. *J. Chem. Comp.*, 25(13):1656–1676, 2004.
- [111] W. L. Jorgensen and J. Tirado-Rives. The opls [optimized potentials for liquid simulations] potential functions for proteins, energy minimizations for crystals of cyclic peptides and crambin. *J. Am. Chem. Soc.*, 110(6):1657–1666, 1988.

- [112] J. W. Ponder and C. Wu. Current status of the amoeba polarizable force field. *J. Phys. Chem. B*, 114(8):2549–2564, 2010.
- [113] N. Gresh, G. A. Cisneros, T. A. Darden, and J-P Piquemal. Anisotropic, polarizable molecular mechanics studies of inter-, intra-molecular interactions, and ligand-macromolecule complexes. a bottom-up strategy. *J. Chem. Theory. Comput.*, 3(6):1960–1986, 2007.
- [114] A. C. T. van Duin, S. Dasgupta, F. Lorant, and W. A. Goddard III. Reaxff: a reactive force field for hydrocarbons. *J. Phys. Chem. A*, 105(41):9396–9409, 2001.
- [115] D. W. M. Hofmann, L. Kuleshova, and B. D’Aguanno. A new reactive potential for the molecular dynamics simulation of liquid water. *Chem. Phys. Lett.*, 448(1-3):138–143, 2007.
- [116] A. J. Stone. *The Theory of intermolecular forces*. Clarendon, Oxford, 1996.
- [117] C. Sagui and T. A. Darden. Molecular dynamics simulations of biomolecules: Long-range electrostatic effects. *Annu. Rev. Biophys. Biomol. Struct.*, 28:155, 1999.
- [118] A. J. Stone. Distributed multipole analysis, or how to describe a molecular charge distribution. *Chem. Phys. Lett.*, 83:233–239, 1981.
- [119] W. A. Sokalski and R. A. Poirier. Cumulative atomic multipole representation of the molecular charge distribution and its basis set dependence. *Chem. Phys. Lett.*, 98:86–92, 1983.
- [120] T. Bereau, C. Kramer, F. W. Monnard, E. S. Nogueira, T. R. Ward, and M. Meuwly. Scoring multipole electrostatics in condensed-phase atomistic simulations. *J. Phys. Chem. B*, 117(18):5460–5471, 2013.
- [121] C. Kramer, P. Gedeck, and M. Meuwly. Atomic multipoles: Electrostatic potential fit, local reference axis systems, and conformational dependence. *J. Chem. Comp.*, 33(20):1673–1688, 2012.
- [122] N. Plattner and M. Meuwly. The role of higher co-multipole moments in understanding the dynamics of photodissociated carbonmonoxide in myoglobin. *Biophys. J.*, 94:2505–2515, 2008.
- [123] N. Plattner and M. Meuwly. Atomistic simulations of co vibrations in ices relevant to astrochemistry. *ChemPhysChem*, 9:1271–1277, 2008.
- [124] K. Nienhaus, S. Lutz, M. Meuwly, and G. U. Nienhaus. Structural identification of spectroscopic substates in neuroglobin. *ChemPhysChem*, 11(1):119–129, 2010.
- [125] N. Plattner, T. Bandi, J. D. Doll, D. L. Freeman, and M. Meuwly. Md simulations using distributed multipole electrostatics: Structural and spectroscopic properties of co- and methane-containing clathrates. *Mol. Phys.*, 106:1675–1684, 2008.
- [126] P. K. Gupta and M. Meuwly. Dynamics and vibrational spectroscopy of water at hydroxylated silica surface. *Faraday Discuss.*, 167:329–346, 2013.
- [127] G.M. Torrie and J.P. Valleau. Nonphysical sampling distributions in Monte Carlo free-energy estimation: Umbrella sampling. *J. Comput. Phys.*, 23:187–199, 1977.

- [128] G.M. Torrie and J.P. Valleau. Monte carlo study of a phase separating liquid mixture by umbrella sampling. *J. Chem. Phys.*, 66:1402–1408, 1977.
- [129] J. G. Kirkwood. Statistical mechanics of fluid mixtures. *J. Chem. Phys.*, 3(5):300–313, 1935.
- [130] E. A. Carter, G. Ciccotti, J. T. Hynes, and R. Kapral. Constrained reaction coordinate dynamics for the simulation of rare events. *Chem. Phys. Lett.*, 156:472–477, 1989.
- [131] T. P. Straatsma and J. A. McCammon. Multiconfiguration thermodynamic integration. *J. Chem. Phys.*, 95:1175–1188, 1991.
- [132] M. Sprik and G. Ciccotti. Free energy from constrained molecular dynamics. *J. Chem. Phys.*, 109:7737–7744, 1998.
- [133] R. W. Zwanzig. High-temperature equation of state by a perturbation method in nonpolar gases. *J. Chem. Phys.*, 22:1420–1426, 1954.
- [134] C. B. Barnett and K. J. Naidoo. Free energies from adaptive reaction coordinate forces (fearcf): an application to ring puckering. *Mol. Phys.*, 107(8-12):1243–1250, 2009.
- [135] C. Jarzynski. Nonequilibrium equality for free energy differences. *Phys. Rev. Lett.*, 78(14):2690–2693, 1997.
- [136] A. Laio and M. Parrinello. Escaping free-energy minima. *Proc. Nat. Acad. Sci. USA*, 99(20):12562–12566, 2002.
- [137] I. R. McDonald and K. Singer. Machine calculation of thermodynamic properties of a simple fluid at supercritical temperatures. *J. Chem. Phys.*, 47:4766–4772, 1967.
- [138] I. R. McDonald and K. Singer. Examination of the adequacy of the 12–6 potential for liquid argon by means of monte carlo calculations. *J. Chem. Phys.*, 50:2308–2315, 1969.
- [139] I. R. McDonald and K. Singer. Calculation of the thermodynamic properties of liquid argon from lennard-jones parameters by a monte carlo method. *Discuss. Faraday Soc.*, 43:40–49, 1967.
- [140] J. A. McCammon. Free energy from simulations: Current opinion in structural biology. *Current Opinion in Structural Biology*, 1(2):196–200, 1991.
- [141] R. D. Ambashta and M. Sillanpaa. Water purification using magnetic assistance: A review. *Journal of Hazardous Materials*, 180(1):38–49, 2010.
- [142] Y. Du, L. E. Luna, W. S. Tan, M. F. Rubner, and R. E. Cohen. Hollow silica nanoparticles in uv - visible antireflection coatings for poly(methyl methacrylate) substrates. *ACS Nano*, 4(7):4308–4316, 2010.
- [143] D. Lee, R. E. Cohen, and M. F. Rubner. Antibacterial properties of ag nanoparticle loaded multilayers and formation of magnetically directed antibacterial microparticles. *Langmuir*, 21(21):9651–9659, 2010.
- [144] Y. Zhang, M. Aagesen, J. V. Holm, H. I. Jorgensen, J. Wu, and H. Liu. Self-catalyzed gaasp nanowires grown on silicon substrates by solid-source molecular beam epitaxy. *Nano Letters*, 13(8):3897–3902, 2013.

- [145] D. Liu, B. Herranz-Blanco, E. Makila, L. R. Arriaga, S. Mirza, D. A. Weitz, N. Sandler, J. Salonen, J. Hirvonen, , and H. A. Santos. Microfluidic templated mesoporous silicon–solid lipid microcomposites for sustained drug delivery. *Appl. Mater. Interfaces*, 5(22):12127–12134, 2013.
- [146] M. J. J. Hetem, J. D. De Haan, H. A. Claessens, L. J. Van de Ven, C. A. Cramers, and J. N. Kinkel. Influence of alkyl chain length on the stability of n-alkyl-modified reversed phases. 1. chromatographic and physical analysis. *Anal. Chem.*, 62(21):2288–2296, 1990.
- [147] M. J. J. Hetem, J. W. De Haan, H. A. Claessens, L. J. M. Van de Ven, C. A. Cramers, P. W. J. G. Wijnen, and J. N. Kinkel. Influence of alkyl chain length on the stability of n-alkyl-modified reversed phases. 2. model dissolution study. *Anal. Chem.*, 62(21):2296–2300, 1990.
- [148] Kenny B. L. Atomistic modeling of enantioselection in chromatography. *J. Chromatogr. A*, 906(1-2):417–442, 2001.
- [149] W. Hertl and M. L. Hair. Adsorption of water on silica. *Nature*, 223:1150–1151, 1969.
- [150] R. Albert, C. Dominique, S. Mariona, J. Jean-François, and U Piero. Silica surface features and their role in the adsorption of biomolecules: Computational modeling and experiments. *Chemical Reviews*, 113(6):4216–4313, 2013.
- [151] J. Morag, M. Dishon, and U. Sivan. The governing role of surface hydration in ion specific adsorption to silica: An afm-based account of the hofmeister universality and its reversal. *Langmuir*, 29(21):6317–6322, 2013.
- [152] C. Tanford. The hydrophobic effect and the organization of living matter. *Science*, 200(4345):1012–1018, 1978.
- [153] F. Fornasiero, H. G. Park, J. K. Holt, M. Stadermann, C. P. Grigoropoulos, A. Noy, and O. Bakajin. Ion exclusion by sub-2-nm carbon nanotube pores. *Proc. Nat. Acad. Sci. USA*, 105(45):17250–17255, 2008.
- [154] Y. Jiang, A. Lee, Jiayun Chen, Martine Cadene, Brian T. Chait, and R. MacKinnon. Crystal structure and mechanism of a calcium-gated potassium channel. *Nature*, 417(6888):515–522, 2002.
- [155] Jongjoo Kim, Wenyun Lu, Weihong Qiu, Lijuan Wang, Martin Caffrey, and Dongping Zhong. Ultrafast hydration dynamics in the lipidic cubic phase: Discrete water structures in nanochannels. *J. Phys. Chem. B*, 110(43):21994–22000, 2006.
- [156] A. Pizzi and G. De Sousa. On the resolution of dihydroxydiphenylmethanes on achiral crystalline cellulose ii. correlation of experimental and calculated results. *Chemical Physics*, 164(2):203 – 216, 1992.
- [157] V. Noinville, C. Vidal-Madjar, and B. Sebille. Modeling of protein adsorption on polymer surfaces. computation of adsorption potential. *J. Phys. Chem.*, 99(5):1516–1522, 1995.
- [158] J. L. Rafferty, J. Ilja Siepmann, and M. R. Schure. Influence of bonded-phase coverage in reversed-phase liquid chromatography via molecular simulation II. Effects on solute retention. *J. Chromatogr. A*, 1204(1):20–27, 2008.

- [159] J. L. Rafferty, L. Zhang, J. I. Siepmann, and M. R. Schure. Retention mechanism in reversed-phase liquid chromatography: a molecular perspective. *Anal. Chem.*, 79(17):6551–6558, 2007.
- [160] L. Zhanga, Li Suna, J. Ilja Siepmann, and Mark R. Schure. Molecular simulation study of the bonded-phase structure in reversed-phase liquid chromatography with neat aqueous solvent. *J. Chromatogr. A*, 1079(1-2):127–135, 2005.
- [161] Rebecca K. Lindsey, Jake L. Rafferty, Becky L. Eggimann, J. Ilja Siepmann, and Mark R. Schure. Molecular simulation studies of reversed-phase liquid chromatography. *J. Chromatogr. A*, 1287:60–82, 2013.
- [162] A. Fouqueau, M. Meuwly, and R. J. Bemish. Adsorption of acridine orange at a C8,18/water/acetonitrile interface. *J. Phys. Chem. B*, 111(34):10208–10216, 2007.
- [163] Raymond D. Mountain. Molecular Dynamics Study of Water-Acetonitrile Mixtures. *J. Phys. Chem. A*, 103(50):10744–10748, 1999.
- [164] S. J. Klatt and T. L. Beck. Microscopic Simulation of Solute Transfer in Reversed Phase Liquid Chromatography. *J. Phys. Chem.*, 100(14):5931–5934, 1996.
- [165] G. Eaton, A. S. Pena-Nunez, and M. C. R. Symons. Solvation of cyanoalkanes [CH<sub>3</sub>CN and (CH<sub>3</sub>)<sub>3</sub>CCN]. An infrared and nuclear magnetic resonance study. *J. Chem. Soc. Faraday Trans.*, 84(6):2181–2193, 1988.
- [166] D. S. Venables and C. A. Schmuttenmaer. Far-infrared spectra and associated dynamics in acetonitrile-water mixtures measured with femtosecond THz pulse spectroscopy. *J. Chem. Phys.*, 108(12):4935–4944, 1998.
- [167] D. S. Venables and C. A. Schmuttenmaer. Spectroscopy and dynamics of mixtures of water with acetone, acetonitrile, and methanol. *Journal of Chemical Physics*, 113(24):11222–11236, 2000.
- [168] E. D. Dawson and S. L. Wallen. Probing transport and microheterogeneous solvent structure in acetonitrile-water mixtures and reversed-phase chromatographic media by NMR quadrupole relaxation. *J. Am. Chem. Soc.*, 124(47):14210–14220, 2002.
- [169] K. N. Woods and H. Wiedemann. The influence of chain dynamics on the far-infrared spectrum of liquid methanol-water mixtures. *J. Chem. Phys.*, 123(13):134507, 2005.
- [170] I. L. Shulgin and E. Ruckenstein. Excess around a central molecule with application to binary mixtures. *Phys. Chem. Chem. Phys.*, 10(8):1097–1105, 2008.
- [171] Imre Bakó, Tünde Megyes, Szabolcs Bálint, Tamás Grósz, and Viorel Chihaiia. Water-methanol mixtures: topology of hydrogen bonded network. *Phys. Chem. Chem. Phys.*, 10(32):5004–5011, 2008.
- [172] Jeffrey R. R. and L. E. Hall. The Solvation of Acetonitrile. *J. Am. Chem. Soc.*, 121(15):3730–3744, 1999.
- [173] F. Gritti and G. Guiochon. A chromatographic estimate of the degree of surface heterogeneity of RPLC packing materials. III. Endcapped amido-embedded reversed phase. *J. Chromatogr. A*, 1103(1):69–82, 2006.

- [174] Jake L. Rafferty, J. Ilja Siepmann, and Mark R. Schure. Mobile phase effects in reversed-phase liquid chromatography: a comparison of acetonitrile/water and methanol/water solvents as studied by molecular simulation. *J. Chromatogr. A*, 1218(16):2203–2213, 2011.
- [175] W. L. Jorgensen, J. Chandrasekhar, Jeffrey D. Madura, Roger W. Impey, and M. L. Klein. Comparison of simple potential functions for simulating liquid water. *J. Chem. Phys.*, 79(2), 1983.
- [176] Jean-Paul Ryckaert, G. Ciccotti, and H. J.C Berendsen. Numerical integration of the cartesian equations of motion of a system with constraints: molecular dynamics of n-alkanes. *Journal of Computational Physics*, 23(3):327–341, 1977.
- [177] M. L. P. Price, D. Ostrovsky, and W. L. Jorgensen. Gas-phase and liquid-state properties of esters, nitriles, and nitro compounds with the OPLS-AA force field. *J. Chem. Comp.*, 22(13):1340–1352, 2001.
- [178] B. R. Brooks and R. E. Bruccoleri. CHARMM: A program for macromolecular energy, minimization, and dynamics calculations. *J. Chem. Comp.*, 4(2):187–217, 1983.
- [179] R. P. W. Scott. The silica-gel surface and its interactions with solvent and solute in liquid chromatography. *Faraday Symp. Chem. Soc.*, 15:49–68, 1980.
- [180] S. Dixit, J. Crain, W. C. K. Poon, J. L. Finney, and A. K. Soper. Molecular segregation observed in a concentrated alcohol-water solution. *Nature*, 416(6883):829–832, 2002.
- [181] L. Dougan, R. Hargreaves, S. P. Bates, J. L. Finney, V. Réat, A. K. Soper, and J. Crain. Segregation in aqueous methanol enhanced by cooling and compression. *J. Chem. Phys.*, 122(17):174514, 2005.
- [182] Shin G. Chou, Alan K. Soper, Sheila Khodadadi, Joseph E. Curtis, Susan Krueger, Marcus T. Cicerone, Andrew N. Fitch, and Evgenyi Y. Shalaev. Pronounced microheterogeneity in a sorbitol-water mixture observed through variable temperature neutron scattering. *J. Phys. Chem. B*, 116(15):4439–47, 2012.
- [183] S. Alexander. Adsorption of chain molecules with a polar head a scaling description. *J. Phys.*, 38:983, 1977.
- [184] P. G. de Gennes. Polymers at an interface; a simplified view. *Adv. Colloid Interface Sci.*, 27:189, 1987.
- [185] M. G. Martin and J. I. Siepmann. Simulating retention in gas-liquid chromatography. *J. Phys. Chem. B*, 103(55):11191–11195, 1999.
- [186] C. D. Wick, J. I. Siepmann, and M. R. Schure. Simulation studies of retention in isotropic or oriented liquid n-octadecane. *J. Phys. Chem. B*, 105(44):10961–10966, 2001.
- [187] C. D. Wick, J. I. Siepmann, and M. R. Schure. Influence of analyte overloading on retention in gas-liquid chromatography: a molecular simulation view. *Anal. Chem.*, 74(1):37–44, 2002.
- [188] C. D. Wick, J. I. Siepmann, and M. R. Schure. Molecular simulation of concurrent gas-liquid interfacial adsorption and partitioning in gas-liquid chromatography. *Anal. Chem.*, 74(14):3518–3524, 2002.



- [189] W. L. Jorgensen, J. Chandrasekhar, J. D. Madura, R. W. Impey, and M. Klein. Comparison of simple potential functions for simulating liquid water. *J. Chem. Comp.*, 79(2), 1983.
- [190] N. Kumagai, K. Kawamura, and T Yokokawa. . *Mol. Simul.*, 12():177–186, 1994.
- [191] M. W. Lee and M. Meuwly. . *J. Phys. Chem. A*, 115():5053–5061, 2011.
- [192] Song Hi Lee and Peter J. Rossky. A comparison of the structure and dynamics of liquid water at hydrophobic and hydrophilic surfaces—a molecular dynamics simulation study. *The Journal of Chemical Physics*, 100(4):3334–3345, 1994.
- [193] Anatoli A. Milischuk and Branka M. Ladanyi. Structure and dynamics of water confined in silica nanopores. *The Journal of Chemical Physics*, 135(17):174709–11, 2011.
- [194] M. W. Lee and M. Meuwly. Molecular Dynamics Simulation of Nitric Oxide in Myoglobin . *J. Phys. Chem. B*, 116():4154–4162, 2012.
- [195] J. Yang and E. G. Wang. Water adsorption on hydroxylated alpha-quartz(0001) surface: From monomer to flat bilayer. *Phys. Rev. B*, 73:35406, 2006.
- [196] P. A. Bonnaud, B. Coasne, and R. J-M. Pellenq. Molecular simulation of water confined in silica nanoporous silica. *J. Phys. Condens. Matter*, 22:284110, 2010.
- [197] D. Argyris, D. R. Cole, and A. Striolo. Dynamics of interfacial water at the silica surface. *J. Phys. Chem. C*, 113:19591–19600, 2009.
- [198] J. Ha, T. Hyun Yoon, Y. Wang, C. B. Musgrave, and J. G. E. Brown. Adsorption of organic matter at mineral/water interfaces: 7. atr-ftir and quantum chemical study of lactate interactions with hematite nanoparticles. *Langmuir*, 24:6683, 2008.
- [199] R. Notman and T. R. Walsh. Molecular dynamics studies of the interactions of water and amino acid analogues with quartz surfaces. *Langmuir*, 25:1638, 2009.
- [200] A. A. Skelton, D. J. Wesolowski, and P. T. Cummings. Investigating the quartz/water interface using classical and ab initio molecular dynamics. *Langmuir*, 27:8700, 2011.
- [201] Osbert Z. Tan, K. H. Tsai, Michael C. H. Wu, and Jer-Lai Kuo. Structural and Dynamic Properties of Water on the GaN Polar Surface. *J. Phys. Chem. C*, 115(45):22444–22450, 2011.
- [202] A. A. Skelton, P. Fenter, J. D. Kubicki, D. J. Wesolowski, and P. T. Cummings. Simulations of the quartz(1011)/water interface: A comparison of classical force fields, ab initio molecular dynamics, and x-ray reflectivity experiments. *J. Phys. Chem. C*, 115(5):2076–2088, 2011.
- [203] W. S. Price, H. Ide, and Y. Arata. Self-diffusion of supercooled water to 238 k using pgse nmr diffusion measurements. *J. Phys. Chem. A*, 103:448, 1999.
- [204] D. Argyris, Tuan Ho, David R. Cole, and A. Striolo. Molecular Dynamics Studies of Interfacial Water at the Alumina Surface. *J. Phys. Chem. C*, 115(5):2038–2046, 2011.
- [205] M. R. Warne, N. L. Allan, and T. Cosgrove. Computer simulation of water molecules at kaolinite and silica surfaces. *Physical Chemistry Chemical Physics*, 2(16):3663–3668, 2000.

- [206] P. A. Pieniazek, Yu-Shan Lin, J. Chowdhary, B. M. Ladanyi, and J. L. Skinner. Vibrational Spectroscopy and Dynamics of Water Confined inside Reverse Micelles. *J. Phys. Chem. B*, 113(45):15017–15028, 2009.
- [207] J. Chowdhary and B. M. Ladanyi. Hydrogen bond dynamics at the water/hydrocarbon interface. *J. Phys. Chem. B*, 113:4045–4053, 2009.
- [208] C. Chapados and J. J. Max. Isotope effects in liquid water by infrared spectroscopy. iii. h<sub>2</sub>o and d<sub>2</sub>o spectra from 6000 to 0 cm<sup>-1</sup>. *J. Chem. Phys.*, 131:184505–184519, 2009.
- [209] W. E. Royer, W. A. Hendrickson, and E. Chiancone. Structural transitions upon ligand binding in a cooperative dimeric hemoglobin. *Science*, 249(4968):518–521, 1990.
- [210] A. Mozzarelli, S. Bettati, C. Rivetti, G. L. Rossi, G. Colotti, and E. Chiancone. Cooperative oxygen binding to scapharca inaequalvis hemoglobin in the crystal. *J. Biol. Chem.*, 271(7):3627–3632, 1996.
- [211] J. Monod, J. Wyman, and J. P. Changeux. On the nature of allosteric transitions: A plausible model. *J. Mol. Biol.*, 12:88–118, 1965.
- [212] J. E. Fuchs, S. von Grafenstein, R. G. Huber, H. G. Wallnoefer, and K. R. Liedl. Specificity of a protein–protein interface: Local dynamics direct substrate recognition of effector caspases. *Proteins: Structure, Function, and Bioinformatics*, 82(4):546–555, 2014.
- [213] D. A. Liberles, S. A. Teichmann, I. Bahar, U. Bastolla, J. Bloom, E. Bornberg-Bauer, L. J. Colwell, A. P. Jason de Koning, N. V. Dokholyan, J. Echave, A. Elofsson, D. L. Gerloff, R. A. Goldstein, J. A. Grahnen, M. T. Holder, C. Lakner, N. Lartillot, Simon C. Lovell, G. Naylor, T. Perica, D. D. Pollock, T. Pupko, L. Regan, A. Roger, N. Rubinstein, E. Shakhnovich, K. Sjölander, S. Sunyaev, A. I. Teufel, J. L. Thorne, J. W. Thornton, D. M. Weinreich, and S. Whelan. The interface of protein structure, protein biophysics, and molecular evolution. *Protein Sci.*, 21(6):769–785, 2012.
- [214] D. Long, Y. Mu, and D. Yang. Molecular dynamics simulation of ligand dissociation from liver fatty acid binding protein. *PLoS ONE*, 4(6):e6081, 2009.
- [215] A. Bhingé, P. Chakrabarti, K. Uthannumallian, K. Bajaj, K. Chakraborty, and R. Varadarajan. Accurate detection of protein:ligand binding sites using molecular dynamics simulations. *Structure*, 12(11):1989 – 1999, 2004.
- [216] J. E. Knapp, R. Pahl, J. Cohen, J. C. Nichols, K. Schulten, Q. H. Gibson, V. Srajer, and W. E. Royer. Ligand migration and cavities within Scapharca Dimeric HbI: studies by time-resolved crystallography, Xe binding, and computational analysis. *Structure London England 1993*, 17(11):1494–1504, 2009.
- [217] E. Chiancone, R. Elber, W. E. Royer Jr, R. Regan, and Q. H. Gibson. Ligand binding and conformation change in the dimeric hemoglobin of the clam scapharca inaequalvis. *J. Biol. Chem.*, 268(8):5711–5718, 1993.
- [218] K. Nienhaus, J. E. Knapp, P. Palladino, Jr. Royer, W. E., and G. U. Nienhaus. Ligand migration and binding in the dimeric hemoglobin of Scapharca inaequalvis. *Biochemistry*, 46(49):14018–14031, 2007.

- [219] E. Antonini, F. Ascoli, M. Brunori, E. Chiancone, D. Verzili, R. J. Morris, and Q. H. Gibson. Kinetics of ligand binding and quaternary conformational change in the homodimeric hemoglobin from *Scapharca inaequalvis*. *The Journal of Biological Chemistry*, 259(11):6730–6738, 1984.
- [220] A. Szabo. Kinetics of hemoglobin and transition state theory. *Proc. Nat. Acad. Sci. USA*, 75(5):2108–2111, 1978.
- [221] J. S. Philo, U. Dreyer, and J. W. Lary. Quaternary structure dynamics and carbon monoxide binding kinetics of hemoglobin valency hybrids. *Biophys. J.*, 70(4):1949–1965, 1996.
- [222] J. Choi, S. Muniyappan, J. T. Wallis, W. E. Royer, and H. Ihee. Protein conformational dynamics of homodimeric hemoglobin revealed by combined time-resolved spectroscopic probes. *ChemPhysChem*, 11(1):109–114, 2010.
- [223] I. Hyotcherl, S. Muniyappan, Y. Kim, J. G. Kim, and S. Nozawa. Direct observation of the cooperative Protein Structural dynamics of Homodimeric Hemoglobin from 100 ps to 10 ms with Pump-Probe X ray Solution scattering. *J. Am. Chem. Soc.*, 134:7001–7008, 2012.
- [224] V. Šrajer, Z. Ren, T. Y. Teng, M. Schmidt, T. Ursby, D. Bourgeois, C. Pradervand, W. Schildkamp, M. Wulff, and K. Moffat. Protein conformational relaxation and ligand migration in Myoglobin: A nanosecond to millisecond molecular movie from time-resolved Laue X-ray diffraction. *Biochemistry*, 40:13802–13815, 2001.
- [225] H. S. Cho, N. Dashdorj, F. Schotte, T. Graber, R. Henning, and P. Anfinrud. Protein structural dynamics in solution unveiled via 100-ps time-resolved x-ray scattering. *Proc. Nat. Acad. Sci. USA*, 107(16):7281–7286, 2010.
- [226] B. R. Gelin and M. Karplus. Mechanism of tertiary structural change in hemoglobin. *Proc. Nat. Acad. Sci. USA*, 74(3):801–805, 1977.
- [227] S. Song, L. Rothberg, D. L. Rousseau, A. Boffi, and E. Chiancone. Metastable CO binding sites in the photoproduct of a novel cooperative dimeric hemoglobin. *Biophys. J.*, 65(5):1959–1962, 1993.
- [228] E. Chiancone and A. Boffi. Structural and thermodynamic aspects of cooperativity in the homodimeric hemoglobin from *Scapharca inaequalvis*. *Biochemistry*, 86(2-3):173–178, 2000.
- [229] W. A. Eaton, E. R. Henry, J. Hofrichter, and A. Mozzarelli. Is cooperative oxygen binding by hemoglobin really understood? *Nature structural biology*, 6(4):351–358, 1999.
- [230] Y. Zhou, H. Zhou, and M. Karplus. Cooperativity in *Scapharca* dimeric hemoglobin: simulation of binding intermediates and elucidation of the role of interfacial water. *Journal of molecular biology*, 326(2):593–606, 2003.
- [231] M. F. Colombo, D. C. Rau, and V. A. Parsegian. Protein solvation in allosteric regulation: a water effect on hemoglobin. *Science*, 256(5057):655–659, 1992.
- [232] R. Gnanasekaran, Y. Xu, and D. M. Leitner. Dynamics of water clusters confined in proteins: a molecular dynamics simulation study of interfacial waters in a dimeric hemoglobin. *J. Phys. Chem. B*, 114(50):16989–16996, 2010.

- [233] M. Karplus and D. L. Weaver. Protein-folding dynamics. *Nature*, 260(5550):404–406, 1976.
- [234] M. Karplus and D. L. Weaver. Protein folding dynamics: the diffusion-collision model and experimental data. *Protein science*, 3(4):650–668, 1994.
- [235] C. M. Dobson and M. Karplus. The fundamentals of protein folding: bringing together theory and experiment. *Current opinion in structural biology*, 9(1):92–101, 1999.
- [236] D. E. Shaw, P. Maragakis, K. Lindorff-Larsen, S. Piana, Ron O Dror, M. P. Eastwood, J. A. Bank, J. M. Jumper, J. K. Salmon, Y. Shan, and W. Wriggers. Atomic-level characterization of the structural dynamics of proteins. *Science*, 330(6002):341–346, 2010.
- [237] J. E. Knapp, R. Pahl, V. Šrajcar, and W. E. Royer. Allosteric action in real time: Time-resolved crystallographic studies of a cooperative dimeric hemoglobin. *Proc. Nat. Acad. Sci. USA*, 103(20):7649–7654, 2006.
- [238] B. R. Brooks, C. L. Brooks, A. D. Mackerell, L. Nilsson, R. J. Petrella, B. Roux, Y. Won, G. Archontis, C. Bartels, S. Boresch, A. Caffisch, L. Caves, Q. Cui, A. R. Dinner, M. Feig, S. Fischer, J. Gao, M. Hodoscek, W. Im, K. Kuczera, T. Lazaridis, J. Ma, V. Ovchinnikov, E. Paci, R. W. Pastor, C. B. Post, J. Z. Pu, M. Schaefer, B. Tidor, R. M. Venable, H. L. Woodcock, X. Wu, W. Yang, D. M. York, and M. Karplus. CHARMM: the biomolecular simulation program. *J. Chem. Comp.*, 30(10):1545–1614, 2009.
- [239] J. C. Phillips, R. Braun, W. Wang, J. Gumbart, E. Tajkhorshid, E. Villa, C. Chipot, R. D. Skeel, L. Kale, and K. Schulten. Scalable molecular dynamics with NAMD. *J. Chem. Comp.*, 26(16):1781–802, 2005.
- [240] J. P. Ryckaert, G. Ciccotti, and H. J. Berendsen. Numerical integration of the cartesian equations of motion of a system with constraints: molecular dynamics of n-alkanes. *J. Comput. Phys.*, 23:327–341, 1977.
- [241] G. M. Torrie and J. P. Valleau. Nonphysical sampling distributions in Monte Carlo free-energy estimation: Umbrella sampling. *Journal of Computational Physics*, 23(2):187–199, 1977.
- [242] S. Kumar, J. M. Rosenberg, D. Bouzida, R. H. Swendsen, and P. A. Kollman. THE weighted histogram analysis method for free-energy calculations on biomolecules. I. The method. *J. Chem. Comp.*, 13(8):1011–1021, 1992.
- [243] M. Souaille and B. Roux. Extension to the weighted histogram analysis method: combining umbrella sampling with free energy calculations, 2001.
- [244] M. Brunori and Q. H. Gibson. Cavities and packing defects in the structural dynamics of myoglobin. *EMBO Reports*, 2(8):674–679, 2001.
- [245] J. Cohen and K. Schulten. O<sub>2</sub> migration pathways are not conserved across proteins of a similar fold. *Biophys. J.*, 93(10):3591–3600, 2007.
- [246] E. Chiancone, D. Verzili, A. Boffi, W. E. Royer, and W. A. Hendrickson. A cooperative hemoglobin with directly communicating hemes. The Scapharca inaequalvis homodimer. *Biophysical Chemistry*, 37(1-3):287–292, 1990.

- [247] E. D. Streaker and D. Beckett. Ligand-linked structural changes in the escherichia coli biotin repressor: the significance of surface loops for binding and allostery. *J. Mol. Biol.*, 292(3):619–632, 1999.
- [248] J. I. Yeh, H. P. Biemann, J. Pandit, D. E. Koshland, and S. H. Kim. The three-dimensional structure of the ligand-binding domain of a wild-type bacterial chemotaxis receptor. structural comparison to the cross-linked mutant forms and conformational changes upon ligand binding. *J. Biol. Chem.*, 268(13):9787–9792, 1993.
- [249] J. I. Yeh, H. P. Biemann, J. Pandit, D. E. Koshland, and S. H. Kim. The relation between carbon monoxide binding and the conformational change of hemoglobin. *Biophys. J.*, 24(1):21–33, 1978.
- [250] H. Tsuruta, P. Vachette, and E. R. Kantrowitz. Direct observation of an altered quaternary-structure transition in a mutant aspartate transcarbamoylase. *Proteins: Structure, Function and Genetics*, 31(4):383–390, 1998.
- [251] T-C Tang, Yi Hu, P. Kienlen-Campard, L. E. Haylani, M. Decock, and S. O. Smith. Conformational changes induced by the a21g flemish mutation in the amyloid precursor protein lead to increased a  $\beta$  production. *Structure*, 22(3):387–396, 2014.
- [252] H. Unal, R. Jagannathan, A. Bhatnagar, K. Tirupula, R. Desnoyer, and S. S. Karnik. Long range effect of mutations on specific conformational changes in the extracellular loop 2 of angiotensin ii type 1 receptor. *J. Biol. Chem.*, 288(1):540–551, 2013.
- [253] G. K. Ackers and H. R. Halvorson. The linkage between oxygenation and subunit dissociation in human hemoglobin. *Proc. Nat. Acad. Sci. USA*, 71:4312–4316, 1974.
- [254] G. K. Ackers and S. H. C. Ip. Thermodynamic studies on subunit assembly in human hemoglobin: temperature dependence of the dimer-tetramer association constants for oxygenated and unliganded hemoglobins. *J. Biol. Chem.*, 252:82–87, 1977.
- [255] F. C. Mills, G. K. Ackers, H. T. Gaud, and S. J. Gill. Thermodynamic studies on ligand binding and subunit association of human hemoglobins. enthalpies of binding o<sub>2</sub> and co to subunit chains of hemoglobin a. *J. Biol. Chem.*, 254(8):2875–2880, 1979.
- [256] F. C. Mills and G. K. Ackers. Thermodynamic studies on the oxygenation and subunit association of human hemoglobin. temperature dependence of the linkage between dimer-tetramer association and oxygenation state. *J. Biol. Chem.*, 254(8):2881–2887, 1979.
- [257] Robert D. Gray. The kinetics of the alkaline bohr effect of human hemoglobin. *J. Biol. Chem.*, 245(12):2914–2921, 1970.
- [258] P. Guesnon, C. Poyart, E. Bursaux, and B. Bohn. The binding of lactate and chloride ions to human adult hemoglobin. *Respir Physiol.*, 38(2):115–129, 1979.
- [259] G. G. van Beek, E. R. Zuiderweg, and S. H. de Bruin. The binding of chloride ions to ligated and unligated human hemoglobin and its influence on the bohr effect. *Eur. J. Biochem.*, 99(2):379–383, 1979.
- [260] G. K. Ackers. Energetics of subunit assembly and ligand binding in human hemoglobin. *Biophys. J.*, 32(1):331–346, 1980.

- [261] J. S. Hub, M. B. Kubitzki, and Bert. L. De Groot. Spontaneous Quaternary and Tertiary T-R Transitions of Human Hemoglobin in Molecular Dynamics Simulation. *PLoS Computational Biology*, 6(5):11, 2010.
- [262] O. K. Yusuff, J. O. Babalola, G. Bussi, and S. Raugei. Role of the subunit interactions in the conformational transitions in adult human hemoglobin: An explicit solvent molecular dynamics study. *J. Phys. Chem. B*, 116(36):11004–11009, 2012.
- [263] L. Mouawada and D. Perahia. Motions in hemoglobin studied by normal mode analysis and energy minimization: Evidence for the existence of tertiary t-like, quaternary r-like intermediate structures. *J. Mol. Biol.*, 258(2):393–410, 1996.
- [264] N. Shibayama S-Yong Park, T. Yokoyama, Y. Shiro, and J. R. H. Tame. 1.25 Å resolution crystal structures of human haemoglobin in the oxy, deoxy and carbonmonoxy forms. *J. Mol. Biol.*, 360(3):690–701, 2006.
- [265] G. Vriend. What if: A molecular modeling and drug design program. *J. Mol. Graph.*, 8(1):52–56, 1990.
- [266] T. Darden, D. York, and L. Pedersen. Particle mesh ewald: An  $N \cdot \log(N)$  method for ewald sums in large systems. *J. Chem. Phys.*, 98(12):10089–10092, 1993.
- [267] R. Benesch, R. E. Benesch, and Y. Enoki. The interaction of hemoglobin and its subunits with 2,3-diphosphoglycerate. *Proc. Nat. Acad. Sci. USA*, 61(3):1102–1106, 1968.
- [268] E. R. Henry W. A. Eaton and J. Hofrichter. Application of linear free energy relations to protein conformational changes: the quaternary structural change of hemoglobin. *Proc. Nat. Acad. Sci. USA*, 88(10):4472–4475, 1991.



# Prashant Kumar Gupta

## Curriculum Vitae

### Personal Information

Address Hegenheimerstrasse 173, 4056, Basel, Switzerland  
Nationality Indian

### Education

- Feb,2010- June, 2014 **Ph.D. in Chemistry**, *Univeristy of Basel*, Basel, Switzerland.  
*Advisor: Prof. Markus Meuwly*
- 2006-08 **Master of Science**, *C.S.J.M. University*, Kanpur, (U.P), India.  
*Specialization in Physical Chemistry*
- 2002-05 **Bachelor of Science**, *Univeristy of Allahabad*, Allahabad, (U.P), India.

### Ph.D. Thesis

Title Computational exploration of water structure and dynamics at heterogeneous interface  
Supervisor Prof. Markus Meuwly  
Description This thesis deals with the perturbation in the static, dynamical and spectroscopic properties of water in the presence of interface and how interfacial water dynamics is coupled with motion of protein residues responsible for cooperative behavior.

### Awards and honor

#### National

1. Qualified the *Council for scientific and industrial research (CSIR)* exam in Chemical sciences, 2008
2. Qualified the *General aptitude test for engineers, (GATE)* in Chemical sciences, 2008

### Scientific publications

#### Published work

1. Dynamics of water/methanol mixtures at functionalized chromatographic interfaces. **Gupta, P. K. and Meuwly, M.**, J. Phys. Chem. B, 2012;116 (35)

Klingelbergstrasse 80, 4056 – Basel, Switzerland

☎ (+41) 763228251 • 📞 (+41) 612673815 • ✉ prashant.gupta@unibas.ch

1/3

2. Dynamics and vibrational spectroscopy of water at hydroxylated silica interfaces. **Gupta, P. K. and Meuwly, M.** (Faraday Discussion 167, 2013; 329-346)

[Manuscript under preparation](#)

3. Mechanism of cooperativity in scapharca dimer hemoglobin. Gupta, P. K. and Meuwly, M.
4. Understanding the structural transition in Human hemoglobin. Gupta, P. K. , Meuwly, M. and Karplus, M.
5. Thermodynamics of intercalation process of pharmacophore at chromatographic interfaces. Gupta, P. K. and Meuwly, M.
6. Water dynamics through C<sub>18</sub> grafted silica nano-pore. Gupta, P. K. and Meuwly, M.

---

## Poster presentations

1. Dynamics and vibrational spectroscopy of water at hydroxylated silica surface. P. K. Gupta, Faraday discussion 167, Bristol, U.K., 2013
2. Dynamics of water at hydroxylated silica surface. P. K. Gupta, Swiss chemical society meeting, 2013, EPFL Laussane, Switzerland
3. Effect of multipoles on the vibrational spectroscopy of water at hydroxylated silica surface. P. K. Gupta, Swiss association of computational chemist, 2013, University of Bern, Switzerland
4. Understanding the cooperative nature in Scapharca dimeric hemoglobin. P. K. Gupta, Theoretical chemistry symposium, 2012, IIT Guwahati, India
5. Cooperativity in Scapharca dimeric hemoglobin. P. K. Gupta, Functional dynamics of Biomolecules, 2012, Lugano, Switzerland
6. Dynamics of water/methanol mixture in heterogeneous environment. P. K. Gupta, Swiss chemical society meeting, 2012, ETH Zurich, Switzerland
7. Role of water in heterogeneous chromatographic interfaces. P. K. Gupta, 25th Molecular modeling workshop, 2011, Erlangen, Germany
8. Understanding the dynamics of water at heterogeneous silica interface, P. K. Gupta, Swiss chemical society meeting, 2011, EPFL Laussane, Switzerland

---

## Teaching experience

[Graduate teaching assistant, Department of Physical chemistry, University of Basel](#)

1. Statistical Mechanics : Spring-2013
2. Computational Chemistry Practical : Fall-2011, Fall-2012
3. Physical Chemistry Practical : Fall-2013
4. Graded assignments, conducted laboratory sessions, lectures, tutorials and help-sessions.

---

## Technical Skills

Programming Skills

platforms MacOS, Unix/Linux, Windows

*Klingelbergstrasse 80, 4056 – Basel, Switzerland*

☎ (+41) 763228251 • 📠 (+41) 612673815 • ✉ [prashant.gupta@unibas.ch](mailto:prashant.gupta@unibas.ch)

2/3



Tools Xmgrace, Gnuplot, Mathematica (intermediate)

---

## Workshop

- 1 Workshop on Computational biophysics, 2011, Bremen, Germany

---

## Interests

- Badminton
- Cooking
- Visiting new places
- Photography
- Watching movies
- Reading novels

---

## References

**Prof. Markus Meuwly**  
Department of Physical Chemistry  
University of Basel, 4056  
Klingelbergstrasse 80, Switzerland  
✉ [m.meuwly@unibas.ch](mailto:m.meuwly@unibas.ch)  
☎ +41 - 612673821

**Prof. Stefan Willitsch**  
Department of Physical Chemistry  
University of Basel, 4056  
Klingelbergstrasse 80, Switzerland  
✉ [stefan.willitsch@unibas.ch](mailto:stefan.willitsch@unibas.ch)  
☎ +41 - 612673830

**Prof. Gerhard Hummer, Director**  
Department of Theoretical Biophysics  
Max Planck Institute of Biophysics  
Max-von-Laue-Strasse 3  
D-60438 Frankfurt am Main  
✉ [gerhard.hummer@biophys.mpg.de](mailto:gerhard.hummer@biophys.mpg.de)  
☎ +49 - 69 63032500